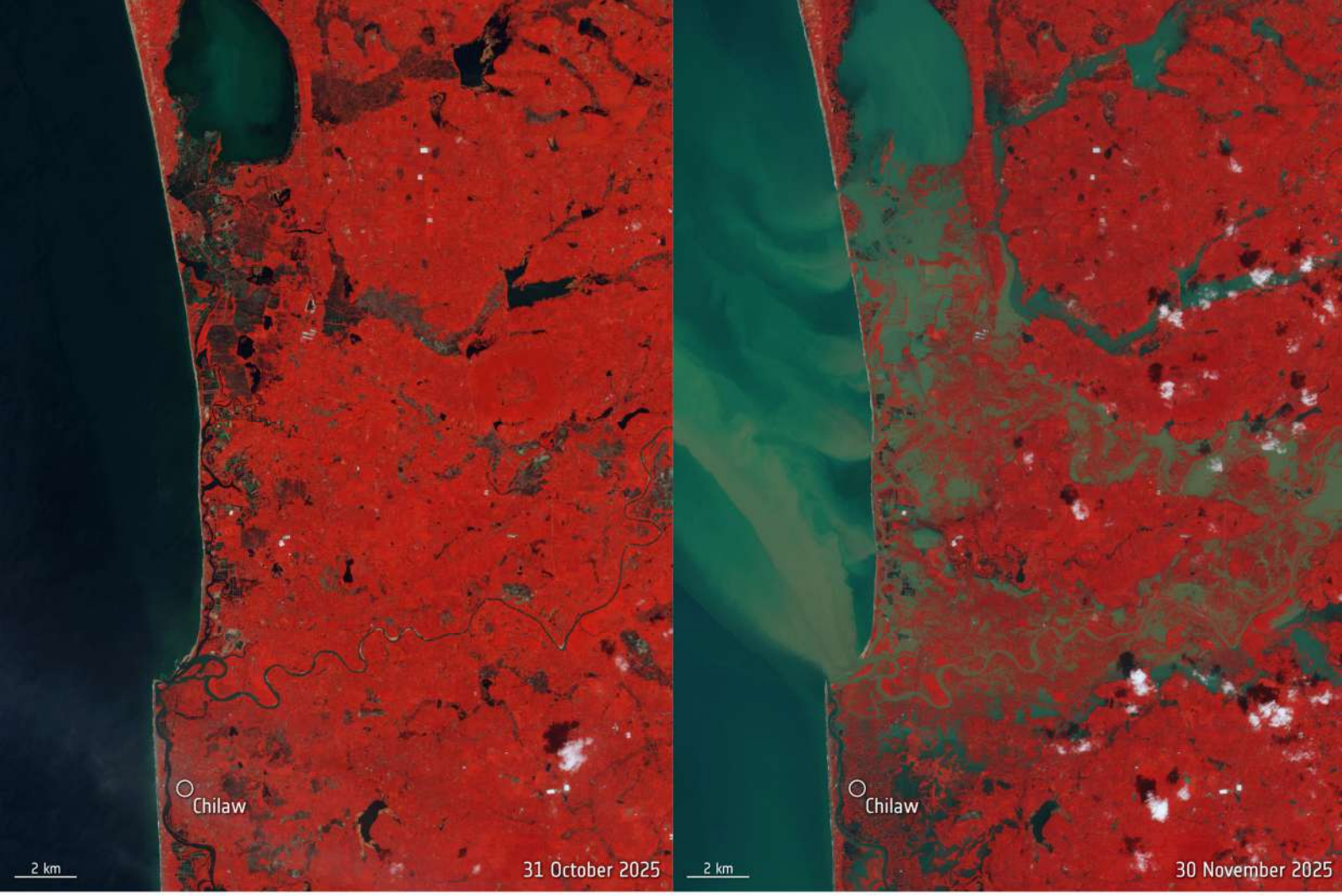

Civil Engineering Undergraduate Research Symposium

(CEURS)

2025

Proceedings

Department of Civil Engineering
University of Peradeniya
ISSN 3021-6737

PROCEEDINGS OF THE CIVIL ENGINEERING UNDERGRADUATE RESEARCH SYMPOSIUM (CEURS) - 2025

DEPARTMENT OF CIVIL ENGINEERING
FACULTY OF ENGINEERING
UNIVERSITY OF PERADENIYA
SRI LANKA

DEPARTMENT OF CIVIL ENGINEERING
FACULTY OF ENGINEERING
UNIVERSITY OF PERADENIYA
SRI LANKA

PROCEEDINGS OF THE CIVIL ENGINEERING UNDERGRADUATE RESEARCH SYMPOSIUM
CEURS 2025

Editor: SASP Sathurusinghe

Cover: SASP Sathurusinghe. Image: Flooding in Sri Lanka, contains modified Copernicus Sentinel data (2025), processed by ESA, CC BY-SA 3.0 IGO. Line art by Kanin Abhiromsawat at Vecteezy.com, coloured by SASPS.

First published in March 2026 by The Faculty of Engineering, University of Peradeniya, Sri Lanka.

ISSN 3021-6737

PUBLISHED BY,
DEPARTMENT OF CIVIL ENGINEERING,
FACULTY OF ENGINEERING,
UNIVERSITY OF PERADENIYA,
SRI LANKA.

Message from the Dean, Faculty of Engineering

It is with great pleasure that I congratulate the Department of Civil Engineering and the final-year undergraduates of the 2024/2025 academic year on the publication of these Proceedings.

The Faculty of Engineering, one of the nine Faculties of the University of Peradeniya, was established in 1950 and is the first engineering faculty in Sri Lanka. With eight academic departments, over 100 permanent academic staff members holding doctoral qualifications from world renowned universities, and well-established laboratory facilities, the Faculty has consistently maintained its position as a leader in high quality engineering education in the country.

The academic staff of the Faculty regularly produce research of international relevance, as reflected in publications in leading peer-reviewed journals. The guidance and training provided by such experienced academics have enabled our undergraduate students to achieve recognition at both national and international levels. These proceedings, which compile selected extended abstracts, not only demonstrate the knowledge and skills of our students but also reflect the Faculty's continued efforts to strengthen its facilities and academic environment in order to cultivate the competencies required of future researchers and professional engineers.

In this regard, I thank the Head of the Department and the organizers of CEURS 2025 for conducting a successful symposium and for making these proceedings available in open-access format, thereby enabling wider dissemination of the research carried out at the Department of Civil Engineering, University of Peradeniya.

Prof. Lilantha Samaranayake
Dean / Faculty of Engineering,
University of Peradeniya.

Message from the Head, Department of Civil Engineering

The Department of Civil Engineering is pleased to present this volume of the CEURS Proceedings, which contains selected extended abstracts of research conducted by final-year undergraduates during the 2024/25 academic year.

Undergraduate research projects form an important component of the four-year academic curriculum in Civil Engineering at the University of Peradeniya and contribute to the development of critical thinking, analytical ability, creativity, and intellectual independence among graduating engineers. The work compiled in this volume comprises investigations on diverse topics in Civil Engineering, undertaken over two semesters, and reflects the commitment, curiosity, and technical competence of our students in conducting academic research.

I congratulate the students whose work is included in these proceedings on the successful completion and presentation of their research. I also acknowledge the academic staff who supervised these projects and provided guidance in systematic research and scholarly practice.

My sincere thanks are extended to the editor, Dr. S. A. S. P. Sathurusinghe, and his team for compiling these proceedings and facilitating the dissemination of the research outcomes to a wider audience.

Prof. K. K. Wijesundara
Head / Department of Civil Engineering,
Faculty of Engineering,
University of Peradeniya.

Editorial Note

I am pleased to present the Proceedings of the Civil Engineering Undergraduate Research Symposium (CEURS 2025). This publication collates selected extended abstracts from research conducted by final-year undergraduate students during the 2024/2025 academic year. The abstracts span a broad range of topics in Civil Engineering and are organised in these Proceedings under the thematic areas of Geotechnical and Transportation Engineering, Material and Structural Engineering, and Water and Environmental Engineering. I take this opportunity to congratulate the students whose work is included in this volume.

I sincerely appreciate the guidance and support of the Dean of the Faculty of Engineering, Prof. Lilantha Samaranayake, and the Head of the Department of Civil Engineering, Prof. K.K. Wijesundara, in making these Proceedings possible and ensuring the success of CEURS 2025. I also acknowledge Dr. M. M. G. T. De Silva, Editor of the previous volume of CEURS, for her assistance and support in the preparation of this publication. My thanks are extended to Ms. W.M.P.H. Senevirathna for her editorial assistance.

Finally, I thank the final-year students and the academic staff of the Department of Civil Engineering for their collaborative efforts in research and for contributing their work to these Proceedings.

Dr. S. A. S. P. Sathurusinghe
Editors of CEURS 2025
Department of Civil Engineering
Faculty of Engineering
University of Peradeniya

Table of Contents

Geotechnical and Transportation Engineering

Material and Structural Engineering

Water and Environmental Engineering

Geogrid on a slope, Photo by Werner W Müller and Fokke Saathoff, cropped
CC BY 3.0

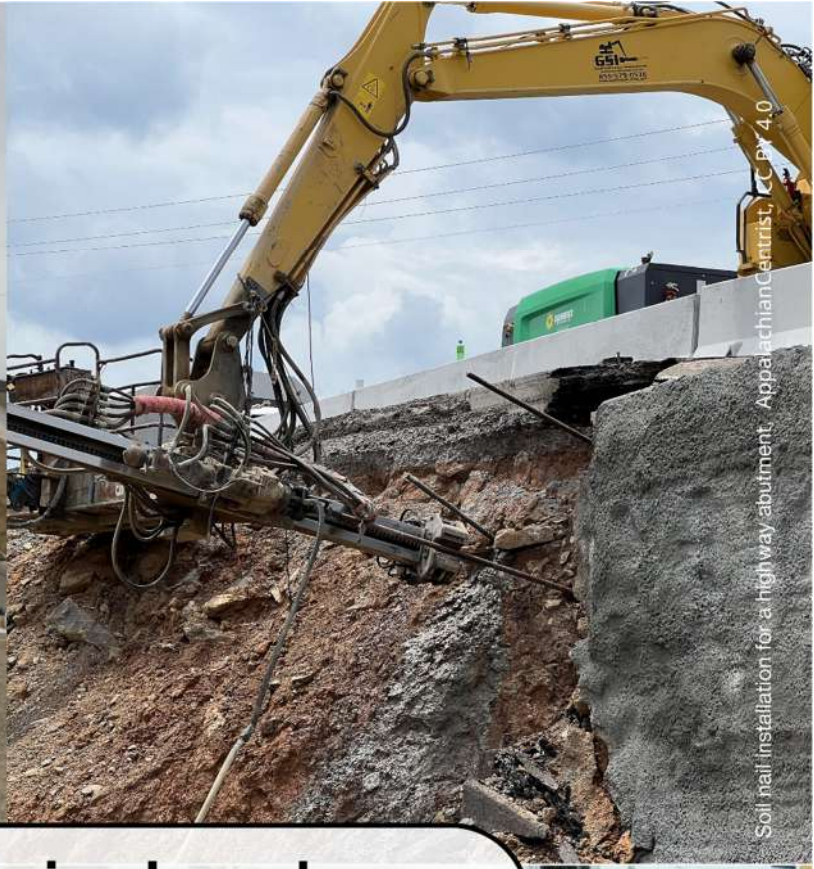

Soil nail installation for a highway abutment, AppalachianEntrist, CC BY 4.0

Geotechnical and Transportation Engineering

Gridlock at the intersection of 1st Avenue and 57th Street in New York City, Photo by Rgoodin CC BY-SA 3.0

HEAVE OF SUBGRADES STABILIZED OPTIMALLY USING CEMENT, LIME AND FLY ASH

A. T. M. Silva*[1], M. G. G. I. U. Siriwardane[1], L. C. Kurukulasuriya[1] and M. C. M. Nasvi[1]

[1]Department of Civil Engineering, University of Peradeniya, Sri Lanka

* e19373@eng.pdn.ac.lk

Abstract

This study investigates the heave characteristics of optimally stabilized expansive soil subgrades using cement, lime and fly ash. The research aims to identify expansive soil characteristics, determine the optimum stabilizer mix proportions of cement, lime and fly ash based on unconfined compressive strength (UCS) of 7-day air cured samples and evaluate heave characteristics of expansive soils stabilized optimally using the same agents using a laboratory scale model and compare with an analytical solution. The proposed methodology involves comprehensive soil characterization through various tests, including Atterberg limits, free swell index, Proctor compaction, particle size distribution, UCS and swelling pressure tests. The optimal mix proportions of cement and fly ash were determined using the UCS test, while the optimal lime content was determined through the pH test, targeting a pH value of 12.4 in the lime-soil mixture. The mix of 3% lime, 2.5% cement, and 15% fly ash showed the best results, with significant reduction in swell potential and improved strength. A laboratory scale physical model simulated subgrade behavior under variable ground water levels and the heave predictions using an analytical method were compared with the observed values. The study showed that 2.5% cement mixture exhibited the lowest swell compared to lime and fly ash.

Keywords: Heave, Stabilization, Swell pressure, Expansive soils

1. Introduction

Expansive soils are highly problematic soils that undergo large volume changes due to fluctuations in the moisture content. In addition, expansive soils contain a significant amount of Montmorillonite clay mineral which exhibits higher cation exchange capacity. High Montmorillonite mineral content of the expansive soils leads to swelling due to water absorption and shrinking due to water evaporation. This behaviour leads to the development of cracks and affects the stability of foundations and structures. Soil stabilization is used to enhance the strength, reduce compressibility, and modify other soil characteristics. Various additives are used for chemical stabilization such as lime, cement, fly ash. This study which is based on expansive soil samples collected in Dambulla, Central Province of Sri Lanka, the influence of soil stabilization using optimal mix proportions of cement, lime and fly ash on heave characteristics is investigated through a laboratory test series including model tests and an analytical method.

2. Literature review

2.1 Characteristics of expansive soil

Identification and characterization of expansive soils is basically based on laboratory experiments. Asuri and Keshavamurthy (2016) identified the characteristics of expansive soil based on physical, strength and gradation characteristics. Atterberg limits, free swell index, Proctor compaction, unconfined compressive strength and swell pressure tests were conducted for this purpose.

2.2 Soil stabilization with cement

Abbey et al. (2020) and Rai et al. (2021) highlighted the effectiveness of Ordinary Portland Cement (OPC) in stabilizing expansive clay soils. Their findings showed that incorporating 5% to 6% OPC significantly reduced plasticity, swell potential, and swelling pressure while improving unconfined compressive strength (UCS). Abbey et al. (2020) also observed microstructural changes and enhanced soil behaviour, while Rai et al. (2021) demonstrated that optimal cement-fly ash blends yielded strength gains and volumetric stability. Both studies supported 6% OPC as a cost-effective, practical solution for improving high-plasticity subgrade soil.

2.3 Soil stabilization with lime

Suhail et al. (2007) highlighted that a pH of 12.4 is critical to initiate pozzolanic reactions in lime-treated soils, with 4% lime achieving this threshold and significantly reducing swell pressure. Consoli et al. (2011) supported this by using the Initial Consumption of Lime (ICL) test, confirming that stabilization effectiveness depends on reaching the required pH level. Both studies emphasized that 5% to 6% lime content ensured optimal strength gain and long-term improvement in expansive soil behaviour.

2.4 Soil stabilization with fly ash

Fly ash significantly improves the engineering behaviour of expansive soils by reducing swell potential and enhancing unconfined UCS. Zha and Liu (2008) observed that increasing fly ash-lime content, along with adequate curing time, notably reduced swelling pressure and free swell. Rai et al. (2021) reported that combining 25% fly ash with around 5% cement yielded substantial improvements in UCS and volumetric stability. Both studies confirmed that fly ash, particularly when blended with cement or lime, is highly effective for expansive soil stabilization.

2.5 Heave prediction techniques

Heave prediction is essential for assessing the upward movement of expansive soils due to moisture changes. Dhowian (1990) outlined four laboratory methods based on swell pressure, void ratio, and stress paths to estimate vertical expansion. These methods, supported by empirical and analytical models, incorporated parameters like swell index, soil suction, and moisture variation. Yoshida et al. (1983) developed a model linking heave to changes in void ratio, stress states, and moisture content, validated through field data in Regina, Canada. Accurate prediction improves foundation design by reducing structural risks from soil swelling and enhancing infrastructure resilience in expansive zones.

3. Methodology

3.1 Introduction

The methodology is based on laboratory testing to determine soil characteristics, identifying optimal stabilizer mix ratios and developing a laboratory-scale model to simulate and measure soil heave under varying ground water levels.

3.2 Sample collection and laboratory testing

Soil samples were collected from Dambulla, Sri Lanka. Particle size distribution, Atterberg limits tests, free swell index test, swell pressure test, modified Proctor compaction test and UCS test were conducted on untreated samples to characterize the raw soil. Then, the soil samples were treated with cement (2%, 2.5%, 5%, 8%) and fly ash (10%, 15%, 20%). The treated samples were then air cured for a period of 7 days. Once cured, UCS test was conducted on stabilized samples to find the optimal stabilizer proportions of cement and fly ash. pH test was conducted on lime-treated (0%, 2%, 3%, 5%, 7%) samples to find the optimal lime content. For the stabilization, cement, lime, and fly ash were added to the soil in the optimal proportions: 2.5% cement, 3% lime, and 15% fly ash by dry weight of the soil. The treated samples were then air cured for a period of 7 days. Once cured, the stabilized samples underwent further laboratory testing of UCS and swell pressure tests to measure compressibility and swelling characteristics.

3.3 Laboratory scale model

Soil was compacted into four CBR moulds. These included one compacted with untreated raw soil and the other three compacted with soil mixtures containing the selected optimal additive percentages of Cement (2.5%), Lime (3%), and Fly Ash (15%). Each treated sample was compacted at MDD according to standard compaction procedures and cured for 7 days to simulate field stabilization conditions. After the curing period, all four CBR moulds were placed together in a controlled water tank setup. The objective was to simulate moisture infiltration and observe the swell behaviour in a more stable and measurable environment. Water was introduced gradually from the bottom of the tank to ensure uniform upward saturation. Heave of all soil samples was measured with time using displacement transducers.

3.4 Analytical method

To evaluate the heave analytically, a structured methodology was adopted. This approach begins with the division of the soil profile into multiple distinct layers, each possessing unique heave characteristics dependent on the effective vertical stress. These properties were denoted as SW_1

through SW_n for the respective layer. The next step involved the calculation of the effective vertical stress exerted on each soil layer. This was accomplished using Equation 1,

$$\sigma_{v\,i} = \gamma' h_i \quad (1)$$

where σ_{vi} represents the effective vertical stress at mid-height of i^{th} layer, γ' is the effective unit weight of the soil, and h_i is the height of the specific soil layer. To further quantify the swell, the corresponding swelling percentage for each vertical stress value is determined. This was performed by referring to the swell pressure test results. Once the swelling percentages were determined for each layer, the total heave of the soil profile was computed using Equation 2.

$$\Delta H = \sum_{i=0}^{n} SW_i \times Z_i \times 100 \quad (2)$$

In this equation, ΔH represents the total heave, SW_i denotes the swell percentage at depth Z_i, where Z_i is the depth to the mid-height of a soil layer. By summing up the contributions of all layers (i=0 to n), the total heave due to soil swelling was determined.

4. Results and Discussion

4.1 Experimental results

Table 1 showed the characteristics of raw soil. The soil has a high swell potential based on the liquid limit (Chen, 1965) and according to the plasticity index (IS 1498, 1970), the soil is classified as having a high swell potential. Additionally, according to the FSI, soil can be categorized as high expansivity (IS 1498, 1970). Raw soil can be categorized as CI (Clay of Intermediate plasticity) according to the British Soil Classification System.

Table 1: Raw soil characteristics

Characteristics	Value
Free Swell Index (FSI)	1.25
Liquid limit (LL)	49
Plastic limit (PL)	17
Plasticity Index (PI)	32
Optimum Moisture Content	12.2%
Maximum Dry Density	18.8 kN/m^3
Swell Pressure	295 kPa
Unconfined Compressive Strength (UCS)	230 kPa

As shown in Figure 1, the critical point for pozzolanic activity, identified at pH 12.4, was reached when the lime content is approximately 3%. Therefore, the optimal lime content for soil was considered as 3%.

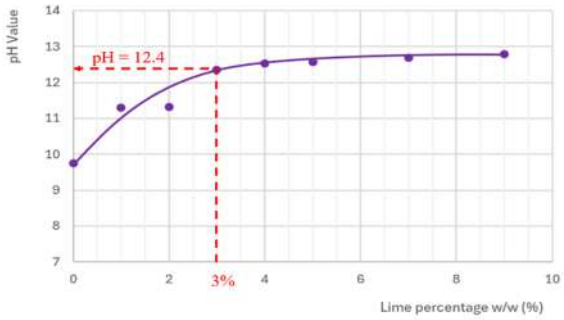

Figure 1: pH Curve for Lime-Soil Mixture

Table 2 shows the Unconfined Compressive Strength values of different percentages of soil stabilized samples.

Table 2: Unconfined Compressive Strength of stabilized samples

Stabilizer	UCS (kPa)
Lime (3%)	1152
Cement (2%)	435
Cement (2.5%)	587
Cement (5%)	1348
Cement (8%)	2855
Fly Ash (10%)	511
Fly Ash (15%)	682
Fly Ash (20%)	531

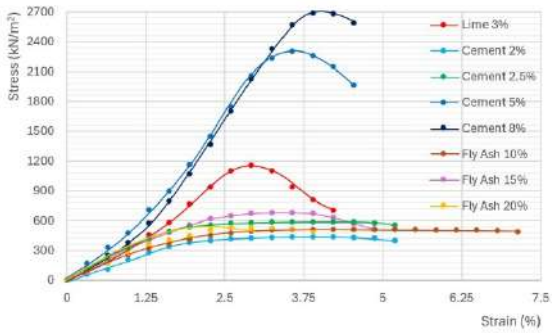

Figure 2: Variation of UCS with Strain for Stabilized Soil

As shown in Figure 2, based on the highest UCS values achieved, the optimum stabilizer content of fly ash is 15%. And the optimal stabilizer content of cement is 2.5%, which corresponds well with the UCS results obtained for lime and

fly ash. Table 3 shows the swell pressure of raw soil and soil samples stabilized with optimal percentages of lime, fly ash, and cement.

Table 3: Swell pressure of raw soil and stabilized samples

Stabilizer	Swell pressure (kPa)
Raw	295
Lime (3%)	271
Fly Ash (15%)	157
Cement (2.5%)	53

As shown in Figure 3, based on these results, cement 2.5% was found to be the most suitable stabilizer in terms of reducing swell pressure, making it the most appropriate choice for improving expansive soils under road pavements.

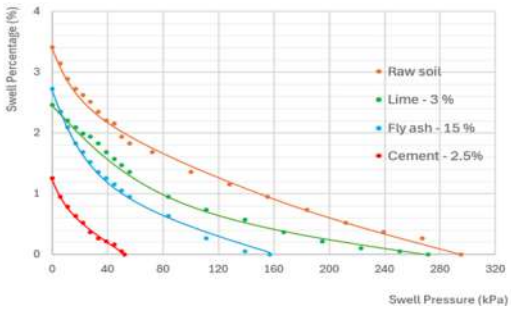

Figure 3: Variation of Swell Pressure with Swell Percentage

4.3 Comparison of Theoretical and Experimental Results

As shown in Figure 4, the variation exists because theoretical calculations assume that soil properties stabilize after 7 days, while in practice, chemical reactions and strength development continue beyond that period.

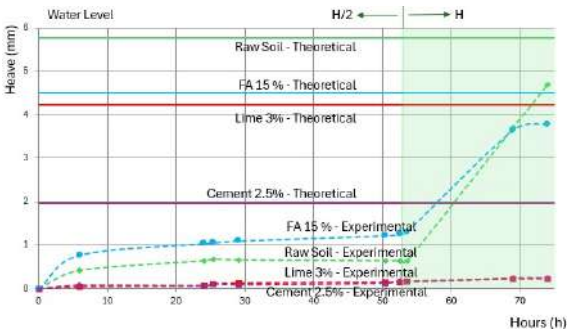

Figure 4: Variation of heave with time

Measured heave is lower since the soil keeps gaining strength during saturation. This shows that stabilization effects improve over time, reducing heave more than the predicted.

5. Conclusions

- From the experimental results, it can be concluded that cement, even at minimum optimum UCS value (587 kPa at 2.5%), resulted in the lowest swell among all three stabilizers.
- The laboratory scale model also exhibited the least swell for cement stabilized expansive soil.
- Considering both the UCS and swell behaviour, cement proved to be the most effective stabilizer due to its high strength and minimal swelling characteristics.

References

Asuri, S. and Keshavamurthy, P. (2016). Expansive Soil Characterisation: an Appraisal. *INAE Letters*, 1(1), pp.29–33.

Consoli, N.C., Lopes Jr, L.S., Prietto, P.D.M., Festugato, L. & Cruz, R.C. (2011) 'Variables Controlling Stiffness and Strength of Lime-Stabilized Soils', Journal of Geotechnical and Geoenvironmental Engineering, 137(6), pp. 628–632.

Dhowian, A.W. (1990). Heave Prediction Techniques and Design Consideration on Expansive Soils. Journal of King Saud University - Engineering Sciences, [online] 2(2), pp.355–376.

Rai, P., Qiu, W., Pei, H., Chen, J., Ai, X., Liu, Y. and Ahmad, M. (2021). Effect of Fly Ash and Cement on the Engineering Characteristic of Stabilized Subgrade Soil: An Experimental Study. *Geofluids*, 2021, pp.1–11.

Suhail, Muzahim Al-Mukhtar and Jean-Marie Fleureau (2007). Long-Term Stability Characteristics of a Lime-Treated Plastic Soil. *Journal of Materials in Civil Engineering*, 19(4), pp.358–366.

Yoshida, R.T., Fredlund, D.G. and Hamilton, J.J. (1983). The prediction of total heave of a slab-on-grade floor on Regina clay. *Canadian Geotechnical Journal*, 20(1), pp.69–81.

Zha, F., Liu, S., Du, Y. and Cui, K. (2008). Behavior of expansive soils stabilized with fly ash. *Natural Hazards*, 47(3), pp.509–523.

COLLAPSIBILITY CHARACTERISTICS OF RESIDUAL SOILS SUBJECTED TO LEACHING AND ITS EFFECT ON THE STABILITY OF SLOPES

R.K.P.U.G. Keerthisinghe*[1], W.M.B.L. Wickramasinghe[1] and L.C. Kurukulasuriya[1]

[1]Department of Civil Engineering, Faculty of Engineering, University of Peradeniya, Sri Lanka

*e19195@eng.pdn.ac.lk

Abstract

Residual soils are widely distributed in tropical regions such as Sri Lanka, where prolonged weathering processes result in soils with heterogeneous properties and complex behavior. These soils are particularly susceptible to leaching, a geochemical process that removes soluble minerals and salts. Leaching significantly impacts slope stability by altering key soil characteristics, including particle size distribution, liquid limit, collapse potential, and shear strength parameters. This study investigated the effects of leaching on the properties of a selected residual soil, focusing on its collapsibility and slope stability. This research employed both experimental and numerical approaches. Experimentally, fundamental soil properties such as particle size distribution, Atterberg limits, collapse potential, and shear strength parameters were determined using standard laboratory tests. Variations in these properties before and after leaching were analyzed to quantify the impact of leaching intensity and hydraulic gradient. Numerically, slope stability analyses were conducted using GeoStudio Slope/W software, simulating different slope geometries and incorporating the derived shear strength parameters to assess the stability of slopes under varying conditions. The findings from this study will contribute to a deeper understanding of how leaching effects on the collapsible characteristics of residual soils and stability of slopes.

Keywords: Residual Soils, Soil characteristics, Leaching process, Slope stability

1. Introduction

Residual soils are especially sensitive to environmental changes, with leaching being a major concern. When water percolates through the soil, it removes fine particles and soluble compounds like clays and carbonates, weakening the soil's internal framework. This often leads to a loss of strength, increased compressibility, volume reduction, all of which can increase slope instability and landslides. This research investigates how leaching affects the structural integrity of residual soils and subsequently influences slope stability.

2. Literature review

Residual soils, common in tropical regions, are highly porous, have low cohesion, and possess a metastable structure, making them vulnerable to moisture-induced collapse (Rahardjo et al., 2012). Leaching removes fine particles and soluble minerals, increasing void ratios and reducing shear strength which heightens collapse potential (Fattah et al., 2019). The degree of collapsibility is influenced by factors such as mineralogy, initial soil structure, permeability, and the duration and intensity of water infiltration. Slope stability analyses will be performed using GeoStudio SLOPE/W software simulating different slope geometries and incorporating strength parameters derived from the leaching tests (Gasmo et al., 2000).

3. Methodology

The methodology followed in this study is illustrated in Figure 1.

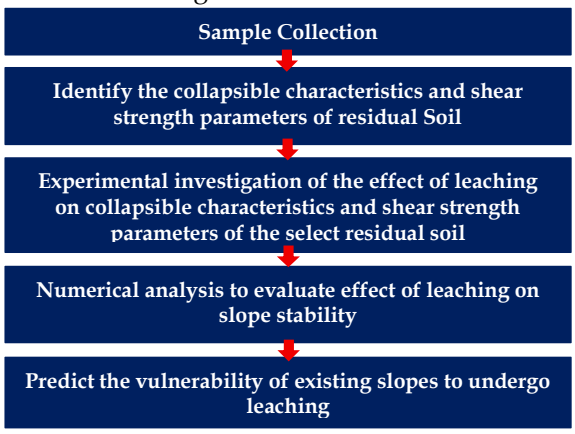

Figure 1: Methodology

3.1 Experimental Work

3.1.1 Sample Collection

Undisturbed soil samples were collected from Muruthagahamula in Gelioya, Sri Lanka. (GPS Coordinates of 7.206719°N, 80.591559° E)

3.1.2 Characterization Testing

Geotechnical properties of the raw soil were evaluated by performing tests including Sieve and Hydrometer tests (BS 1377: Part 2: 1990), Atterberg limit tests (BS 1377: Part 2: 1990), Specific gravity test (BS 1377: Part 2: 1990), Collapse Index (ASTM D5333) and Direct Shear Test (BS 1377: Part 2:1990).

3.1.3 Leaching Process

Undisturbed samples were subjected to seepage flow under two hydraulic gradients (i1(8.29) and i2(15.44)) for different degrees of leaching due to seepage flow defined by the replaced pore volume ratio.

Table 1: Pore Volume Ratio of Samples

Hydraulic gradient	Sample Number	Pore volume ratio
	Reference	0.00
8.29	Sample 01	1.48
	Sample 02	2.11
	Sample 03	2.36
	Sample 04	4.35
	Sample 05	8.13
15.44	Sample 06	0.91
	Sample 07	1.67
	Sample 08	2.71
	Sample 09	4.19
	Sample 10	6.15

3.1.4 Soil Characterization of Leached Samples

Geotechnical properties of the leached soil samples were evaluated by performing tests including Sieve and Hydrometer tests (BS 1377: Part 2: 1990), Atterberg limit tests (BS 1377: Part 2: 1990), Specific gravity test (BS 1377: Part 2: 1990), Collapse Index (ASTM D5333) and Direct Shear Test (BS 1377: Part 2:1990) to determine the effect of leaching on soil properties.

3.2 Numerical Analysis

To investigate the influence of leaching on slope stability, a series of numerical models were created using GeoStudio Slope/W software representing slopes with varying heights (4 m, 8 m, and 12 m) and slope angles (30°, 45°, 60° and 75°).

4. Results and Discussion

4.1 Characterization Test Results of Raw Soil

Results of the raw soil characterization are given in Table 2.

Table 2: Results of characterization testing

Property	Value
Specific gravity	2.71
Bulk density	1538.3 Kg/m^3
Cohesion (c)	61.6 KPa
Friction angle (φ)	39.4°
Liquid limit	41
Plastic Limit	Non - plastic

As shown in Table 2, the Liquid limit was 41%. Figure 2 shows that less than 35% of the particles were smaller than 0.06 mm, according to the British Soil Classification System (BSCS). Accordingly, the soil was classified as Very silty sand of intermediate plasticity (SMI).

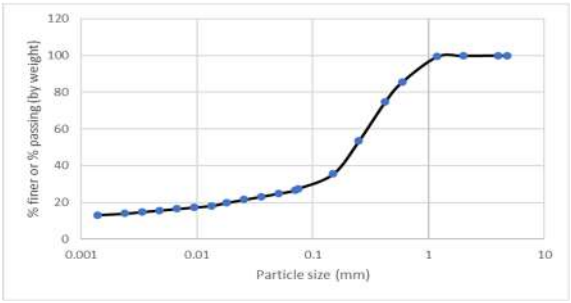

Figure 2: The particle size distribution of raw soil

4.2 Results of Leached Samples

4.2.1 Sieve and Hydrometer Tests

Variation of Particle size distribution of raw soil and leached samples under two hydraulic gradients (i1(8.29) and i2(15.44)) for different degrees of leaching shown in Figure 3 and 4.

Under moderate leaching at i_1, the PSD curve shows minimal shift with a fine reduction of about 5-10%, while aggressive leaching at i_2 causes a significant rightward shift in the PSD curve, especially for particles smaller than 0.075 mm, leading to a fines loss of 15-20%.

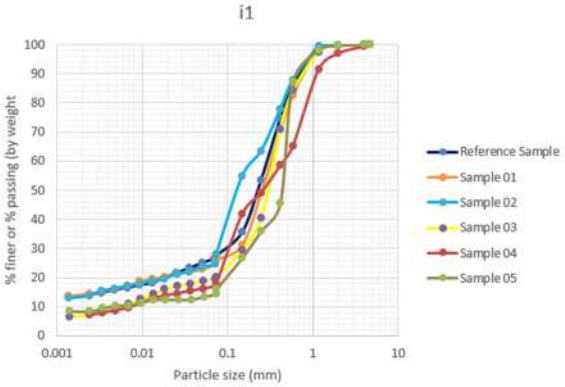

Figure 3: Particle Size Distribution of Samples under Hydraulic Gradient 1

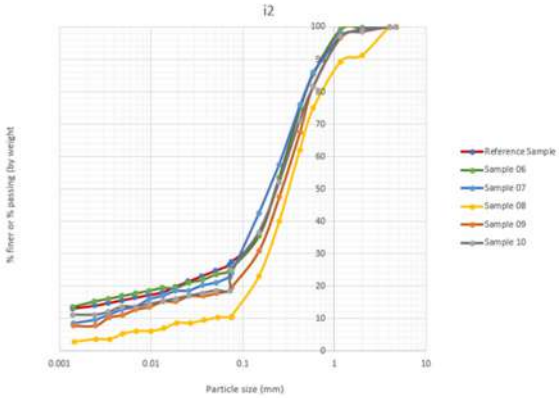

Figure 4: Particle Size Distribution of Samples under Hydraulic Gradient 1

4.2.2 Direct Shear Test

The shear strength of soils is primarily governed by two key parameters: cohesion (c) and internal friction angle (φ). Results of soil samples are given in Table 3.

Table 3: Shear Strength Parameters of raw soil and leached samples

Sample Number	Cohesion	Friction angle
Reference	61.6	39.4
Sample 01	58.2	41.7
Sample 02	57.5	41.4
Sample 03	53.7	45.6
Sample 04	54.3	32.6
Sample 05	52.3	33.0
Sample 06	58.8	40.0
Sample 07	54.2	36.1
Sample 08	56.2	35.8
Sample 09	53.5	33.8
Sample 10	50.2	42.3

Experimental results from the study reveal that both cohesion and internal friction angle are significantly affected by leaching, with higher hydraulic gradients leading to more pronounced reductions. In the reference sample (unleached), indicating relatively high shear strength due to intact interparticle bonding and cementation. However, under moderate leaching conditions (hydraulic gradient i_1 = 8.29), these values showed a gradual decline and under higher hydraulic gradient (i_1 = 15.44) the degradation became more severe.

4.2.3 Atterberg Limits Test

Liquid Limit of raw soil and leached samples under two hydraulic gradients (i1(8.29) and i2(15.44)) for different degrees of leaching shown in Table 4.

Table 4: Liquid Limit of raw soil and leached samples

Sample No.	Ref.	01	02	03	04	05
LL (%)	41	48	36	42	43	40

Sample No.	06	07	08	09	10
LL (%)	43	44	45	45	43

The reference sample had an initial liquid limit of 41%. Under moderate leaching at i1, the liquid limit showed significant fluctuations, ranging from a low of 36% to a high of 48%, indicating erratic behavior likely due to partial dissolution of cementing agents and redistribution of fine particles. In contrast, leaching at i2 resulted in a more consistent upward trend in liquid limit, with values increasing progressively from 43% to a peak of 45% but slightly declining to 43% at 6.15 pore volume replaced.

4.2.4 Collapse Index Test

Results of Collapse Index test for raw, leached Soil is shown in Figure 5 and Figure 6.

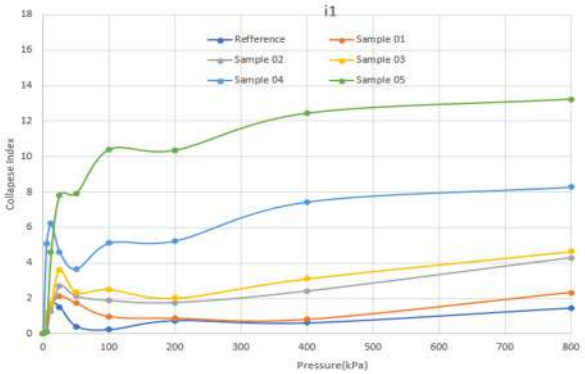

Figure 5: Collapse Index variation of Samples under Hydraulic Gradient 1

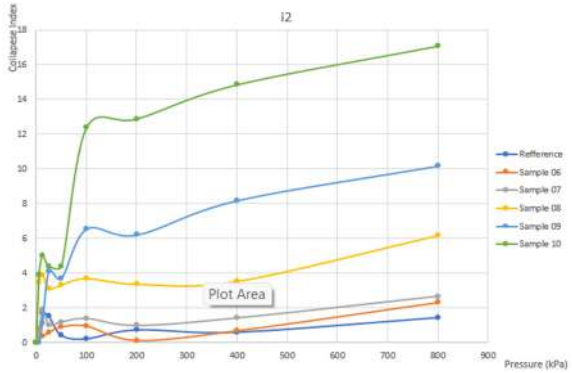

Figure 6: Collapse Index variation of Samples under Hydraulic Gradient 2

At lower hydraulic gradient (i_1=8.29), the collapse potential shows gradual increases with increasing pore volume replacement. This indicates that while leaching causes some dissolution of cementing materials, the structural degradation is relatively slow. At higher hydraulic gradient (i_2 = 15.44), the collapse potential exhibits a more significant increase compared to i_1. This suggests that higher flow velocities accelerate the leaching process, leading to faster dissolution of cementing agents and greater structural degradation.

4.3 Numerical Analysis

Factor of Safety values correspond to insitu soil conditions and leached samples under hydraulic gradients of 8.29 and 15.44 were calculated for each slope height and gradient combination, using SLOPE/W simulations. The variation in FOS of samples represents in Figure 7.

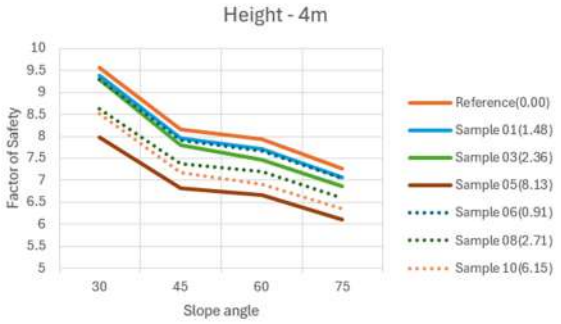

Figure 7: FOS of Samples for 4 m height

5. Conclusions

- Leaching significantly altered key soil properties. The data showed that cohesion and friction angle decreased, while the Collapse Index increased. Specifically, cohesion reduced by up to 18% under the higher hydraulic gradient (i_2=15.44), and the friction angle decreased by as much as 4.5°. The collapse index increased by up to 66%, indicating a higher potential for structural collapse. The liquid limit exhibited inconsistent behavior under moderate leaching but increased consistently under higher gradients.
- Higher hydraulic gradients intensified soil degradation by causing greater loss of fine particles, which led to further reduction in soil strength.
- The Factor of Safety (FOS) decreases with increased leaching intensity, with more severe reductions observed for higher slopes (e.g., 8 m and 12 m). The effect is especially pronounced under higher hydraulic gradients, indicating that slope vulnerability is strongly influenced by leaching severity.

These findings highlight the critical importance of considering leaching-induced degradation in geotechnical design and slope stability assessments in tropical regions. Ongoing environmental exposure and rainfall-driven leaching pose serious challenges to long-term slope performance and safety.

References

Fattah, M.Y., Obead, I.H. and Omran, H.A. (2019). 'A Study on Leaching of Collapsible Gypseous Soils', *International Journal of Geotechnical Engineering*, 16(1), pp.44–54. doi: 10.1080/19386362.2019.1647664.

Gasmo, J.M., Rahardjo, H. and Leong, E.C. (2000). 'Infiltration Effects on Stability of a Residual Soil Slope', *Computers and Geotechnics*, 26(2), pp.145–165. doi: 10.1016/S0266-352X(99)00035-X.

Lommler, J.C. and Bandini, P. (2015). 'Characterization of Collapsible Soils', *IFCEE 2018*. doi: 10.1061/9780784479087.167.

Rahardjo, H., Satyanaga, A., Leong, E.-C., Ng, Y.S. and Pang, H.T.C. (2012). 'Variability of Residual Soil Properties', *Engineering Geology*, 141–142, pp.124–140. doi: 10.1016/j.enggeo.2012.05.00

MECHANICAL PROPERTIES OF RUBBER - BALLAST MIXTURES FOR RAILWAY APPLICATIONS

Sageepan K.[1,*], Sugananthan P.[1], and Navaratnarajah S. K.[1]

[1]Department of Civil Engineering, Faculty of Engineering, University of Peradeniya, Sri Lanka

* e19337@eng.pdn.ac.lk

Abstract

Railway transportation is essential in Sri Lanka. Railway ballast, made of crushed stone, provides track stability and load distribution but degrades over time due to repeated train loads and environmental effects. This study investigates shredded recycled tire rubber as a partial ballast replacement to improve performance and sustainability. Rubber inclusion enhances energy absorption, reduces particle breakage and noise, and offers an eco-friendly solution. The research aimed to determine the optimal rubber content (by weight) that improves mechanical performance without significantly reducing strength. Large-scale direct shear tests were conducted at normal stresses of 30, 60, and 90 kPa on fresh ballast and rubber–ballast mixtures with two rubber sizes (8–16 mm and 19–26.5 mm) at 10% and 15% replacement. Results showed particle breakage decreased by up to 45% (BBI), while peak shear stress reduced by 29–38%. Rubber also reduced dilation, improving stability by limiting particle movement and maintaining a compact structure. A calibrated DEM simulation modeled particle behavior and supported a parametric study to identify the most effective rubber content. Overall, shredded rubber improves ballast durability, reduces maintenance, and promotes sustainable tire recycling in Sri Lanka.

Keywords: Railway ballast, Crumb rubber, Shear strength, DEM

1. Introduction

Railway tracks in Sri Lanka predominantly rely on traditional ballast systems, which deteriorate under cyclic loading and environmental exposure. This leads to high maintenance costs and reduced track performance. The increasing volume of discarded tires presents an environmental challenge that can be addressed by integrating crumb rubber into ballast systems. This study investigates the mechanical behaviour of rubber-ballast mixtures as a sustainable alternative to traditional ballast track system, focusing on strength, elasticity, breakage resistance, and energy absorption.

2. Literature review

Several studies have been conducted to explore alternative materials for enhancing the mechanical performance of traditional railway ballast. Research has shown that incorporating crumb rubber into railway ballast improves mechanical performance by enhancing energy dissipation, reducing vibration, and minimizing particle breakage (Sol-Sánchez et al., 2015, Indraratna et al., 2021). Optimal results are typically achieved with 10–15% rubber content and particle sizes between 8–16 mm or 19–26.5 mm (Arachchige et al., 2022). Large-scale direct shear and impact tests confirm improved behaviour, while Discrete Element Modelling (DEM) has effectively replicated particle interactions and validated experimental outcomes in the previous studies related to the addition of rubber to the traditional ballast track. Though promising, excessive rubber content may affect drainage and interlocking, and further full-scale field studies are needed to assess long-term performance. Additionally, many studies have also being done related to the hydraulic conductivity of traditional track system in addition with the rubber from the waste tires.

3. Methodology

3.1 Experimental

The experimental method involved conducting large-scale direct shear tests on both conventional ballast and rubber-intermixed ballast systems under three different normal stress levels, as previously mentioned. The tests also considered two different percentages and sizes of rubber particles. By following the Indian Standard (IS) specifications, Sri Lankan railway projects maintain uniformity in aggregate quality, which supports effective interlocking, proper drainage, and long-term durability of the track system. Figure 1 shows the particle size distribution of ballast within the limits specified by the Indian Standard.

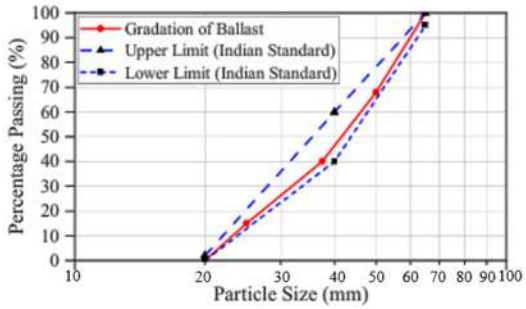

Figure 1: Particle size distribution based on the Indian Standard

Sample preparation for this study involved several crucial steps to ensure consistent and accurate experimental results. First, ballast samples, ranging from 19 mm to 63 mm, were collected from the Gampola Railway Ballast Stockyard. These samples were then manually sieved in the laboratory and the particle size distribution requirements, categorizing them into four distinct groups: 19–25 mm, 25–37.5 mm, 37.5–50 mm, and 50–63 mm. To remove dust and fine particles acquired from the open stockyard, the sieved ballast was thoroughly cleaned by washing with clean water and subsequently dried under direct sunlight to eliminate any moisture that could affect testing. For large-scale direct shear tests, the ballast sample was divided into three distinct layers top, middle, and bottom to investigate particle breakage at different depths, with each layer marked using a unique colour (red, blue, or green) for post-test identification as shown in Figure 2. Finally, crumb rubber samples were prepared in two designated size ranges: 8–16 mm and 19–26.5 mm, and then mixed uniformly with the ballast in two proportions (10% and 15% by weight of the total ballast) to create consistent test specimens.

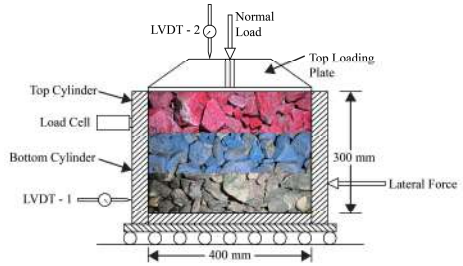

Figure 2: Cross section of particles arranged in the apparatus

3.2 Large-Scale Direct Shear Test

The large-scale direct shear test served as a key experimental method in this study, supported by numerical simulations, to assess the mechanical behaviour of rubber-ballast mixtures. As shown in the Figure 3, the test apparatus consisted of two cylindrical sections each 200 mm in diameter and 150 mm deep with the bottom cylinder sheared laterally at a constant rate of 4 mm/min. Normal stress was applied through a top loading plate using a lever-arm system with calibrated weights.

Figure 3: Large-scale apparatus used for the experimental purpose

Tests were performed under three stress levels: 30, 60, and 90 kPa. A load cell measured shear resistance at the top cylinder, while two LVDTs recorded vertical and horizontal displacements to track dilation, compression, and shear. Data from these instruments were captured every 10 seconds using a data logger. Samples were prepared directly inside the apparatus by manually compacting pre-weighed ballast and rubber in layers to achieve uniform density and realistic field conditions. Shearing continued until a shear of 60 mm (strain of 15%) was reached, in accordance with the experimental design.

3.3 Compression, Dilation & Breakage.

The large-scale direct shear tests revealed important behaviours of ballast-rubber mixtures, particularly in terms of dilation and compression. Dilation, or volume expansion during shearing, increased with rubber

inclusion due to rubber's flexible and elastic nature, which reduced particle interlocking and allowed greater lateral movement. Conversely, compression behaviour was influenced by the deformability of rubber, which affected load transfer and packing. To assess particle degradation, the Ballast Breakage Index (BBI) was calculated using sieve analyses conducted before and after testing. This allowed for a clear comparison of mechanical breakage across different mixtures.

3.4 Numerical Analysis

The numerical analysis played a key role in this study by replicating the conditions of large-scale direct shear tests and helping to understand particle behavior that is hard to observe through experiments alone. The Discrete Element Method (DEM), carried out using EDEM software, was chosen because it effectively simulates granular materials like railway ballast. Unlike traditional methods such as FEM or FDM, DEM captures individual particle movements, shape effects, and degradation under loading. As shown in Table 1, to improve accuracy, actual ballast and rubber particles used in experiments were 3D scanned using the software, refined and scaled, and then imported into numerical analysis as CAD templates.

Table 1: Real, scanned & generated particles during the numerical procedure

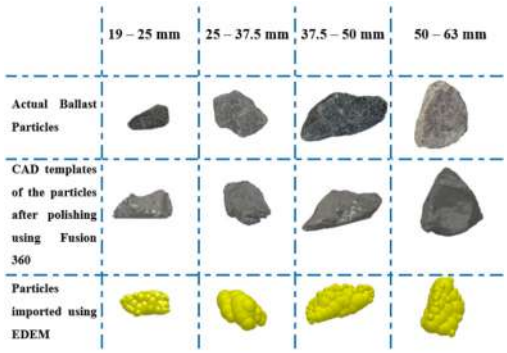

These particles were modelled using overlapping spheres and smoothed to maintain a balance between detail and computational efficiency. This approach allowed realistic simulation of particle interlocking, force transfer, offering reliable insight into material behavior during shear loading.

4. Results and Discussion

The study assessed rubber-ballast mixtures using large-scale direct shear tests and DEM simulations. Results showed that adding 10–15% shredded rubber reduced peak shear stress, dilation, energy dissipation, and particle breakage, while improving compressibility. Mohr–Coulomb analysis revealed a decrease in friction angle with more rubber. DEM simulations, calibrated with 3D-scanned particles, closely matched experimental outcomes, confirming the benefits of rubber in enhancing ballast performance and durability.

4.1 Shear Strain and Shear stress

The maximum shear stress of the sample is reduced with the addition of the rubber content. The stress further decreases with the addition of rubber up to 15%. The Figure 4 shows the variation of the stress with strain for the normal stress of 90 kPa. The addition of the rubber particles also reduces the energy dissipation from the track system as the rubber has the capacity to absorb energy. The area under the stress strain curve will give the energy dissipation from the track system.

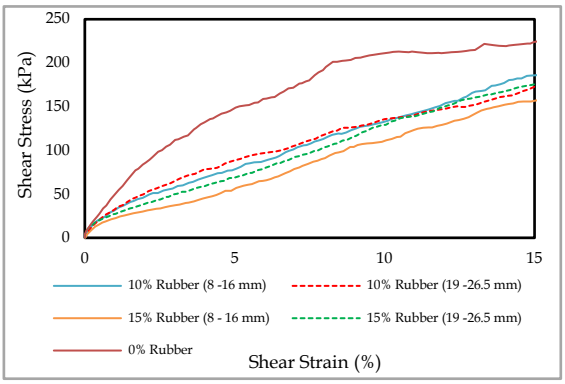

Figure 4: Variation of shear stress vs shear strain for the normal stress of 90 kPa

Table 2 shows the maximum shear stress values for the traditional ballast and the rubber intermixed ballast systems with different percentage and sizes of rubber for the normal stress of 90 kPa.

Table 2: Variation of maximum shear stress with rubber content

Material Type	Maximum Shear Stress (kPa)
Ballast Only	224.92
Rubber 10% (8 -16 mm)	190.33
Rubber 10% (19 – 26.5 mm)	174.06
Rubber 15% (8 -16 mm)	157.88
Rubber 15% (19 – 26.5 mm)	177.19

4.2 Dilation and compression

In traditional railway ballast, shear loading often leads to dilation due to particle interlocking and rearrangement. However, the addition of shredded rubber reduces this dilation effect. As rubber content increases, the mixture becomes more compressive and flexible. This change is attributed to the rubber particles' ability to deform and absorb part of the load. The Figure 5 illustrates the dilation and compression effect of the particles during loading of 90 kPa.

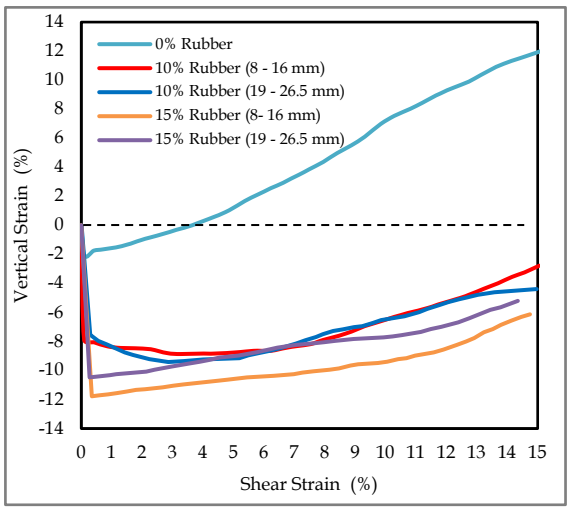

Figure 5: Variation of dilation and compression with rubber content

4.3 Ballast Breakage

Ballast particle breakage was notably observed under high normal stress due to increased contact forces, contributing to long-term degradation and reduced track stability. Figure 6 illustrates the variation of the Ballast Breakage Index (BBI) with different rubber content and size ranges. The addition of rubber significantly reduces the BBI compared to fresh ballast. For the 8–16 mm rubber size range, BBI decreased by 20% with 10% rubber and by 23% with 15% rubber. In the 19–26.5 mm range, the reduction is more pronounced—9% with 10% rubber and 46% with 15% rubber. This indicates that both higher rubber content and larger rubber sizes are more effective in minimizing ballast degradation. This is due to the added rubber's deformability cushions particle impacts, reducing breakage. The mixture becomes less brittle, better absorbing and distributing loads. As a result, breakage is minimized, enhancing the durability and resilience of the ballast system. Both BBI and the Breakage Ratio were used in this study.

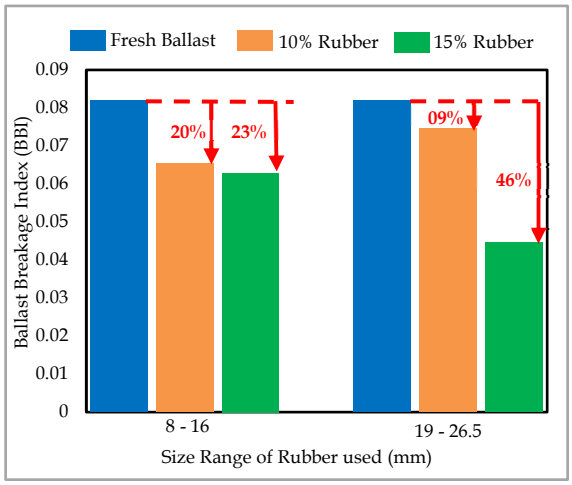

Figure 6: Variation of BBI with rubber content

5. Conclusions

Increasing the rubber content in the ballast mix led to reduced dilation, improving load stability. Peak shear stress dropped by 29–38% with 15% of this rubber size, while the friction angle showed a maximum reduction of 23% when 10% of 19–26.5 mm rubber was used. Additionally, rubber inclusion significantly reduced ballast breakage, with a maximum 45% reduction in the Ballast Breakage Index (BBI) achieved using 15% of the larger rubber size (19–26.5 mm).

References

Arachchige, C.M., Indraratna, B., Qi, Y., Vinod, J.S. and Rujikiatkamjorn, C. (2022) 'Deformation and degradation behavior of rubber intermixed ballast system under cyclic loading', *Engineering Geology*, 307, p. 106786.doi: 10.1016/j.enggeo.2022.106786

Indraratna, B., Qi, Y., Jayasuriya, C., Rujikiatkamjorn, C. and Arachchige, C.M. (2021) 'Use of recycled rubber inclusions with granular waste for enhanced track performance', *Transportation Engineering*, 6, p. 100093. doi: 10.1016/j.treng.2021.100093

Sol-Sánchez, M., Thom, N.H., Moreno-Navarro, F., Rubio-Gámez, M.C. and Airey, G.D. (2015) 'A study into the use of crumb rubber in railway ballast', *Construction and Building Materials*, 75, pp. 19-24. doi: 10.1016/j.conbuildmat.2014.10.045

PREDICTING TRAFFIC DELAYS CAUSED BY LANE-CHANGING BEHAVIOR ON MULTILANE HIGHWAYS

Ekanayake N.[1,*], Eriyagolla R.[1], Wijesundara H.[1], Wickramasinghe V.[1]

[1]Department of Civil Engineering, Faculty of Engineering, University of Peradeniya, Sri Lanka

* e19097@eng.pdn.ac.lk

Abstract

This study examines the impact of lane change manoeuvres on the time delay experienced by target lane following vehicles (TLFVs) in mixed traffic using machine learning. Based on the HighD dataset, which includes naturalistic trajectory data from German highways, over 3500 valid interactions involving both cars and trucks were extracted. Key features such as vehicle types, velocities, steering angle, minimum gap, traffic density, and lane change duration were considered. Time delay was computed by comparing predicted and actual TLFV trajectories during each manoeuvre. Two ensemble models, Random Forest and XGBoost were developed and compared with a baseline Linear regression model. XGBoost yielded the highest performance, with Minimum gap and LC duration identified as the most influential features. Truck-involved Lane changes led to consistently higher delays, with average time delay increasing by 14–21% in mixed vehicle scenarios compared to car–car interactions. The findings offer practical value for traffic management and autonomous vehicle systems, especially in the context of developing countries with heterogeneous traffic.

Keywords: Lane-changing, Machine learning, HighD dataset, Predictive modelling

1. Introduction

Lane-changing behaviour is a critical component of traffic flow dynamics, often causing disruptions that impact safety, efficiency, and overall road capacity. Numerous studies have examined the implications of lane changes, with research by indicating that such manoeuvres account for around 17% of severe traffic accidents (Shawky, 2020). Nagatani & Yonekura (2014) further highlighted the potential for rear-end and side collisions during lane changes, emphasizing their role in initiating crash chains. While existing literature have explored the influence of lane-changing on traffic flow and safety, most studies have focused on general effects or congested conditions. However, under free and moderate flow conditions, the specific time delay imposed on TLFVs remains underexplored. This research addresses this gap by quantifying the delay experienced by TLFVs during adjacent lane changes under free and moderately congested (<20 veh/km) highway conditions. In contrast to earlier studies, this work also adopts machine learning methods to predict complex non-linear interactions, offering new insights into delay mechanisms and enabling improved real-time traffic management strategies.

2. Literature review

2.1 Introduction

Lane changing, classified as mandatory or discretionary (Samal et al., 2024), significantly affects traffic flow, often creating shockwaves and congestion (Wang et al., 2019) While moderate lane-changing can improve flow, excessive or aggressive manoeuvres reduce capacity, increase delays, and raise crash risks, accounting for about 5% of crashes and 7% of related fatalities (Susilawati et al., 2018).These disruptions impact queue length, travel time, and road safety, emphasising the need for better traffic management strategies.

2.2 Factors influencing Lane Changing behavior

Lane-changing is shaped by traffic density, driver behaviour, vehicle characteristics, and road conditions. High-density traffic leads to more aggressive changes (Yang et al., 2021). Aggressive drivers tend to change lanes abruptly, while cautious ones maintain following positions (Ali Abdi et al., 2012; Sun & Kondyli, 2010). Larger vehicles require more space (Xie et al., 2022), and decisions are influenced by gap acceptance (Wang et al., 2019). Anticipation behaviour also plays a role, with 44% of following vehicles

slowing down before a nearby lane change (Chen et al., 2022).

2.3 Data analysis Methodologies

Various methods, including trajectory analysis, estimate delays from lane changes. Statistical approaches include parametric, non-parametric, and semi-parametric models (Zhao et al., 2024). Hazard-based and accelerated failure time models capture delay durations. Kaplan–Meier and Nelson–Aalen offer distribution-free estimates but low interpretability. Cox models balance complexity and clarity, while RSF models offer accuracy but are harder to implement. The absence of a standard model stems from variations in traffic conditions, data quality, model assumptions, and evaluation metrics, limiting generalizability across different settings.

2.4 Review of relevant studies

(Yang et al., 2021) reported delays of 3.9–9.5 seconds per lane change. (Sun & Kondyli, 2010) showed how lane changes disrupt surrounding vehicles in dense traffic. (Ali et al., 2020) found Extra Trees to be the most effective ML model for predicting lane changes. (Li et al., 2020) showed that designated lane-changing zones improve flow. (Xie et al., 2022) highlighted autonomous vehicles reduce unnecessary lane changes, smoothing traffic.(Zhao et al., 2024) found that speed, density, and gap size significantly affect lane-changing duration.

2.5 Gaps and research contribution

Several key research gaps remain in the current understanding of lane-changing-induced delays. One major challenge is isolating delays specifically caused by lane changes from those due to general traffic congestion (Hou et al., 2024). Most studies also overlook the role of surrounding traffic conditions—such as the positions and movements of adjacent vehicles—despite their importance in influencing lane-change decisions (Zhao et al., 2024). Furthermore, existing research has primarily focused on congested conditions, with limited attention given to how lane changes affect traffic in free-flow or moderate-density environments. These gaps suggest a need for more refined models that incorporate local traffic interactions and conditions. Addressing these limitations could enhance predictive accuracy and support the development of more effective traffic management strategies.

3. Methodology

3.1 Dataset source and Preprocessing

The HighD dataset (Krajewski et al., 2018) is a high-resolution naturalistic vehicle trajectory dataset recorded on six structurally similar rural highway sections near Cologne, Germany. Captured using drones over 16.5 hours of daylight traffic, it includes nearly 10,000 documented lane-change events under free to moderately congested conditions. The dataset features both passenger cars and trucks, with clear vehicle type labelling.

Data pre-processing focused on identifying valid lane-change events. Initial detection was based on changes in lane ID, which update when half the vehicle enters a new lane. Trajectories were then analysed to determine the true start (onset of lateral movement) and endpoint (stabilization in the new lane) of each manoeuvre. Events with missing data, incomplete manoeuvres, or exits from the observation area were excluded. Delay outliers were removed using the interquartile range method. This process yielded 3651 high-quality lane change scenarios suitable for delay prediction modelling.

3.2 Delay Estimation

The time delay experienced by the TLFV was estimated by comparing its actual trajectory to a predicted trajectory assuming no lane change occurred. The start of the lane change was defined as the onset of lateral movement by the lane-changing vehicle (LCV), with a 0.5-second lead time included to account for driver reaction. Within this window, the TLFV was assumed to travel at uniform velocity or acceleration, and a linear trend was fitted to its velocity data to forecast its expected motion. The predicted distance the TLFV would have travelled by the end of the lane change was then calculated and compared to the actual distance covered. The difference between these values represented the distance loss due to the lane change. This loss was converted into a time delay by dividing it by the TLFV's average speed before the manoeuvre.

3.3 Model Development

Three machine learning models were developed and compared to predict the delay.

- Linear Regression was used as a baseline model, assuming additive and linear relationships between features and delay, with coefficient analysis used to interpret feature influence.

- Random Forest Regression, an ensemble method based on multiple decision trees, was employed to capture complex interactions and non-linear patterns.
- XGBoost Regression, a gradient boosting algorithm known for its high accuracy and efficiency, was also implemented; it builds trees sequentially.

The dataset was split into training (80%) and testing (20%) sets using stratified sampling to preserve the vehicle type distribution. Features were scaled where appropriate to improve model stability.

4. Results and Discussion

4.1 Model Performance

Three models, Linear Regression, Random Forest Regression, and XGBoost Regression were evaluated using RMSE, MAE, and R^2 metrics. Linear Regression showed the weakest performance with high error rates, indicating its inadequacy in modelling the non-linear relationships in the dataset. Random Forest Regression significantly improved accuracy, capturing complex interactions. XGBoost Regression achieved the best performance, offering highly reliable predictions across vehicle categories.

Table 2: Performance of models

Model	RMSE (s)	MAE (s)	R^2
Linear Regression	2.37	1.37	0.60
Random Forest Regression	1.44	0.72	0.82
XGBoost Regression	1.33	0.59	0.87

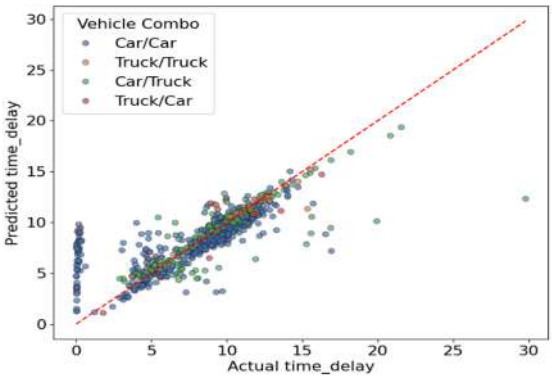

Figure 1: Predicted vs. Actual time delay by the Linear Regression Model

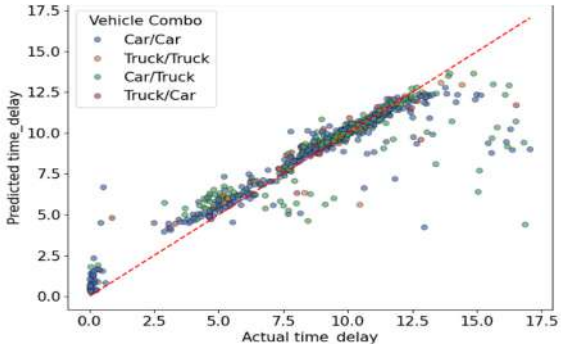

Figure 2: Predicted vs. Actual time delay by the Random Forest Regression Model

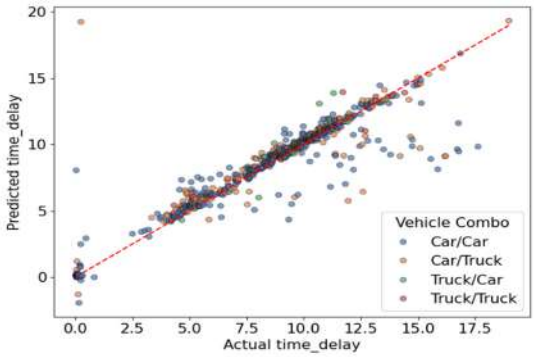

Figure 3: Predicted vs. Actual time delay by the XGBoost Model

Linear Regression showed the poorest performance, with the highest error and lowest R^2, highlighting its inability to capture complex patterns in the data. Scatter plots of predicted vs. actual delays showed in Figure 1 revealed wide dispersion, especially for higher delays and certain vehicle types. Random Forest improved accuracy noticeably, with reduced error and better alignment in predictions. XGBoost performed the best, demonstrating tight clustering in predicted vs. actual plots across all vehicle combinations.

4.2 Discussion

The ensemble models clearly outperformed Linear Regression in capturing the complex non-linear relationships between variables and the delay outcome. XGBoost's boosting framework allowed it to incrementally minimize prediction error, resulting in slightly better performance than Random Forest. Scatter plots by vehicle combination confirmed that ensemble models were more consistent across categories. In addition to model performance, the study identified the average delay experienced for each combination of LCV and TLFV types.

These results show that vehicle type combinations significantly impact TLFV delay

during lane changes. Car/car interactions resulted in the lowest delays, while truck/truck combinations caused the highest average delay. Truck-involved manoeuvres increased delay by 14–21% compared to car/car cases, highlighting the disruptive nature of heavy vehicles.

Table 2: Average time delay of each vehicle type

LCV/ TLFV	Actual avg. delay (s)	Avg. delay predicted by LR (s)	Avg. delay predicted by RFR (s)	Avg. delay predicted by XGB (s)
Car/Car	7.95	7.84	7.86	7.83
Car/Truck	9.25	9.02	9.18	9.23
Truck/Car	9.04	9.16	8.79	8.90
Truck/Truck	9.59	10.22	9.36	9.38

5. Conclusions

This study found that machine learning models—particularly ensemble methods such as Random Forest and XGBoost—achieved high accuracy in predicting delays from lane changes. XGBoost performed best, closely followed by Random Forest, effectively capturing non-linear relationships. Minimum gap and lane-change duration were the most influential features. Delays were lowest for car–car interactions and highest for truck–truck interactions, highlighting the impact of vehicle type, gap size, and manoeuvre duration on traffic delay modelling.

References

Abdi, A., Mobasheri, H. and Alavi, M.P.N. (2012) 'The Evaluation of Lane-Changing Behavior in Urban Traffic Stream with Fuzzy Clustering Method', *Research Journal of Applied Sciences, Engineering and Technology*, 4(22), pp. 4701–4710.

Chen, K., Knoop, V.L., Liu, P., Li, Z. and Wang, Y. (2023) 'Modeling the impact of lane-changing's anticipation on car-following behavior', *Transportation Research Part C Emerging Technologies*, 150.

Hou, K., Zou, J., Zheng, F., Liu, X. and He, Z. (2024) 'On the Precise Quantification of the Impact of a Single Discretionary Lane Change on Surrounding Traffic', *arXiv*, doi: 2407.18557.

Krajewski, R., Bock, J., Kloeker, L. and Eckstein, L. (2018) 'The highD Dataset: A Drone Dataset of Naturalistic Vehicle Trajectories on German Highways for Validation of Highly Automated Driving Systems', *2018 21st International Conference on Intelligent Transportation Systems (ITSC)*, pp. 2118–2125.

Li, H., Huang, Z., Zou, X., Zheng, S. and Yang, Y. (2020) 'VISSIM-Based Simulation and Analysis of Upstream Segments in Ramp Areas for Optimizing Vehicle Group Lane-Changing Behaviors', *Journal of Advanced Transportation*, 2020, pp. 1–11.

Nagatani, T. and Yonekura, S. (2014) 'Multiple-vehicle collision induced by lane changing in traffic flow', *Physica A: Statistical Mechanics and Its Applications*, 404, pp. 171–179.

Samal, S.R., Mohanty, M. and Gorzelańczyk, P. (2024) 'Exploring Lane Changing Dynamics: A Comprehensive Review of Modeling Approaches, Traffic Impacts, and Future Directions in Traffic Engineering Research', *Transactions on Transport Sciences*, 15(2), pp. 54–68.

Shawky, M. (2020) 'Factors affecting lane change crashes', *IATSS Research*, 44(2), pp. 155–161.

Sun, D.J. and Kondyli, A. (2010) 'Modeling Vehicle Interactions during Lane-Changing Behavior on Arterial Streets', *Computer-Aided Civil and Infrastructure Engineering*, 25(8), pp. 557–571.

Susilawati, S., Tan, K.Y., Samad, K.M.A. and Ng, C. (2018) 'The Study of Location Specific Lane Change Impacts on Traffic Delay using Extended Cell Transmission Model', *MATEC Web of Conferences*, 203.

Wang, X., Yang, M. and Hurwitz, D. (2019) 'Analysis of cut-in behavior based on naturalistic driving data', *Accident Analysis and Prevention*, 124, pp. 127–137.

Xie, H., Ren, Q. and Lei, Z. (2022) 'Influence of Lane-Changing Behavior on Traffic Flow Velocity in Mixed Traffic Environment', *Journal of Advanced Transportation*, 2022.

Yang, Q., Lu, F., Ma, J., Niu, X. and Wang, J. (2021) 'Analyzing the delays of target lane vehicles caused by vehicle lane-changing operation', *Scientific Reports*, 11(1).

Zhao, S., Huang, S., Wen, H. and Liu, W. (2024) 'Analysis of Highway Vehicle Lane Change Duration Based on Survival Model', *Big Data and Cognitive Computing*, 8(9), 114

RECURSIVE LOGIT MODELLING APPROACH FOR EVACUATION ROUTE CHOICE IN DISASTROUS NETWORKS

Goonasekara S.W.[1,*], Basnayaka B.M.P.S.[1], Thalgaskotuwa D.H.M.K.S.[2] and Dharmarathna W.R.S.S.[1]

[1]Department of Civil Engineering, University of Peradeniya

[2]Department of Civil Engineering, University of Tokyo

* e19122@eng.pdn.ac.lk

Abstract

Flood evacuation planning in densely populated areas requires a proper understanding on how people make decisions under emergency conditions, as poor evacuation decisions can lead to significant casualties and economic losses. Traditional evacuation models often fail to capture the dynamic nature of human decision-making during emergencies, particularly in flood-prone regions where conditions change rapidly. This research addresses the critical need for improved evacuation route choice modelling by examining how evacuees make sequential decisions during flood events in Ratnapura district, Sri Lanka. Recursive Logit (RL) Modelling Approach was used and it provides a robust framework for analysing evacuation route choices during flood events by capturing the sequential decision-making process of evacuees. This study applies the β-Scaled RL model to evaluate dynamic route choice, incorporating factors such as distance to the evacuation centre, elevation, early evacuation, and late evacuation. The estimated value of β (sequential time discount rate) was 0.46 and it significantly indicated the lack of knowledge on proper evacuation routes where myopic decisions were dominated. The framework enables data-driven decision support systems that can enhance community resilience and reduce evacuation times during flood emergencies.

Keywords: Recursive Logit, evacuation, decision-making dynamics, disastrous network

1. Introduction

In recent years, the increasing frequency and intensity of flood events have underscored the critical need for effective evacuation planning in disaster-prone regions. This study focuses on the development of a β-Scaled Recursive Logit (β - SRL) modelling approach to analyse and predict the evacuation route choices of individuals during floods. Specifically, the research aims to identify key factors influencing route selection behaviour, capture the sequential decision-making patterns of evacuees using the RL model, and propose optimized evacuation strategies that minimize both time and risk. The study area includes major flood-prone zones within the Rathnapura district. Detailed data analysis and parameter estimation were carried out in the RStudio platform.

2. Literature review

Fosgerau et. al., (2013) proposed a link-based network route choice model that eliminates the need to predefine a restricted choice set. This innovation allows for greater modeling flexibility and better reflects real-world conditions where travelers may consider numerous routes. The model uses a Recursive Logit (RL) framework, which captures the sequential nature of decision-making across network links rather than entire paths. This structure makes it computationally efficient and scalable to large networks, as it avoids the need to enumerate all possible routes while still maintaining behavioral realism.

Oyama and Hato (2016) developed a dynamic network route choice model based on the above RL approach which tailored to disaster evacuation scenarios, incorporating evacuees' risk perception. They accounted for how individuals make route decisions in a step-by-step manner, adapting as new information becomes available during an evacuation. Their findings highlight that perceived risk plays a crucial role in determining evacuation behavior, and the model effectively simulates adaptive responses in real-time, making it useful for emergency planning and policy development.

Dharmarathna and Hato (2018) examined the impact of sequential time discount rate (β) in varying disaster scenarios through β-SRL modeling approach. Their research revealed how time urgency and network-specific characteristics influence evacuees' decision-making during emergencies. By analyzing behavior across different network conditions, the study emphasized the importance of incorporating dynamic time sensitivity into evacuation models. These insights contribute to the design of more responsive and efficient evacuation strategies, especially in disaster-prone areas.

3. Methodology

The study employed a structured methodology consisting of three primary phases: data collection, cross-sectional analysis, and parameter estimation. Data were gathered from major flood-prone areas of Ratnapura, capturing evacuees' behaviour over a 4-hour period prior to a flood. This period starts from the moment that an evacuee receives the early warning. 4-hour period was segmented into 16 decision-making intervals (D1 to D16), each representing 15-minute time steps. This breakdown enabled the modelling of sequential decisions made by individuals during process of evacuation. The analysis incorporated five dynamic parameters: distance to the evacuation centre, elevation above mean sea level, early evacuation behaviour (between 1.0 to 2.5 hours), late evacuation behaviour (between 2.5 to 4.0 hours), and the sequential time discount rate (β). Cross-sectional analysis was conducted to evaluate how these variables influenced decision-making at each time interval, and parameter estimation was performed using the β-SRL model in RStudio platform.

Table 3: Decision-making steps with time

h/m	15	30	45	60
1	D1	D2	D3	D4
2	D5	D6	D7	D8
3	D9	D10	D11	D12
4	D13	D14	D15	D16

Activities in each time-step was recorded during the field surveys. In addition, their moving map was generated by using the Global Position System (GPS) data. These maps were checked with the manually drawn maps relevant to the location of each time step. One of the key findings revealed during the discussion was that these evacuees do not evacuate as soon as they received the early warning but use about an hour for preparations. This was confirmed later during the cross-sectional analysis of data.

3.1 Cross Sectional Analysis

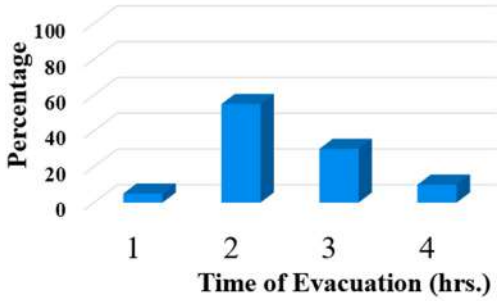

Figure 1: Time of evacuation

Figure clearly shows that first hour evacuees are very low as about 5%. This highlights the victims' understanding about the rate of water level rising which they confirmed through the local identified places during the past floods.

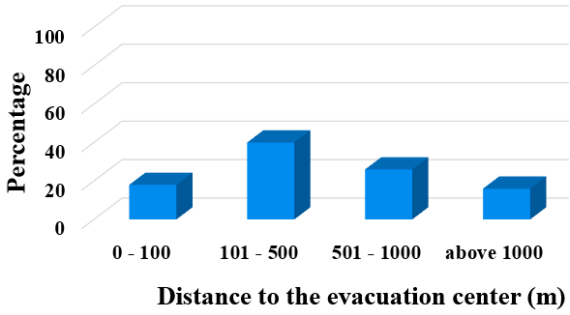

Figure 2: Distance to the evacuation center

Distance varied from neighboring places to above 1 km in distance. However, 84% of them were in less than 1 km distance.

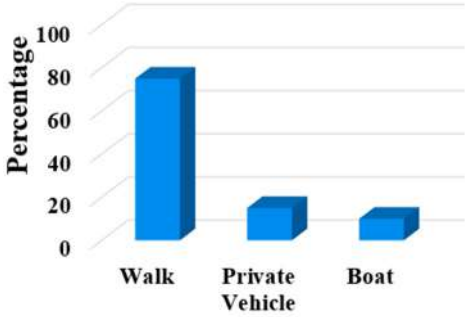

Figure 3: Mode of evacuation

Walking was the dominating mode for evacuation while local boats have been used to cross the flooded sections.

3.2 Theoretical Framework

It is assumed that, an evacuee chooses a link a_{j+1} from the set of outgoing links $A(a_j)$ which maximizes the sum of instantaneous utility $u(a_{j+1}|a_j)$ associated with each link pair and expected downstream utility to the destination link d; $V^d(a_{t+1})$ that is given as a value function which is formulated via Bellman equation as shown in equation 1.

$$V^d(a_j) = \mathrm{E}\left[\max_{a_{j+1}\in A(a_j)}\{v(a_{j+1}|a_j;\theta) + V^d(a_{j+1}) + \mu\varepsilon(a_{j+1})\}\right] \quad \forall a_j \in A \qquad (1)$$

where, $v(a_{j+1}|a_j;\theta) = v(x_{a_{t+1}|a_t};\theta)$ is the deterministic utility component, $x_{a_{t+1}|a_t}$ is a vector of observed characteristics of the link pair (a_j, a_{j+1}) and θ is an unknown parameter vector to be estimated. The random term ε is assumed to be an independent and identically distributed (i.i.d.) extreme value type I with scale parameter μ, the dummy link for the destination d has no successor.

The probability of choosing a link a_{j+1} given state a_j is given by the multinomial logit model and is shown in equation 2.

$$p(a_{j+1}|a_j) = \frac{e^{\frac{1}{\mu}\{v(a_{j+1}|a_j)+V(a_{j+1})\}}}{\sum_{a'_{j+1}\in A(a_j)} e^{\frac{1}{\mu}\{v(a'_{j+1}|a_j)+V(a'_{j+1})\}}} \qquad (2)$$

As indicated in the literature review, the concept of sequential time discount rate (β) was introduced as a generalization of drivers' decision-making dynamics and a representation of the degree of spatial cognition of networks, as a parameter in RL model. Accordingly, the equation 1 was re-formulated as shown in equation 3.

$$V^d(a_j) = E[_{a_{j+1}\in A(a_j)}\max\{v(a_{j+1}|a_j;\theta) + \beta V^d(a_{j+1}) + \mu\varepsilon(a_{j+1})\}] \ \forall a_j \in A \qquad (3)$$

β is the sequential time discount rate of the value function and it is assumed to be vary between zero and one. The transition probability from link a_j to a_{j+1} is given from the multinomial logit model and is shown in equation 4.

$$p(a_{j+1}|a_j) = \frac{e^{\frac{1}{\mu}\{v(a_{j+1}|a_j)+\beta v(a_{j+1})\}}}{\sum_{a'_{j+1}\in A(a_j)} e^{\frac{1}{\mu}\{v(a'_{j+1}|a_j)+\beta v(a'_{j+1})\}}} \qquad (4)$$

As identified earlier, first hour was excluded from the parameter estimation as there were no significant decisions related to the dynamic evacuation. Initial moving, reaching an intermediate station, leaving the intermediate station and reaching the evacuation centre were considered as the key decisions.

4. Results and Discussion

4.1. Parameter Results

Table 2: Parameter estimates and t-value

Parameter	Estimate	t-Value
Distance to Evacuation Centre	-6.77	-3.04
Elevation (MSL)	0.34	0.11
Early evacuation (1.0 - 2.5 hours)	0.45	3.65
Late evacuation (2.5 - 4.0 hours)	0.51	4.77
Sequential time discount rate (β)	0.46	2.28
Rho Squared	0.41	
Adjusted Rho-Squared	0.39	
Sample size	447	

Distance to the evacuation center has significantly affected the route choice, with people less likely to choose distant locations. Late evacuation is more preferred than the early evacuation as it was not a flash flood. β was 0.46 which indicates the dominance of myopic decisions.

4.2 Public Opinion

Public opinions were collected on participating in the flood evacuation preparedness programs and flood drills. Accordingly, it was revealed that 67.8% are interest for flood evacuation preparedness programs.

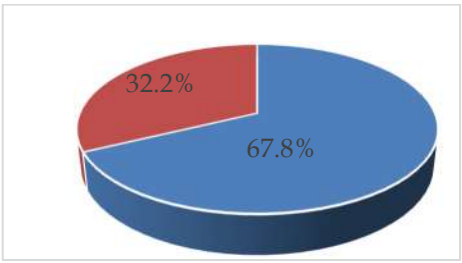

Figure 4: Interest for flood evacuation preparedness programs

- Interested for flood preparedness programs
- Not interested for flood preparedness programs

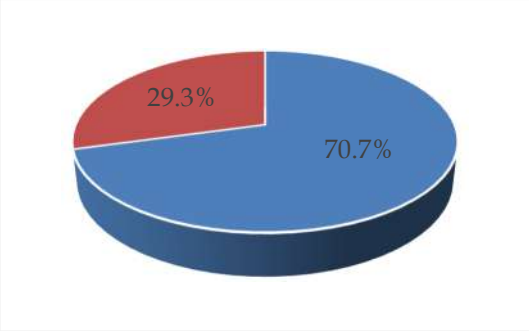

Figure 5: Interest for flood drills

- Interested for flood drills
- Not interested for flood drills

70.7 % of the public are interest for participating in flood drills. These strong public support for improved flood preparedness programs and flood drills should be utilized and conducting such programs in regular basis would improve the β to a higher value than the current 0.46.

5. Conclusions

The findings of the study highlight that distance to the evacuation centre played a significant role in influencing evacuees' route choices, whereas elevation was not a significant factor. The analysis revealed a general preference for late evacuation (2.5 – 4.0 hours) over the early evacuation. The estimated sequential time discount rate *(β)* value of 0.46 suggests a dominance of myopic decision-making, where immediate choices outweigh long-term considerations. These behavioural patterns show the need for stronger flood preparedness strategies. Public support for such initiatives is evident and should be effectively leveraged through prioritized evacuation planning, flood risk map displays, regular drills, and clear procedural guidelines, all of which have the potential to enhance forward-looking decision-making and improve β in future evacuations.

References

Bellman, R.E. (1957) 'Dynamic programming'. Princeton: Princeton University Press.

Dharmarathna, W.R.S.S. and Hato, E. (2018) 'Comparison of sequential time discount rate in differential disastrous networks', *Proceedings of Transportation Research Board 97th Annual Meeting*, 7–11 January, Washington D.C., USA.

Fosgerau, M., Frejinger, E. and Karlstrom, A. (2013) 'A link-based network route choice model with unrestricted choice set', *Transportation Research Part B: Methodological*, 56, pp. 70–80.

Mert, A., Kiziltan, G. and Balakrishna, R. (2022) 'Integrating behavioral consistency in recursive logit route choice models for dynamic networks', *Transportation Research Part C: Emerging Technologies*, 141, p. 103756. doi: 10.1016/j.trc.2022.103756

Oyama, Y. and Hato, E. (2016) 'A dynamic network model based on a recursive logit model considering risk perception in disaster evacuation behavior', *Journal of the Eastern Asia Society for Transportation Studies*, 11, pp. 1394–1409.

Xu, R., Gao, S., Lu, J. and Zhao, J. (2018) 'Dynamic network user equilibrium with recursive logit-based route choice model', *Transportation Research Part B: Methodological*, 111, pp. 132–147. doi: 10.1016/j.trb.2018.03.005

MODE CHOICE AND MODE SHIFT OF COMMUTERS FOR ALTERNATIVE BUS ROUTE SYSYTEMS IN KANDY DISTRICT

Dassanayake D.M.S. I[1,*], Ponnamperuma T.D.R.[1], Herath P.M.G.D.M.[1] and Dharmarathna W.R.S.S.[1]

[1] Department of Civil Engineering, Faculty of Engineering, University of Peradeniya, Sri Lanka

* sandunidassanayake8@gmail.com

Abstract

Urban congestion and inefficient public transport have become critical challenges in Kandy district, where daily commuters frequently face delays, overcrowding, and unreliable travel services. This study investigates commuter mode choice behavior and the potential for mode shift toward direct, non-transit alternative bus routes. Data were collected through structured surveys and field observations across the district. Multinomial Logit (MNL) modeling approach was applied to analyze mode choice behavior. The results revealed a strong preference for private modes, such as motorcycles, cars, and three-wheelers, primarily due to convenience and reduced travel time. Public buses were less preferred, especially where service quality was lacking. Travel time emerged as the most influential factor, while cost had a lesser effect. Elasticity analysis showed that even a slight increase in travel time significantly reduced bus attractiveness. Cross elasticity confirmed that inconvenience in one mode drives commuters toward alternatives. Importantly, both public and private users expressed willingness to shift to direct public transport if improvements are made in speed, comfort, and affordability. The study highlights the urgent need for direct, efficient, and commuter-oriented public bus routes to improve travel conditions and reduce urban congestion in Kandy district.

Keywords: Travel Behavior, MNL Modeling, Public Transport, Stated Preference, Elasticity

1. Introduction

Public transport in the Kandy district, primarily public buses continue to face challenges such as inefficiency, overcrowding, and frequent delays, prompting many commuters to depend on private modes of travel. As urban areas expand and private vehicle ownership increases, traffic congestion has become a growing concern across both urban and rural parts of the district. This study aims to understand how commuters in Kandy district make transport decisions and examines the potential for encouraging a shift toward improved public transport services. It focuses on identifying current travel patterns and the key factors influencing mode choice, including travel time and travel cost. The research also evaluates commuter willingness to shift to direct, non-transit alternative bus routes under improved service conditions. The findings are expected to support the development of a more efficient, reliable, and user-friendly public transport system tailored to the needs of the Kandy district.

2. Literature Review

Herath et al. (2023) studied short-distance commuters in Kandy district using factor analysis, Multinomial Logit (MNL) modeling, and elasticity analysis. They found that age, occupation, distance, and travel cost significantly influence mode choice. Elasticity results showed that even slight reductions in bus travel time could increase public transport use, highlighting the need for travel-time-sensitive and demand-driven planning to promote sustainable urban mobility in the region.

Ashalatha et al. (2013) analyzed commuter mode choice in Thiruvananthapuram using MNL modeling. The study showed that rising age and income led commuters to prefer private transport, while travel time and cost per distance were also significant influencers. The findings stressed the importance of understanding behavioral and socio-economic factors for designing user-focused and effective transport systems in developing urban areas.

Naqvi et al. (2022) explored commuter mode shift toward the Islamabad Metro Bus Service using logistic regression analysis. They found that commuters were more likely to switch from private and traditional public modes to metro services for job, education, and shopping

purposes. Travel time, cost, and trip distance were key factors, while income was not significant. Female commuters showed a greater likelihood to shift compared to male counterparts.

3. Methodology

3.1 Data collection

Primary data were collected through a structured survey conducted among 461 commuters in the Kandy district. The survey gathered data on socio-demographic attributes, trip characteristics, current travel mode, and willingness to shift to direct public transport.

3.2 Parameter estimation for mode choice

A Multinomial Logit (MNL) model was used to estimate the probability of selecting a particular mode from six alternatives: Taxi, Bus, Car, Motorbike, Train, and Three-Wheeler. The utility function for each mode was formulated as:

$$U = \beta_0 + \beta_1 X_1 + \cdots . \beta_n X_n + \varepsilon \quad (1)$$

Where is U the utility X_1, X_2, ..., X_n are attributes and β_0, β_1, β_2, ..., β_n are parameters, and ε represents the random error term. Model parameters were estimated via Maximum Likelihood Estimation (MLE), optimizing the log-likelihood function. This optimization was performed using the Nelder–Mead algorithm.

$$LL(\beta) = \prod_{n=1}^{N} \prod_{i} . y_{ni} \ln (P_{ni}) \quad (2)$$

The MNL model follows the general form:

$$p(k) = \frac{e^{U_k}}{\sum_x e^{U_x}} \quad (3)$$

Where $p(k)$ is the probability of choosing alternative k and U_k is the utility of alternative k. RStudio platform were used to estimate the above parameters.

3.3 Parameter estimation for mode shift

Direct and cross elasticities were calculated to quantify commuter sensitivity to changes in travel time and cost. These elasticities were derived from the estimated utility parameters and choice probabilities as follows:

Direct elasticity:

$$Eik = \beta k \, Xik \, (1 - Pi) \quad (4)$$

Cross elasticity:

$$Eik = -\beta k \, Xik \, Pi \quad (5)$$

In these equations, β_k is the coefficient of the attribute, X_{ik} represents the attribute value, and P_i is the probability of choosing mode i.

Stated preference responses were also analyzed to evaluate the potential modal shift to a proposed direct public transport service.

4. Results and Discussion

4.1 Major origins and destinations

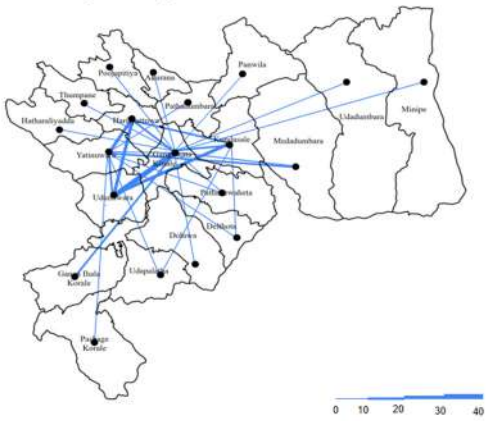

Figure 1: Trip Distribution Network

Major origin–destination (O–D) connections across the Kandy district were mapped using survey data. The thickness of each line on the map represents the volume of commuters traveling along that route. Notably, several high-demand O–D pairs do not pass through Kandy city center. However, the current public bus network frequently forces such trips through the city core, resulting in unnecessary delays and increased congestion. This highlights the need for direct route planning to improve travel efficiency and reduce central traffic loads.

4.2 Cross Sectional Analysis

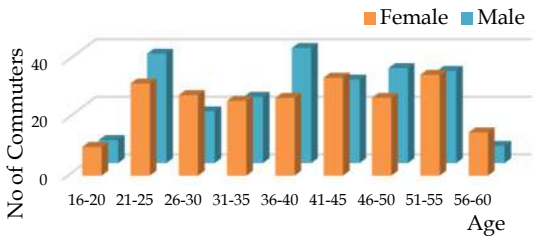

Figure 2: Age Distribution by Gender

A total of 461 survey responses were analyzed to assess commuter behavior in Kandy district. The sample ensured diversity in age, gender, occupation, and travel purpose. Figures 2 and 3 show wide age representation and that most commuters travel for work or education. Figure

4 indicates that, out of 461 commuters, 241 currently use private transport and 220 use public transport, reflecting a slight preference for private modes.

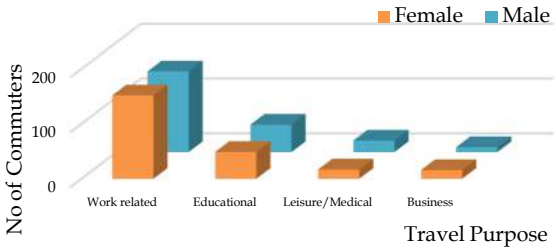

Figure 3: Travel Purposes by Gender

Commuters were asked if they would shift to a direct public transport service connecting their origins and destinations without transits. Stated preference analysis showed strong support, with 96% of public (Figure 5) and 71% of private (Figure 6) users willing to shift, indicating high potential for modal shift.

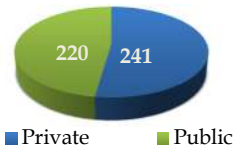

Figure 4: Current Travel Mode Usage

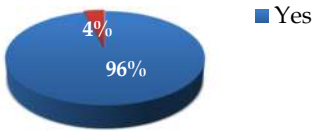

Figure 5: Willingness of Public Users to Shift

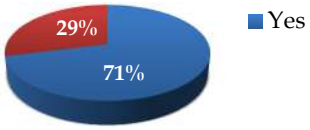

Figure 6: Willingness of Private Users to Shift

Factors influencing willingness to shift (Figures 7 and 8) varied by mode, public users prioritized travel time, cost, and convenience, while private users emphasized cost, followed by time and convenience. Overall, travel time and cost are key drivers of mode shift and improving them supports sustainable transport.

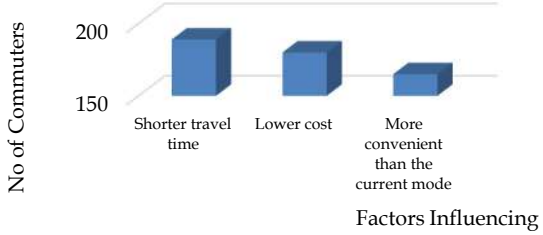

Figure 7: Key Factors Influencing Mode Shift Among Public Transport Users

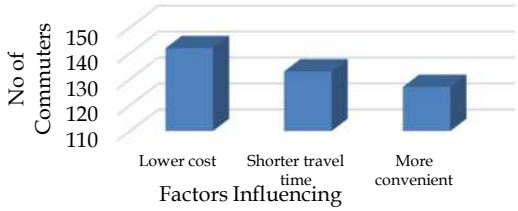

Figure 8: Key Factors Influencing Mode Shift Among Private Transport Users

4.3 Parameter estimation for mode choice

A Multinomial Logit (MNL) model was developed to evaluate commuter mode choice among six alternatives: Taxi, Bus, Car, Motorbike, Train, and Three-Wheeler. The model incorporated travel time and travel cost as continuous explanatory variables and included alternative-specific constants to capture mode-specific preferences.

Table 1: Estimated coefficients

Parameter	Estimate	t-value
ASC_Taxi	-2.818	-6.65
ASC_Car	1.034	2.87
ASC_Motorbike	1.036	3.36
ASC_Train	-1.07	-3.33
ASC_Three-Wheeler	0.826	2.59
Total Travel Time	-0.214	-4.27
Total Travel Cost	-0.001	-1.36
Sample size	461	
Rho-square	0.447	
Adjusted rho-square	0.437	

The Bus mode was normalized and treated as the reference category. Maximum Likelihood Estimation yielded a final log-likelihood of −380.079 and a null log-likelihood of −687.1023. The model demonstrated strong explanatory power, with a McFadden's Rho-square (ρ^2) of 0.447 and an adjusted ρ^2 of 0.437.

The estimated coefficients (Table 1) confirmed that travel time was the most influential factor in mode selection, significantly reducing utility as it increased. Travel cost, although negatively related to utility, had a weaker statistical impact. Most parameters, especially travel time and alternative-specific constants, were statistically significant at the 95% confidence level.

Among the alternatives, motorbike and car emerged as the most preferred modes, with motorbike slightly ahead. Three-wheeler was the third choice, while train and taxi were less preferred than the base mode (bus). The findings emphasize the need for substantial improvements in public transport services to compete effectively with private travel options.

4.4 Parameter estimation for mode shift

Elasticity analysis was conducted using the coefficients derived from the MNL model to evaluate commuter sensitivity to changes in travel time and cost.

Table 2: Estimated direct elasticity values

Mode	Travel Time (%)	Travel Cost (%)
Bus	-3.65	-0.02
Taxi	-1.48	-0.07
Car	-1.39	-0.06
Motorbike	-1.45	-0.05
Train	-17.84	-0.04
Three-wheeler	-2.19	-0.06

The results confirm that all direct elasticity values are negative, indicating that increases in travel time or cost reduce the likelihood of selecting the same mode. Specifically, a one-minute increase in bus travel time reduces bus ridership by 3.65%, while a one LKR increase in bus fare leads to a 0.02% reduction in bus users. This highlights the high time sensitivity of commuters compared to cost.

Table 3: Estimated cross elasticity values

Mode	Travel Time (%)	Travel Cost (%)
Bus	7.72	0.043
Taxi	6.83	0.32
Car	6.99	0.32
Motorbike	6.72	0.23
Train	0.03	0.0001
Three-wheeler	5.20	0.18

Conversely, all cross-elasticity values are positive, confirming that a decrease in utility for one mode increases the probability of choosing an alternative. A one-minute increase in bus travel time shifts 7.71% of commuters to other modes, while a one LKR increase in bus cost results in a 0.04% shift. These results emphasize that commuters are significantly more responsive to travel time than cost, and even marginal increases in time can lead to notable shifts in mode choice. The findings validate the importance of minimizing travel time in public transport services to retain users and attract commuters from private modes.

5. Conclusions

This study aimed to analyze commuter travel behavior and mode shift dynamics in the Kandy district to support the development of more efficient alternative bus route systems. Using spatial trip mapping, MNL based mode choice modelling, and elasticity analysis, the study quantified the influence of travel time and cost on transport decisions.

Private modes, particularly motorbikes and cars were found to be most preferred, compared to busses, and trains and taxis were least attractive. Elasticity analysis revealed that even small increases in travel time or cost can lead to noticeable reductions in ridership and encourage shifts to other modes. For example, a one-minute increase in bus travel time reduces ridership by 3.65%, while a one LKR increase in cost leads to a 0.02% decline.

These findings highlight the need to introduce direct, high-demand bus routes that bypass Kandy city to reduce travel time, alleviate congestion, and enhance the sustainability and efficiency of public transport.

References

Ashalatha, R., Manju, V.S. and Zacharia, A.B. (2013) 'Mode choice behavior of commuters in Thiruvananthapuram city', *Journal of Transportation Engineering*, 139(5).

Herath, P.M.G.D.M., Dharmarathna, W.R.S.S., Wickramasinghe, W.M.V.S.K. and Edirisinghe, A.G.H.J. (2023) 'Travel behavior analysis and exploration of mode choice variability of short-distance travelers', *Engineer: Journal of the Institution of Engineers, Sri Lanka*, 56(1).

Naqvi, R.A., Irfan, M., Farwa, S., Wong, W. and Ahmad, H. (2022) 'Mode Shift Behavior of Commuters Toward Islamabad Metro Bus Service', *Advances in Decision Sciences*, 26(3).

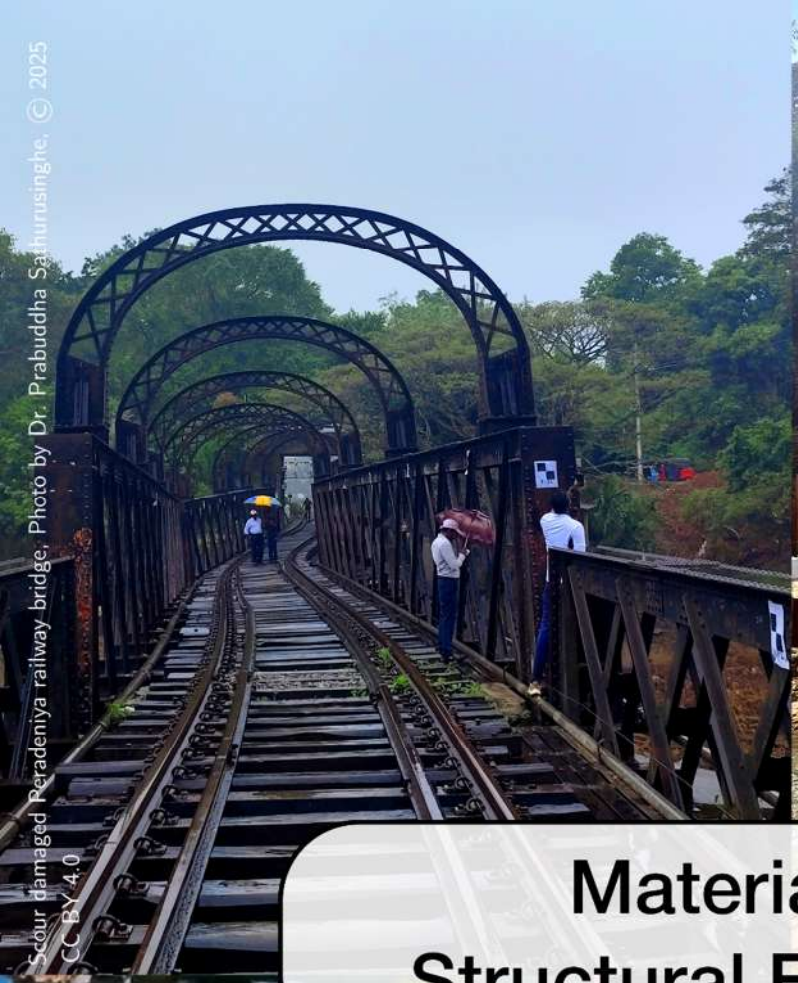

Scour damaged Peradeniya railway bridge, Photo by Dr. Prabuddha Sathurusinghe, © 2025 CC BY 4.0

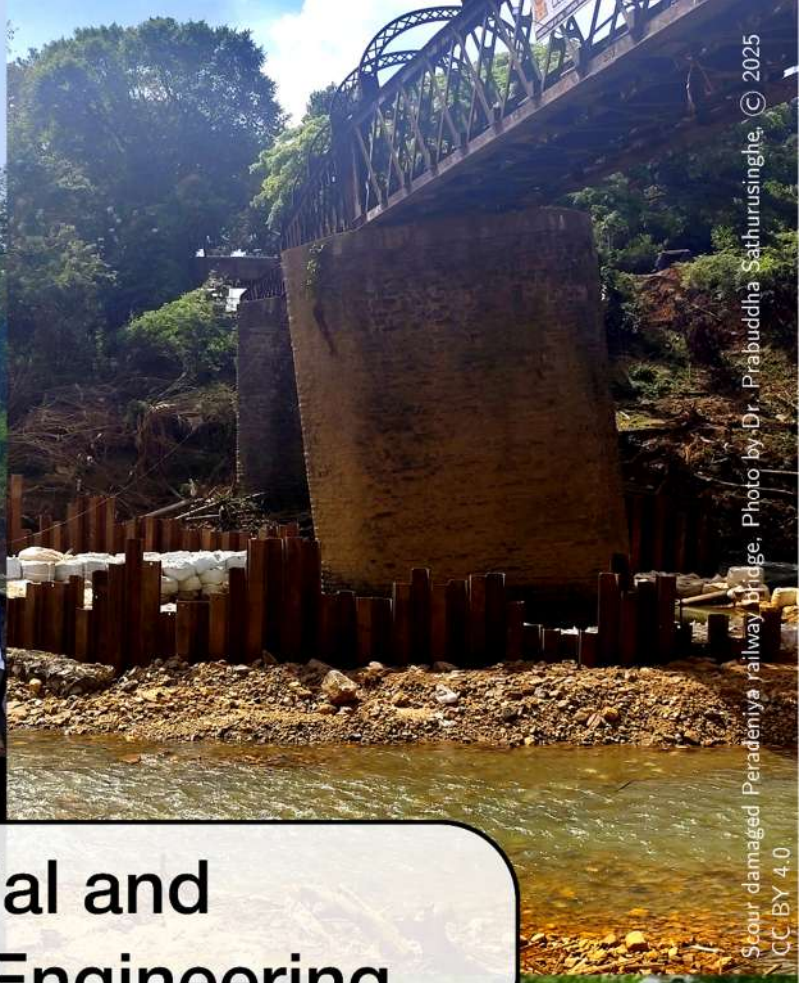

Scour damaged Peradeniya railway bridge, Photo by Dr. Prabuddha Sathurusinghe, © 2025 CC BY 4.0

Material and Structural Engineering

Eco-sustainable 3D printed house "Tecla", still from video by Alfredo Milano and Italdron, CC BY 2.5

PERFORMACE BASED DESIGN OF HIGH-RISE BUILDINGS FOR WIND LOADING

Wijayarathne, R.M.T.D.[1,*], Jayarathna, K.M.S.M.[1], and Wijesundara, K.K.[1]

[1] Department of Civil Engineering, University of Peradeniya, 20404, Sri Lanka

[*] e19442@eng.pdn.ac.lk

Abstract

High-rise buildings experience significant dynamic responses under wind loads, requiring accurate prediction of accelerations, displacements, and drifts for performance-based design. This study presents a validated numerical framework combining linear and nonlinear finite element methods, benchmarked against CAARC wind tunnel data. The workflow includes structural modelling, synthetic wind time-history generation, buffeting load application, and both LTHA and NLTHA. Validation showed strong agreement with experimental results. Parametric studies demonstrated sensitivity to wind speed and damping, with nonlinear analysis predicting slightly higher accelerations due to stiffness degradation. The proposed approach improves response prediction and supports more reliable high-rise wind design.

Keywords: Wind load time histories, CAARC building, Performance-based design, Nonlinear analysis, High-rise buildings

1. Introduction

Modern tall buildings are highly sensitive to wind-induced accelerations affecting occupant comfort. Traditional static or linear methods often overlook these effects. This study develops a validated performance-based wind design (PBWD) framework using the CAARC building, combining synthetic wind load generation and dynamic finite element modelling, supported by wind tunnel data, to assess wind effects under serviceability and ultimate conditions.

2. Literature review

Wind design of high-rise buildings has traditionally relied on simplified code-based methods, which often overlook complex wind-structure interactions. Alternatives like wind tunnel testing and CFD offer improved accuracy but are resource-intensive (Jeong et al., 2021). Performance-Based Wind Design (PBWD) addresses these limitations by evaluating structural performance under varying hazard levels. Early PBWD frameworks (Ciampoli et al., 2011) were extended to include comfort and collapse criteria (Caracoglia and Jones, 2009)). While most studies focus on elastic behaviour, recent research has introduced nonlinear analysis to capture inelastic effects (Bezabeh et al., 2019).

3. Methodology

Figure 1 shows the general steps of the methodology of this study.

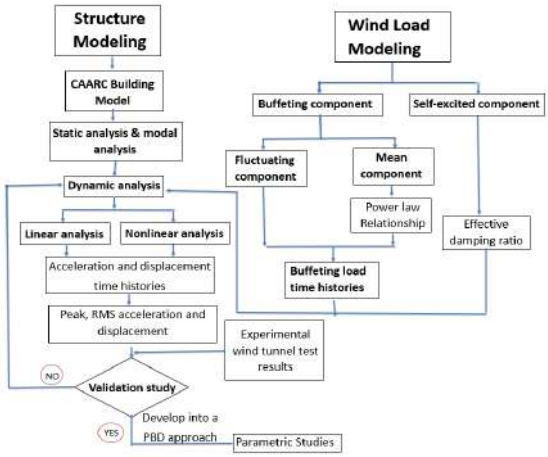

Figure 1: Flowchart of the methodology

3.1 Elastic structure modelling

The CAARC standard building was modeled in ETABS with a 45.72 m × 30.48 m plan and 182.9 m height over 59 stories using its defined geometry and dynamic properties. Figure 2 shows the plan and 3D views of the structure.

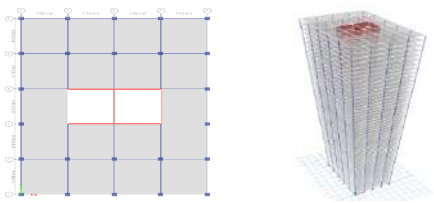

Figure 2: Elastic mode

3.2 Wind load modelling

Turbulent wind load histories were generated using the Deodatis (1996) method with Kaimal spectra and applied at each story level to simulate wind-induced response. The process is illustrated in Figure 3.

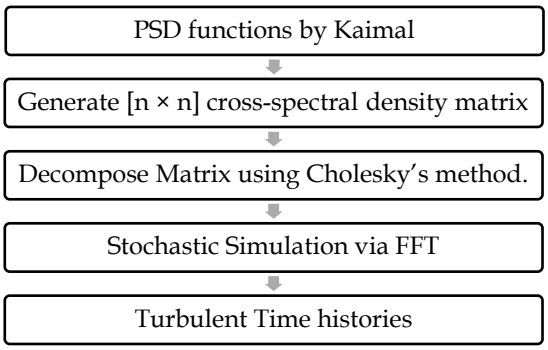

Figure 3: Wind velocity time history generation procedure

Figure 4 shows the power spectra used.

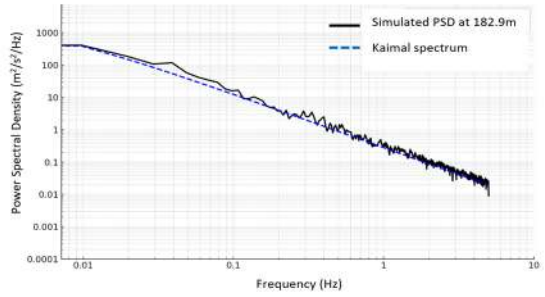

Figure 4: Power spectra at top of the building at wind velocity 30m $s^{-1.}$

Using the procedure above, synthetic velocity time histories were generated at 59 vertical positions. Figure 5 shows the generated wind velocity time histories at storey 1 and storey 59 for a wind velocity of $30ms^{-1}$.

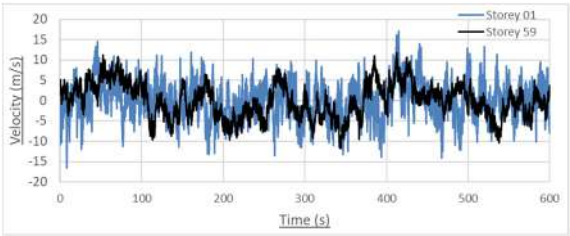

Figure 5: Generated wind turbulent time histories for $30ms^{-1}$ in along wind direction

The quasi-steady aerodynamic load model was used to convert the wind velocity fluctuations into time-dependent buffeting forces. The drag (along-wind) force per story was calculated as:

$$D_B(t) = \frac{1}{2} \cdot \rho U(z)^2 B h \left[C_D \left(1 + 2 \cdot \frac{u(z,t)}{U(z)}\right) + \left(\frac{dC_D}{d\theta} - C_L\right)\frac{v(z,t)}{U(z)}\right] \quad (1)$$

A drag coefficient C_D=1.21, obtained from wind tunnel tests on the CAARC model, was used. Figure 6 shows the buffeting loads generated in Along wind direction at storey 1 and storey 59 for a wind velocity of $30ms^{-1}$.

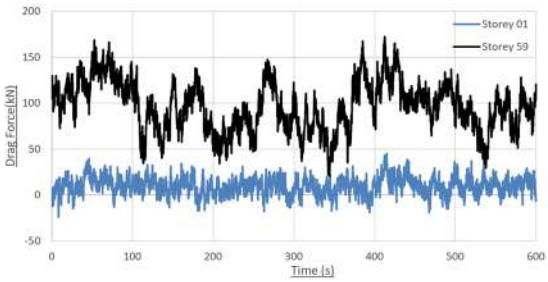

Figure 6: Buffeting load time histories at 30m/s reference wind velocity

3.3 Linear time history analysis

A Linear Modal Time History Analysis (LTHA) was performed in ETABS by applying unidirectional buffeting loads at each floor's centre node. Simulations covered wind speeds from 5–55 m/s in 5 m/s increments, with 6000 steps at 0.1-second intervals.

3.4 Nonlinear time history analysis

A nonlinear time history analysis (NLTHA) was carried out using OpenSees to capture inelastic structural response under wind loads. The building was modelled with fibre-based beam-column elements and layered shell elements for the core wall. Material models included Concrete02 and Steel02. The structure modelled in OpenSees is shown in Figure 8. Wind loads were applied as time-varying functions to the master node at each floor level, and the analysis was performed for a 30 m/s reference wind speed.

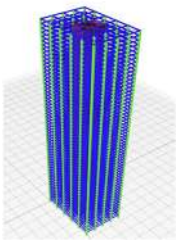

Figure 7: Nonlinear structural model in OpenSees

3.5 Parametric study

To evaluate key influencing parameters:

- LTHA was conducted for multiple wind speeds (5–55 m/s).
- Damping ratio was varied from 0.1% to 5%.
- Rayleigh damping models using initial, tangent, and secant stiffness were compared.

4. Results and Discussion

4.1 Modal analysis results

The linear elastic model closely matched the CAARC benchmark, with fundamental frequencies of 0.196 Hz and 0.204 Hz. Despite a slightly higher mass (176.6 kg/m² vs. 160 kg/m²), the agreement in dynamic properties validates the model for wind response and performance-based analysis.

Table 1: Natural frequency values of elastic model

Mode	Natural Frequency (Hz)
01	0.196
02	0.203

4.2 Validation results

The validation study compared average top displacement from Linear Time History Analysis (LTHA) with CAARC wind tunnel test results (Melbourne, 1980) across a range of wind velocities.

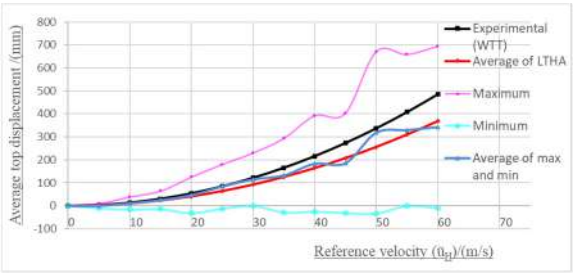

Figure 9: Comparison of LTHA results and experimental results.

As shown in Figure 9, the simulated response closely follows the experimental trend with a slight underestimation, confirming that the LTHA model reliably captures wind-induced behaviour for use in performance-based analysis.

4.3 LTHA results

Structural response increases with both wind speed and elevation due to flexibility and dynamic amplification in tall buildings. As shown in Figures 10, peak acceleration exceeds the 200 mm/s² comfort threshold beyond 35 m/s. Figure 11 shows that inter-story drift increases moderately up to 50 m/s but rises significantly beyond that.

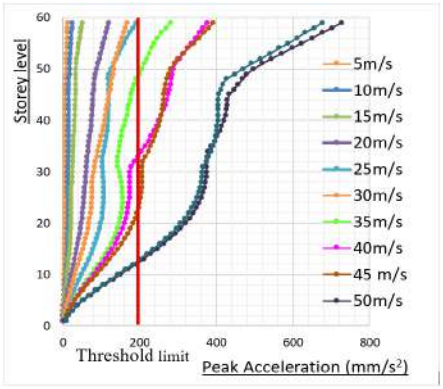

Figure 10: Peak acceleration vs storey level

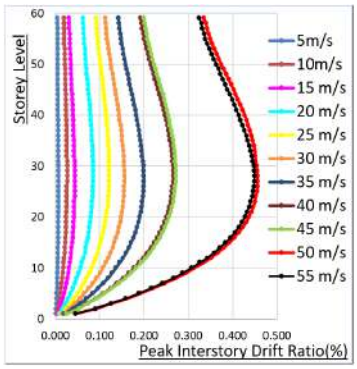

Figure 11: Peak inter-storey drift vs storey level

4.4 Effect of damping on building response

Figure 12 illustrates that peak acceleration decreases significantly with increased damping, especially at upper storeys.

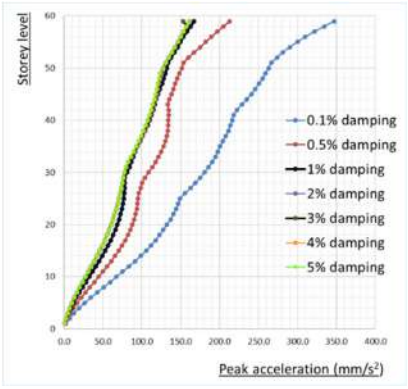

Figure 12: Effect of damping on Peak acceleration.

4.5 NLTHA results

Figure 13 shows that nonlinear analysis results in slightly lower peak accelerations across all floors compared to linear analysis, due to energy dissipation and period elongation from inelastic behaviour.

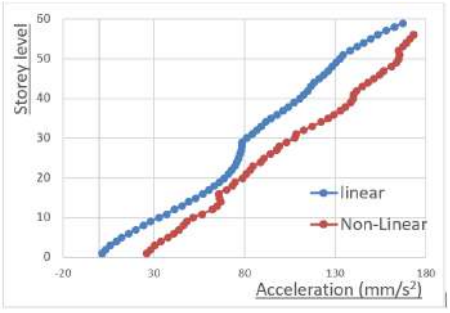

Figure 13: Comparison of acceleration

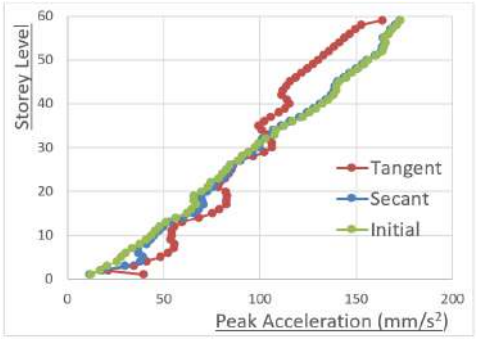

Figure 14: Comparison of inter-storey drift

4.6 Comparison of Reyleigh damping models

Figure 14 shows that the tangent stiffness damping model results in higher accelerations at lower stories and reduced accelerations at upper stories compared to initial and secant stiffness models. This variation is due to the reduced damping contribution in upper levels where structural stiffness degrades, demonstrating the influence of damping model selection in nonlinear analysis.

5. Conclusions

A validated virtual wind tunnel framework was developed by integrating synthetic wind load generation and both linear and nonlinear FEM modelling, benchmarked against CAARC wind tunnel data. Rayleigh damping variations showed minimal effect on overall behaviour, validating their use in SLS analysis. Parametric studies confirmed that response increases with wind speed, while low damping significantly amplifies accelerations. The nonlinear model supports extension to ULS, enabling realistic assessment of inelastic behaviour and damage for performance-based wind design. This approach offers a scalable foundation for future applications such as fragility analysis and wind-resilient structural optimization.

References

Bezabeh, M.A., Bitsuamlak, G.T. and Tesfamariam, S. (2020) 'Performance-based wind design of tall buildings: concepts, frameworks, and opportunities', *Wind and Structures*, 31(2), pp. 103–142. doi: 10.12989/WAS.2020.31.2.103.

Caracoglia, L. and Jones, N.P. (2009) 'Analysis of full-scale wind and pressure measurements on a low-rise building', *Journal of Wind Engineering and Industrial Aerodynamics*, 97(3–4), pp. 157–173. doi: 10.1016/j.jweia.2009.06.001.

Ciampoli, M., Petrini, F. and Augusti, G. (2011) 'Performance-Based Wind Engineering: Towards a general procedure', *Structural Safety*, 33(6), pp. 367–378. doi: 10.1016/j.strusafe.2011.07.001.

Deodatis, G. (1996) 'Simulation of ergodic multivariate stochastic processes', *Journal of Engineering Mechanics*, 122(8), pp. 778–787. doi: 10.1061/(asce)0733-9399(1996)122:8(778).

Jeong, S.Y., Alinejad, H. and Kang, T.H.-K. (2021) 'Performance-based wind design of high-rise buildings using generated time-history wind loads', *Journal of Structural Engineering*, 147(10), 04021134. doi: 10.1061/(ASCE)ST.1943-541X.0003077.

Melbourne, W.H. (1980) 'Comparison of measurements on the CAARC standard tall building model in simulated model wind flows', *Journal of Wind Engineering and Industrial Aerodynamics*, 6(1–2), pp. 73–88. doi: 10.1016/0167-6105(80)90023-9.

RESPONSE OF PRECAST BEAM-TO-COLUMN CONNECTIONS FOR QUASI STATIC LATERAL LOADING

Thayaparan A.[1,*], Sowminiyan S.[1], and Wijesundara K.K.[1]

[1]Department of Civil Engineering, University of Peradeniya, 20404, Sri Lanka

[*] e19401@eng.pdn.ac.lk

Abstract

Precast concrete construction offers advantages in speed, cost-efficiency, and quality control. However, achieving reliable beam-to-column connections remains a key challenge for ensuring structural integrity under lateral loading. This study introduces a novel precast moment-resisting bolted connection, incorporating couplers and internal anchorage rods to enhance load transfer and stability. Initial hand calculations were performed assuming monolithic behavior to determine design actions. Connection detailing followed Eurocode 2, Eurocode 3, and PCI guidelines. A detailed finite element model was developed in MIDAS FEA NX to simulate the connection's behavior under quasi-static lateral loading, accounting for material nonlinearities, realistic boundary conditions, and displacement-controlled loading applied at the beam tip. The results confirmed that the proposed connection effectively resists lateral loads, with improved moment transfer performance. The internal anchorage system significantly enhanced behavior under increasing displacement. The assumed dominant failure mode—end plate yielding—was validated through simulation, and only a 1.4% difference was observed between predicted and numerical outcomes. The findings support the reliability and accuracy of the proposed design guideline and demonstrate the connection's potential for seismic and lateral load-resisting precast applications. Further studies are recommended for experimental validation and investigation of alternative geometries.

Keywords: Precast Beam-to-column connection, Bolted connection, Quasi-static lateral loading, Finite element analysis

1. Introduction

Precast beam-to-column connections are integral to modern prefabricated construction, offering benefits such as accelerated construction, consistent quality, and reduced on-site labour compared to traditional cast-in-place methods. However, their structural behaviour under combined vertical and lateral monotonic loading, as experienced during extreme events such as earthquakes or wind-induced displacements requires careful evaluation. Ensuring that these connections can achieve full moment transfer and replicate monolithic behaviour is essential for safety and performance. This research focuses on the development and evaluation of a novel precast beam-to-column connection, designed to meet strength, ductility, and constructability requirements under monotonic lateral loading, in line with the provisions of Eurocode-based structural design standards.

2. Literature review

Ensuring structural continuity and adequate force transfer at beam-to-column joints remains a major challenge in precast concrete construction, particularly under quasi-static monotonic lateral loading. Several innovative approaches have been developed to improve connection performance and achieve monolithic-like behaviour.

Senturk et al. (2020) proposed a novel plate anchorage system that transfers compressive forces through bearing plates and tensile forces via rivet-headed longitudinal bars anchored into a drilled beam endplate. Finite element models developed in ABAQUS using an explicit dynamic procedure, along with full-scale experimental testing, confirmed the superior ductility, deformability, and energy dissipation capacity of the proposed monolithic-like connection compared to conventional systems.

Meydanli Atalay and Ozden (2021) developed a hybrid moment-resisting connection using high-strength post-tensioning bolts (60SiCr7) at the beam ends. These bolts provide clamping force

for shear transfer and contribute to flexural resistance while minimizing stress loss. Steel corbels placed above and below the beam prevent vertical sliding on the column face, enhancing stiffness and enabling the joint to behave more like a monolithic connection.

Zhang et al. (2024) conducted a finite element study highlighting the role of steel detailing in connection performance. Increasing end plate thickness and bolt preload improved bearing capacity and initial stiffness, while reducing stiffness degradation. Although focused on cyclic behaviour, these findings are relevant to monotonic loading scenarios.

3. Methodology

3.1 Introduction to Methodology

Precast concrete construction is widely adopted due to its advantages in improved quality control, reduced construction time, and enhanced cost-efficiency. However, a fundamental challenge lies in ensuring the structural reliability of connections between precast elements, as they must effectively transfer various forces and maintain overall stability. To address this, the research aims to develop a novel precast beam-to-column connection that is structurally stable and seismically resilient under quasi-static lateral loading. The primary goal of this research is to create a reliable and practical tool for engineers to assess and optimize connections, specifically tailoring them to the demands of seismic and lateral load-resisting structures. The approach synthesizes relevant provisions from Eurocode 2 (EC2), Eurocode 3 (EC3) and the PCI Design Handbook to propose a unified, rational design method.

As per Figure 1, the research procedure begins with the literature review followed by the conceptualization of an innovative beam-to-column connection detail, designed to enhance structural performance under lateral loading. This is followed by the development of an optimized design guideline aimed at evaluating critical performance parameters, including moment capacity and ductility. The investigation is primarily based on numerical analysis, allowing for a detailed assessment of the connection's behaviour. A comprehensive finite element model was developed using MIDAS FEA NX to simulate the connection's response under quasi-static lateral loading, with particular emphasis on capturing its nonlinear characteristics. The results presented in this study are limited to numerical predictions, which form the basis for evaluating the effectiveness and applicability of the proposed design guideline.

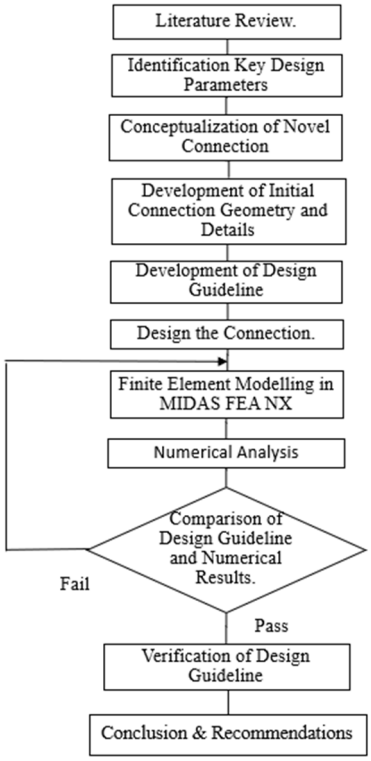

Figure 1: Methodology Flowchart

3.2 Development of Design Guideline

The design guideline was focused on a novel moment-resisting connection for precast concrete framed buildings. It was considered crucial for enhancing overall stability and load-carrying capacity by resisting both bending moments and shear forces. A code-based design methodology was adopted, incorporating Eurocode 3, Eurocode 2, and the PCI Design Handbook to identify all potential failure modes, including bolt shear/tension, end plate flexure, concrete shear friction, and anchor rebar shear/tension. A new design guideline was developed by synthesizing the strengths of these established codes to ensure both safety and structural performance. Each design step from material selection and geometric detailing to failure mode analysis was addressed methodically, with particular emphasis placed on achieving full moment capacity and ductile behaviour. The guideline was structured to function as both a practical tool for design engineers and a reference framework for researchers investigating advanced precast connection systems.

3.3 Finite Element Modelling

To investigate the seismic performance of the connection, detailed nonlinear finite element (FE) model was developed using MIDAS FEA NX. The study employed a quasi-static lateral loading protocol to simulate seismic demands, with emphasis on accurately capturing material and geometric nonlinearity. Concrete and steel components, including end plates, bolts, and anchor rods, were modelled using 3D solid elements, while reinforcement bars were represented using embedded truss elements. Nonlinear material models were applied: concrete was defined with tension cracking, compressive crushing, and softening behaviour, while steel was modelled as an elastic–plastic material with strain hardening. Advanced contact interfaces were defined between steel and concrete surfaces, bolts and couplers, and other connection interfaces to simulate realistic load transfer and bearing behaviour. Boundary conditions were set to replicate experimental test setups, with both ends of the column fully restrained. Mesh convergence and quality checks were conducted to ensure result accuracy, with refined meshing in the connection zone as shown in Figure 2. The analysis captured key behaviours such as deformation and strain distribution, providing critical insights into the connection's moment capacity and ductility under seismic loading. The results support the development of a practical design guideline for precast seismic connections.

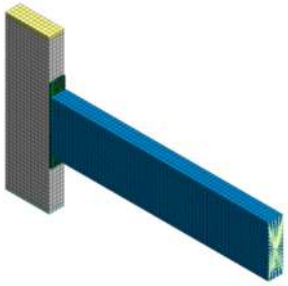

Figure 2: Meshed Finite Element Model

4. Results and Discussion

4.1 Load – Displacement Behaviour

The load–displacement curve derived from the finite element model is shown in Figure 3. The connection exhibits a nonlinear response characteristic of ductile flexural behaviour, with gradual stiffness degradation as displacement increases. The connection reached an applied peak load of 96 kN, corresponding to a moment capacity of 288 kNm at the critical joint section. This value is in strong agreement with the moment capacity of 285 kNm calculated using the proposed design guideline, with nearly 1.4% variation. This correlation validates the reliability of the design guideline and confirms the predictive accuracy of the numerical model.

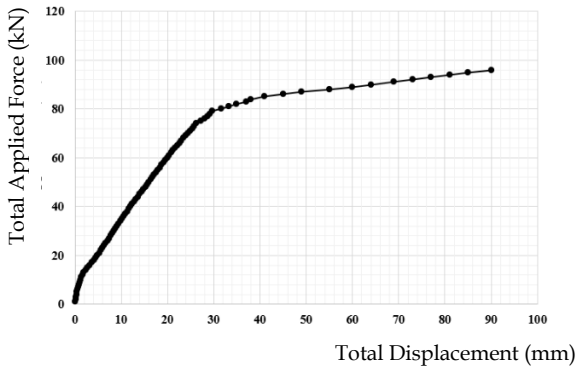

Figure 3: Load-Displacement Curve

4.2 Strain Variation and Joint Behaviour

Figure 4 illustrates the overall strain distribution pattern within the joint region. Distinct tension and compression zones are evident across the beam depth at the beam–column interface, consistent with expected flexural action. The upper region of the connection, particularly at the beam–plate interface, shows strain concentration around the bolts, indicating their role in resisting tensile forces. The lower region experiences compressive strain, where plate yielding is observed.

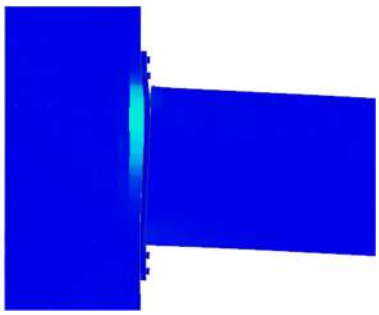

Figure 4: Strain Distribution Pattern

The onset of yielding is localized in the steel end plate, demonstrating its active role in moment resistance and energy dissipation. The connection does not exhibit signs of brittle failure, and the strain patterns suggest that a ductile failure mechanism governs the response which is an essential requirement for seismic-resistant design.

4.3 Strain Distribution in Joint Elements

To further understand the internal behaviour of the connection, Figure 5 shows the strain distribution in key joint elements: bolts, end plate, and anchor reinforcement bars.

Quantitative values of maximum strain are summarized in Table 1.

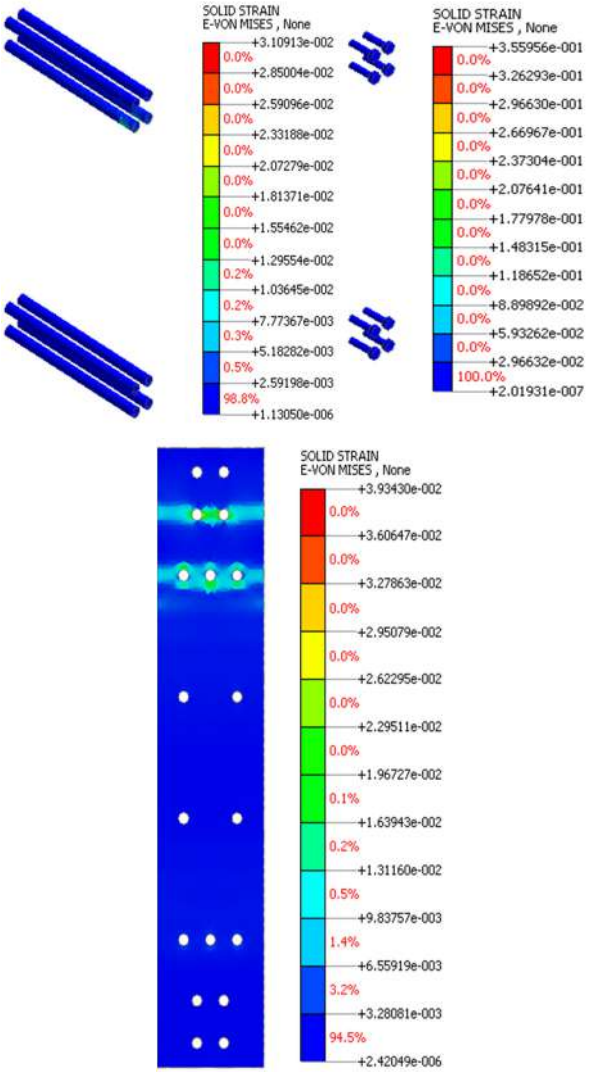

Figure 5: Strain Distribution in Key Joint Elements

Table 1: Maximum Strain in Joint Components

Component	Maximum Strain
Bolts	≤ 0.0032
End Plate	0.0364
Anchor Rebar	0.0017

The results indicate that maximum strain occurs in the steel end plate, confirming that it undergoes significant plastic deformation under cyclic loading. This validates the design assumption that the end plate serves as the primary energy-dissipating element. In contrast, the anchor reinforcement bars experience low levels of strain, indicating they remained within the elastic range and were effective in transferring forces without yielding.

Importantly, the bolts exhibited negligible strain, suggesting that they remained elastic throughout the loading history. This implies that the force transfer mechanism relies more on the yielding of the steel plate and the anchorage system, rather than bolt elongation or slip. This behaviour helps avoid premature bolt failure and contributes to the ductile performance of the connection.

5. Conclusions

A design guideline for a bolted precast beam-to-column connection was developed and subsequently validated through finite element analysis. A discrepancy of only 1.4% was observed between the predicted values and the numerical simulation results, indicating that the proposed guideline offers a highly accurate and reliable estimation of the connection's structural performance.

In the design guideline, it was assumed that the end plate failure mode would be dominant. This assumption was confirmed through finite element analysis, in which plate failure was also identified as the primary mode. The agreement between the assumed and simulated failure modes further supports the reliability and

References

Meydanli Atalay, H. and Ozden, S. (2021) 'Cyclic Behavior of Beam-Column Connections in Precast Structures', *Frontiers in Built Environment*,7. doi: 10.3389/fbuil.2021.639778.

Senturk, M. et al. (2020) 'Development of a monolithic-like precast beam-column moment connection: Experimental and analytical investigation', *Engineering Structures*, 205. doi: 10.1016/j.istruc.2023.105778.

Zhang, H. et al. (2024) 'Numerical analysis of a prefabricated concrete beam-to-column connection with bolted end plates', *Structures*, 59. doi: 10.1016/j.istruc.2023.105778.

MODELING OF INELASTIC BUCKLING OF MEMBERS IN LATTICE TOWERS USING FORCE-BASED FIBER BEAM-COLUMN ELEMENTS

Gallehewa, D.H.[1,*], Bandara, U.L.N.T.[1*], and Wijesundara, K.K.[1]

[1]Department of Civil Engineering, University of Peradeniya

[*] e19112@eng.pdn.ac.lk

Abstract

Capturing inelastic buckling of complex structures has been a challenging, yet demanding phenomenon for many decades. This study intends to develop a model to capture the inelastic buckling of members in lattice towers utilizing force-based fiber beam-column elements. The structural integrity of lattice towers which serve telecommunications and power transmission networks can be compromised under high wind loads because compression members experience buckling. The research proposes to create and verify a numerical model that effectively simulates the inelastic buckling behaviors of non-symmetric lattice tower sections. The proposed methodology utilizes force-based fiber beam-column elements to precisely represent material nonlinearity and geometric imperfections. The research develops a numerical model which undergoes validation with experimental data and uses parametric studies to assess how end conditions, and initial imperfections influence the model behavior. The research will offer a modeling approach to analyse lattice towers to capture lateral load capacity and failure modes. This research will lead to improved knowledge about inelastic buckling behavior and better-designed safer lattice towers considering the performance.

Keywords: inelastic buckling, lattice towers, force-based fiber beam–column elements, non-symmetric sections.

1. Introduction

Lattice towers support critical infrastructure but are vulnerable to inelastic buckling under lateral loads. Traditional analysis and design methods either ignore post-buckling or demand heavy computational models to capture the real tower response under lateral loads. This research introduces a balance between the accuracy and high computational cost by utilizing force-based fiber beam–column approach that can account for material nonlinearity and large displacements. Initially, a Single brace element is optimised through a series of parametric studies done under monotonic and cyclic loading tests. Then applied in a full-scale tower to conduct a static pushover analysis to assess the capacity and the failure mode.

2. Literature Review

Uriz et al. in 2008 demonstrated that force-based fiber beam–column elements can accurately capture inelastic buckling and energy dissipation with far lower computational cost than full 3D models. Wijesundara et al. in 2014 applied this beam column element, to capture the inelastic buckling behaviour of steel braces in concentrically braced frames. Benchmark experiments include Liu and Chantel's in 2011 eccentric compression tests on unequal-leg angles and Liu et al.'s in 2023 cyclic tests on equal-leg angles. Szafran and Rykaluk's in 2016 full-scale pushover of a 40m tower provides capacity curves, validating the method for global tower analysis.

3. Methodology

Figure 1 shows the general steps of the methodology of this study.

3.1 Development of a Numerical Model for a Single Brace

Two steel angle sections, a 1200 mm unequal-leg angle (L76×51×6.4 mm) and a 3560 mm equal-leg angle (L90×90×7 mm) are modeled in STKO/OpenSees using force-based fiber beam–column elements. Cross sections are discretized into uniaxial fibers with the Menegotto–Pinto Steel02, while a corotational formulation captures large-displacement effects. This setup provides a robust foundation for simulating inelastic buckling behavior.

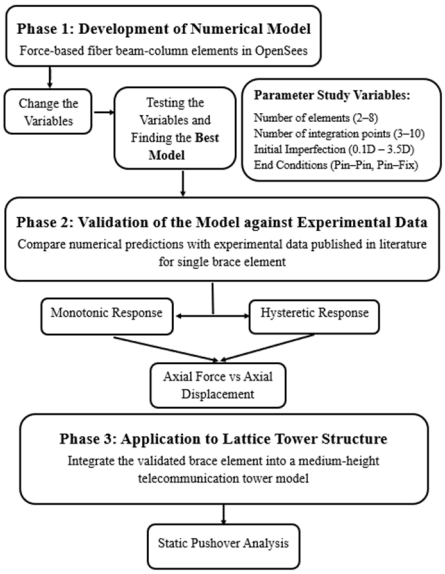

Figure 8: Flow chart of the methodology

3.2 Parametric Study for a Single Brace

A systematic parametric study evaluates how key modeling choices affect brace response under monotonic axial-compression and cyclic displacement-controlled loading. Key Variables include element count (2–8 per brace), Gauss integration points (3–10 per element), initial mid-span imperfection amplitude (0.1% – 3.5% of member length) and end-condition stiffness (pin–pin versus pin-fixed). The study provides insight to select of an optimal discretization and imperfection level that balances numerical accuracy with computational efficiency.

3.3 Validation against Experimental Data for a Single Brace

The optimized brace model is validated against experimental. Monotonic buckling predictions are compared with compression data for unequal-leg angles, and hysteretic loops are corelated against low-cycle cyclic tests on equal-leg angles. Validation measures include relative error in peak load, curve matching and post buckling response.

3.4 Application of the Validated Brace Model to a Lattice Tower

The validated brace elements are integrated into a three-dimensional model of a 40 m telecommunication lattice tower. Member profiles and material definitions are same as the single-brace setup. Base nodes are fully fixed, and a rigid diaphragm at the tower top applies uniform lateral displacements via multi-point constraints.

3.5 Analysis of Lattice Tower Structures

A displacement-controlled pushover analysis is conducted by incrementally imposing lateral displacements at the diaphragm. Newmark-β integration with Newton Line traces the global capacity curve. Key outputs such as the base shear versus top-node displacement, failure mode is recorded to assess tower performance under lateral loading.

4. Results and Discussion

4.1 Monotonic Response of a Single Brace

4.1.1 Numerical Modeling

Monotonic buckling was simulated in STKO/OpenSees using force-based fiber beam–column elements with Steel02 fibers and corotational kinematics. The 76×51×6.4 mm, 1200 mm unequal-leg angle was discretized into fiber sections, and axial displacement control generated the numerical buckling envelope, which aligns with Liu and Chantel in 2011 experimental data.

4.1.2 Parametric study

Figure 2 compares 2, 4 and 6 elements per brace, showing nearly identical force–displacement curves and confirming that 2 elements suffice.

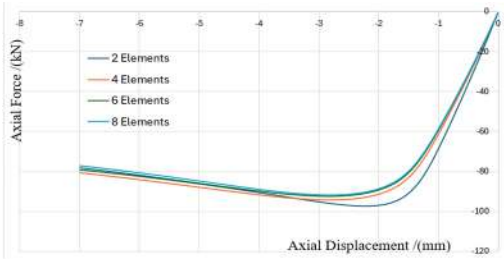

Figure 9: Influence of Number of Elements

Figure 3 illustrates convergence of buckling load for 3, 5, 6, 8 and 10 Gauss integration points, with 5 points offering a balance of accuracy and efficiency.

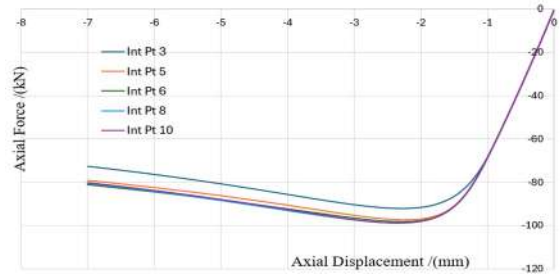

Figure 10: Influence of Number of Integration Points

4.1.3 Validation of the single brace under monotonic loading

Figure 4 shows axial force–displacement responses for major-axis bending with mid span camber values from 0.5 % to 3.5 %, overlaid on the experimental curve. A 3 % imperfection yields the closest agreement in both peak load and initial stiffness.

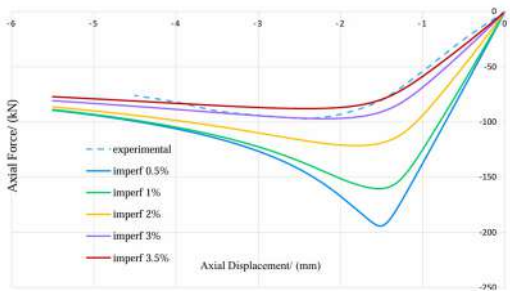

Figure 11: Influence of Initial Imperfections under Pin-Fixed Condition

4.2 Hysteretic Responses of a Single Brace

4.2.1 Numerical Modeling

Cyclic behavior was modeled in STKO/OpenSees using force-based fiber beam–column elements with Steel02 fibers and corotational kinematics. The 90×90×7 mm equal-leg angle was discretized into fiber sections, and displacement-controlled loading is conducted to generate the numerical hysteresis loops.

4.2.2 Parametric study

Figure 5 compares 2, 4 and 6 elements per brace, showing nearly identical force–displacement curves and confirming that 2 elements suffice.

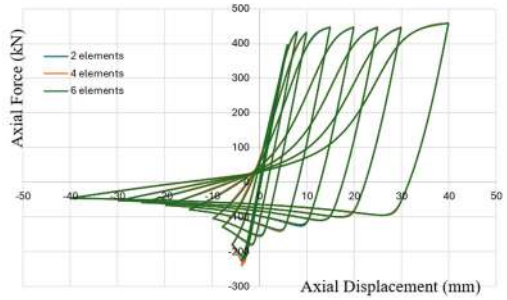

Figure 12: Influence of Number of Elements

Figure 6 illustrates convergence of buckling load for 3, 5, 6, 8 and 10 Gauss integration points, with 5 points offering a balance of accuracy and efficiency.

Figures 7 and 8 illustrate how boundary condition changes can influence cyclic response. Under fixed-pinned restraints, the brace exhibits a higher initial peak load, larger hysteretic loop area and slower stiffness degradation compared to the pinned-pinned case. The fixed-pinned configuration also shows greater energy dissipation per cycle and a more gradual post-peak strength decay, highlighting the importance of semi-rigid end connections in enhancing inelastic buckling resistance.

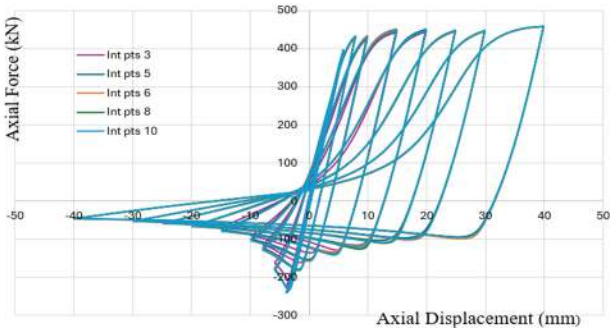

Figure 13: Influence of Number of Integration Points

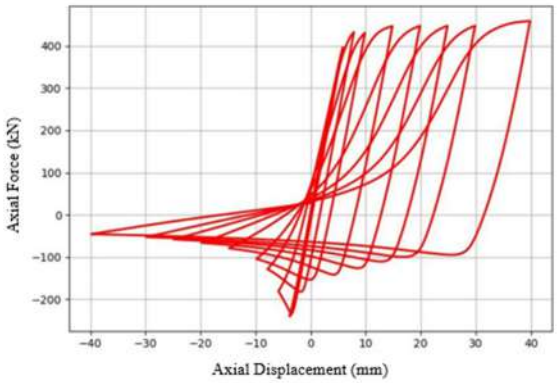

Figure 14: Hysteretic envelopes under pinned–fixed end conditions

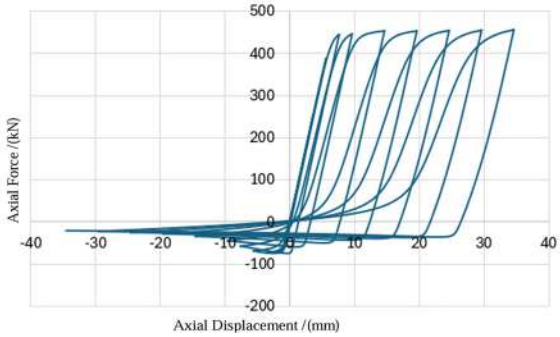

Figure 15: Hysteretic envelopes under pinned–pinned end conditions

4.2.3 Validation of a single brace under cyclic loading

Figure 9 compares OpenSees hysteresis loops with Liu et al. in 2023 experimental cycles for the 90×90×7 mm angle. The validated model accurately demonstrates its ability to reflect real structural behavior under cyclic loading.

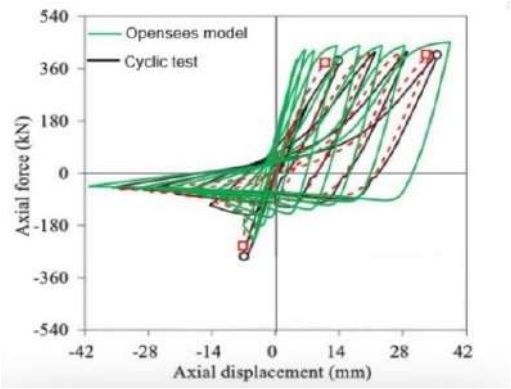

Figure 16: Comparison of numerical and experimental axial force–displacement curves

4.3 Full-Scale Tower Pushover Analysis

The calibrated single brace model with two elements, 5 integration points and imperfection of 1% the initial length on the middle node was applied in a 40 m lattice-tower pushover using STKO/OpenSees. Figure 10 shows the resulting base shear versus top-node displacement curve. The curve demonstrates a numerical peak capacity of 134 kN compared to the experimental 132.5 kN, corresponding to just a 1.1 % deviation. Thus, the numerical model developed can be successfully validated.

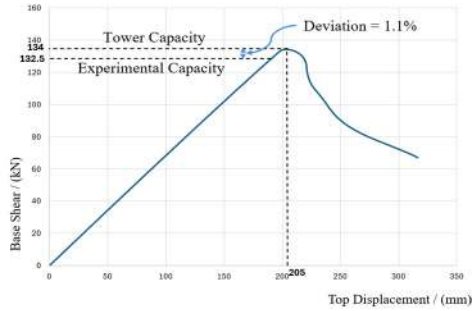

Figure 17: Base shear versus top-node displacement, comparing numerical peak capacity with the experimental

In Figure 11, SLS and ULS design loads (83.1 kN and 103.5 kN) are overlaid, revealing substantial reserve capacity beyond standard limit state design loads.

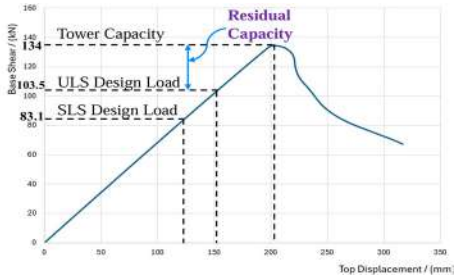

Figure 18: Tower capacity curve overlaid with SLS and ULS design loads and residual capacity

5. Conclusions

A single brace, modeled with two force-based beam–column elements, five Gauss integration points and a 1 % initial camber can accurately capture both the initial buckling response and the cyclic post-buckling response.

The calibrated brace model when incorporated into a full-scale lattice tower, can effectively represent realistic boundary conditions. By comparison with experimental results confirmed that the model can accurately predict both the lateral load capacity and the failure mechanism of the structure.

Pushover analysis of the tower highlights that Ultimate Limit State (ULS) design may underestimate structural capacity. Both SLS and ULS design loads lie within the elastic response range, but a significant reserve capacity beyond ULS design load can be seen. This suggests that more efficient designs can be achieved through nonlinear analysis.

References

Liu, J. *et al.* (2023) 'Phenomenological hysteretic model for fixed-end steel equal-leg angle: Development and application', *Thin-Walled Structures*, 183. doi: 10.1016/j.tws.2022.110335.

Liu, Y. and Chantel, S. (2011) 'Experimental study of steel single unequal-leg angles under eccentric compression', *Journal of Constructional Steel Research*, 67(6), pp. 919–928. doi: 10.1016/j.jcsr.2011.02.005.

Szafran, J. and Rykaluk, K. (2016) 'A full-scale experiment of a lattice telecommunication tower under breaking load', *Journal of Constructional Steel Research*, 120, pp. 160–175. doi: 10.1016/j.jcsr.2016.01.006.

Uriz, P., Filippou, F. C. and Mahin, S. A. (no date) 'Model for Cyclic Inelastic Buckling of Steel Braces'. doi: 10.1061/ASCE0733-94452008134:4619.

Wijesundara, K. K., Nascimbene, R. and Rassati, G. A. (2014) 'Modeling of different bracing configurations in multi-storey concentrically braced frames using a fiber-beam based approach', *Journal of Constructional Steel Research*, 101, pp. 426–436. doi: 10.1016/j.jcsr.2014.06.009.

PRINTABLE CONCRETE WITH PARTIAL AGGREGATE REPLACEMENT BY WASTE PLASTIC AND POLYTHENE

Dilaksha. J.[1,*], Luxshiga. N.[1], and Bandara. C. S.[1]

[1]Department of Civil Engineering, Faculty of Engineering, University of Peradeniya, Sri Lanka

* e19077@eng.pdn.ac.lk

Abstract

This research presents a sustainable approach to 3D printable concrete by partially replacing natural coarse aggregates (NCA) with recycled High-Density Polyethylene (HDPE) waste. A modified mix design incorporated 20% fly ash as a cement substitute and maintained a constant water-to-cement ratio of 0.32. Concrete samples were prepared with 0%, 10%, 30%, and 100% HDPE aggregate replacements. Fresh properties, evaluated through mini slump and flow table tests, showed acceptable workability, enhanced by the use of a high-range superplasticizer (Plastobuild ES). Compressive strength tests at 1, 7, and 21 days revealed that the 30% HDPE mix achieved a good balance between flowability (160 mm), mechanical strength (36.06 MPa), and sustainability. Stress–strain behaviour was observed using strain gauges. Preliminary Finite Element Method (FEM) simulations were initiated using Abaqus, employing the Concrete Damaged Plasticity (CDP) model for cube compression and the Mohr-Coulomb model for layered printing simulation. While still at an initial stage, these models provide a basis for future numerical validation and buildability assessment of plastic-modified printable concrete.

Keywords: 3D Printable Concrete, Recycled Plastic Aggregates, Finite Element Method (FEM), Sustainable Construction

1. Introduction

This 3D printable concrete is an emerging construction method that enables automated, layer-by-layer fabrication of structures without the need for conventional formwork, offering advantages in design efficiency and material usage. However, its reliance on natural coarse aggregates and high cement content contributes to environmental degradation and carbon emissions. Meanwhile, the accumulation of plastic waste, particularly High-Density Polyethylene (HDPE), presents an ongoing sustainability challenge due to its low recycling rates. In response to these issues, this study aims to investigate the use of recycled waste plastic as aggregates in printable concrete, focusing on its potential to reduce environmental impact while maintaining the fresh and mechanical properties necessary for successful 3D printing applications.

2. Literature review

2.1 Sustainable Use of Plastic Waste

The environmental implications of plastic waste have prompted researchers to explore sustainable solutions, such as incorporating recycled plastics into construction materials. Plastics like HDPE, polyethylene terephthalate (PET), and polypropylene (PP) are being studied for partial aggregate replacement in concrete due to their abundance and durability (Rigamonti et al., 2014; Ilyas et al., 2018). Recycling these plastics not only mitigates environmental pollution and landfill usage but also supports circular economy practices and reduces the carbon footprint associated with conventional concrete. Optimal performance has been observed at substitution levels around 10–15%, though higher contents can negatively impact mechanical properties (Abeysinghe et al., 2021; Kangavar et al., 2022).

2.2 Properties of Printable Concrete

The rheological and mechanical performance of 3D printable concrete is highly sensitive to mix design, especially when modified with plastic waste. Printable concrete requires a balance of flowability, buildability, and interlayer bonding to ensure structural stability during layer-by-layer construction (Kazemian et al., 2017; Colyn et al., 2024). Additives such as fly ash, silica fume, nano clay, and HPMC are used alongside plastic particles to tailor the mix. However, plastic addition often reduces flowability and fresh density, requiring superplasticizers for

compensation (Chunsheng et al., 2025). Buildability and compressive strength are also influenced by print orientation, nozzle shape, and material cohesion, with PET and HDPE mixes achieving acceptable strengths around 25 MPa at 10% replacement levels.

2.3 Modeling and Simulation Techniques

Recent advances in numerical modelling have improved the prediction of printable concrete performance. The Concrete Damage Plasticity (CDP) model in ABAQUS effectively simulates stress–strain behaviour, failure patterns, and interlayer bonding in mixes with recycled plastics (Liu et al., 2021). A time-dependent Mohr-Coulomb failure criterion has also been applied for simulating layer-wise behaviour, incorporating key material properties (Wolfs, Bos & Salet, 2018).

3. Methodology

This study adopted a three-pronged approach—environmental assessment, experimental investigation, and numerical modelling—to evaluate the feasibility of using recycled HDPE as a partial replacement for coarse aggregates in 3D printable concrete.

3.1 Environmental Assessment

An environmental impact study was first carried out to assess the viability of using plastic waste in concrete. HDPE was selected based on its local availability, chemical stability, and compatibility with cementitious materials. A cradle-to-gate life cycle assessment (LCA) was performed to estimate CO_2-equivalent emissions per cubic meter for varying HDPE replacement levels (0%, 10%, 30%, 100%). Emission factors were sourced from literature, and HDPE was treated as carbon-neutral. A cost-benefit analysis was also conducted using current market prices of materials.

3.2 Experimental Investigation

Two main experimental phases were conducted. In the first phase, cement was partially replaced with fly ash at 0%, 10%, 20%, and 30% levels to determine the optimal mix. Based on compressive strength performance, a 20% fly ash replacement was selected for further testing.

In the second phase, natural coarse aggregates were replaced with HDPE plastic particles at 0%, 10%, 30%, and 100% volumetric ratios. All mixes maintained a 0.32 water–cement ratio and included a high-range water-reducing admixture to ensure printability.

Fresh concrete properties were evaluated using mini slump cone and flow table tests. Compressive strength tests were conducted on 150 mm cubes at 1, 7, and 21 days in accordance with ASTM C39 standards.

3.3 Numerical Modelling

Finite Element Method (FEM) simulations were performed using ABAQUS software. The Concrete Damage Plasticity (CDP) model was used to simulate the compressive behaviour of concrete cubes incorporating HDPE. A mesh convergence study was conducted to ensure numerical accuracy. Figure 1 illustrates the 3D cube model developed using the CDP approach.

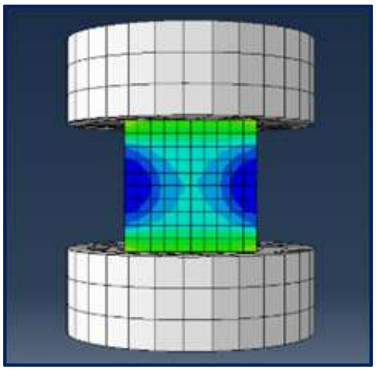

Figure 1: Cube Model with CDP

For buildability assessment, a layer-by-layer printing simulation was developed using the Mohr-Coulomb model. Layers were activated sequentially using the Model Change function, and age-dependent material parameters such as cohesion and stiffness were incorporated. Boundary conditions and mesh refinements were applied to replicate the experimental setup. Figure 2 presents the visualization of the layered printing process used in the simulation.

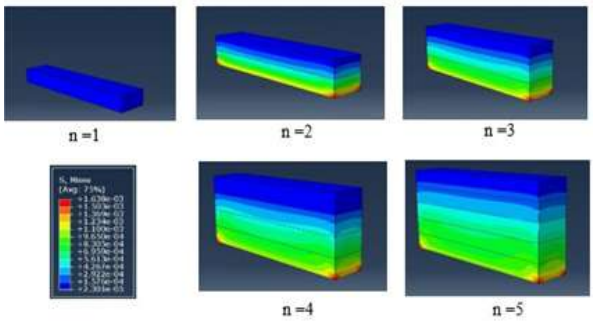

Figure 2: Layers Visualization

4. Results and Discussion

4.1 Experimental Results and Discussion

4.1.1 Workability of Fresh Concrete

Workability was assessed using mini-slump and flow table tests. The control mix (HDPE0) had a slump of 7 mm, while HDPE10 showed a slight decrease to 6 mm due to increased internal friction from HDPE particles. At higher replacements (HDPE30 and HDPE100), slump increased to 12 mm and 16 mm respectively, indicating improved flowability. Figure 3 shows mini slump cone test.

Figure 3: Mini slump cone test

A similar pattern was observed in flow table results, with diameter increasing from 146 mm (HDPE0) to 153.5 mm (HDPE100). This is attributed to the low density and deformability of HDPE particles. Superplasticizer dosage was modified accordingly to maintain mix consistency across all HDPE levels. Figure 4 shows the apparatus which used for flow table test.

Figure 4: Flow table apparatus

4.1.2 Compressive Strength of Hardened Concrete

Compressive strength decreased with increasing fly ash and HDPE content. The OPC-based control mix (FA0) achieved 45.4 MPa, while strength reduced to 44.3 MPa (FA10), 42.6 MPa (FA20), and 34.9 MPa (FA30), leading to the selection of 20% fly ash for further testing. In PFC-based mixes with 20% fly ash, strength declined from 53.82 MPa (HDPE0) to 43.03 MPa (HDPE10), 36.06 MPa (HDPE30), and 24.39 MPa (HDPE100), mainly due to HDPE's weak bonding behaviour. Figure 5 shows the results of compressive strength variation of HDPE replacement.

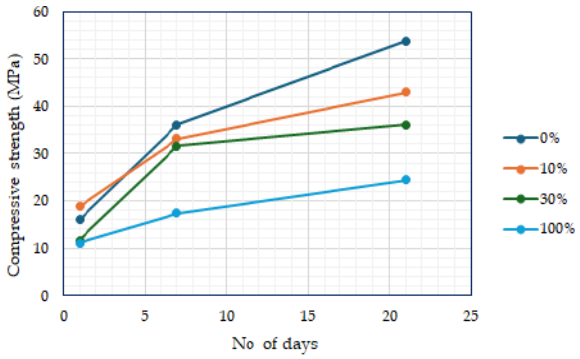

Figure 5: Compressive strength with varying HDPE replacement percentages

4.2 Carbon Emission and Cost Analysis

Carbon emissions per cubic meter decreased slightly with higher HDPE content, primarily due to the reduced use of natural coarse aggregates. Emissions dropped from 400.85 kg CO_2-eq/m³ (HDPE0) to 398.39 kg CO_2-eq/m³ (HDPE100), resulting in a modest reduction of approximately 2.46 kg/m³.

Similarly, the total material cost per cubic meter declined as HDPE content increased. The cost decreased from LKR 44 773.92 (HDPE0) to LKR 34 052.57 (HDPE100), achieving a cost saving of about 24%, mainly due to the elimination of conventional aggregate costs. These findings are summarized in Table 1, which helping to assess the overall efficiency and sustainability of each mix.

Table 4: Impact of HDPE on Strength, Cost, & CO_2 Emissions

HDPE (%)	Strength (MPa)	Cost (LKR/m³)	CO_2-eq (kg/m³)
0	53.82	44 773.92	400.85
10	43.03	43 701.74	400.61
30	36.06	41 557.53	400.12
100	24.39	34 052.57	398.39

5. Conclusions

This study highlights the potential of incorporating recycled HDPE plastic as a sustainable partial replacement for natural

coarse aggregates in 3D printable concrete. The inclusion of HDPE enhanced the flowability of the mix at higher replacement levels while maintaining acceptable levels of printability and buildability. Additionally, HDPE-modified mixes contributed to notable reductions in both carbon emissions and material costs. Although a decline in compressive strength was observed with increasing HDPE content, a 30% replacement ratio was identified as a favourable balance between mechanical performance and sustainability. To complement the experimental work, numerical modelling was initiated using the Concrete Damaged Plasticity (CDP) model for simulating cube compressive behaviour, and the Mohr–Coulomb model for analysing layer-wise performance. Overall, the integration of recycled HDPE into 3D printable concrete presents a promising approach toward environmentally responsible and economically viable construction materials.

References

Abeysinghe, S., Gunasekara, C., Bandara, C., Nguyen, K., Dissanayake, R. and Mendis, P. (2021) 'Engineering performance of concrete incorporated with recycled high-density polyethylene (HDPE)—A systematic review', *Polymers*, 13(11), p.1885. doi: 10.3390/polym13111885

Chunsheng, Z. et al. (2025) 'Effect of double substitution of recycled coarse and fine aggregates on the workability and mechanical properties of 3D printed concrete', *Ceramics-Silikáty*, 69(1), pp.75–92. doi: 10.13168/cs.2024.0067

Colyn, M., van Zijl, G. and Babafemi, A.J. (2024) 'Fresh and strength properties of 3D printable concrete mixtures utilising a high volume of sustainable alternative binders', *Construction and Building Materials*, 419. doi: 10.1016/j.conbuildmat.2024.135474

Ilyas, M., Ahmad, W., Khan, H., Yousaf, S., Khan, K. and Nazir, S. (2018) **'**Plastic waste as a significant threat to environment–a systematic literature review', *Reviews on Environmental Health*, 33(4), pp.383–406. doi: 10.1515/reveh-2017-0035

Kangavar, M.E. et al. (2022b) 'Investigation on the properties of concrete with recycled polyethylene terephthalate (PET) granules as fine aggregate replacement', *Case Studies in Construction Materials*, 16, e00934. doi: 10.1016/j.cscm.2022.e00934

Kazemian, A., Yuan, X., Meier, R., Cochran, E. and Khoshnevis, B. (2017) 'Construction-scale 3D printing: shape stability of fresh printing concrete', *International Manufacturing Science and Engineering Conference*, Vol. 50732, p.V002T01A011. American Society of Mechanical Engineers. doi: 10.1115/MSEC2017-2823

Liu, H. et al. (2021) 'A numerical study on 3D printed cementitious composites mixes subjected axial compression', *Materials*, 14(22), p.6882. doi: 10.3390/ma14226882

Rigamonti, L., Grosso, M., Møller, J., Sanchez, V.M., Magnani, S. and Christensen, T.H. (2014) 'Environmental evaluation of plastic waste management scenarios', *Resources, Conservation and Recycling*, 85, pp.42–53. doi: 10.1016/j.resconrec.2013.12.012

Wolfs, R.J.M., Bos, F.P. and Salet, T.A.M. (2018) 'Early age mechanical behaviour of 3D printed concrete: numerical modelling and experimental testing', *Cement and Concrete Research*, 106, pp.103–116. doi: 10.1016/j.cemconres.2018.02.001

EVALUATION OF WIND EFFECTS ON LIFT-UP BUILDINGS IN HIGH DENSITY URBAN AREAS: A COMPUTATIONAL FLUID DYNAMICS (CFD) APPROACH

D. N. Liyanage[1, *], H. M. D. L. Premadasa[1] and J. A. S. C. Jayasinghe[1]

[1]Department of Civil Engineering, University of Peradeniya, 20404, Sri Lanka

* e19220@eng.pdn.ac.lk

Abstract

This study investigates wind flow around lift-up buildings in dense urban areas using CFD with the RANS method and *k-ω* SST model. Pedestrian wind comfort is assessed for variations in core shape, lift-up height, surrounding building height, and wind direction. Comfort improves when surrounding buildings reach two-thirds of the central height due to wake dissipation. However, when heights are equal under 0° wind, over 30% of the area exceeds Lawson's comfort limit. Greater lift-up height intensifies undercroft flow and discomfort, while core shape shows minimal influence at a fixed aspect ratio. Wind barriers of 2–12 m reduce uncomfortable areas by up to 83%, with the 12 m barrier eliminating discomfort. These findings highlight wind barriers as effective passive measures for enhancing pedestrian comfort in high-density urban settings.

Keywords: CFD simulation, Downwash effect, Lift-up buildings, Pedestrian comfort

1. Introduction

In high-density urban areas, lift-up buildings with elevated ground floors create complex wind patterns that affect pedestrian comfort. Downwash and wind acceleration beneath these structures can cause localized discomfort, especially influenced by nearby building layouts. While general wind effects around tall buildings have been studied, limited research focuses on how lift-up core shape, lift-up height, surrounding building height, and wind direction impact wind comfort in realistic urban settings. This study fills that gap using CFD with a power law wind profile to analyze these factors and evaluate wind barriers as passive solutions to reduce pedestrian wind discomfort.

2. Literature review

Previous studies primarily used experimental or numerical simulations to assess wind effects around lift-up buildings under simplified or isolated conditions (Du et al., 2018), often neglecting the complexity of dense urban environments. Urban form research indicates that surrounding building configuration, both horizontally and vertically, strongly influences local wind behavior. Conventional approaches such as wind codes and wind tunnel testing have limitations in capturing these interactions, making CFD a more effective tool for detailed analysis. However, limited research has examined the combined influence of lift-up geometry, surrounding building height, wind direction, and passive mitigation measures such as wind barriers.

3. Methodology

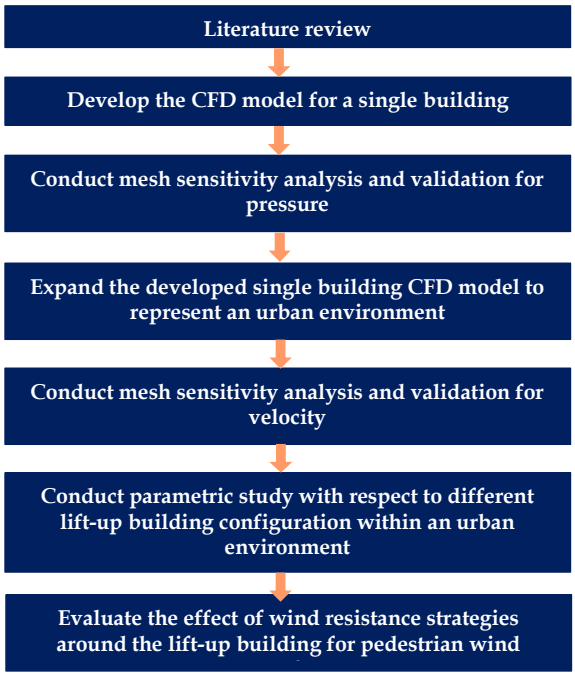

Figure 1: Methodology

The methodology followed in this study is illustrated in Figure 1. Wind flow simulations were subsequently performed using *OpenFOAM* software.

3.1 Model validation

The multiple-building model was validated using experimental data from Liu et al. (2019). The validated configuration, shown in Figure 2, consists of a central high-rise building surrounded by eight low-rise urban blocks.

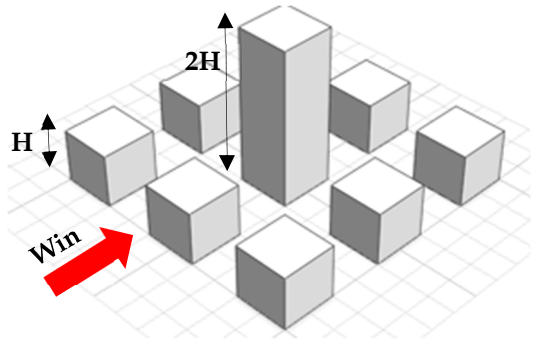

Figure 2: Wind tunnel arrangement for case 2H (Liu et al., (2019))

Velocity values given at 120 points, located 0.02 m above the ground in the horizontal plane around the central building, were compared with the numerical simulation results.

3.2 Parametric study

A parametric study was performed to investigate wind flow around lift-up buildings in high-density urban environments. A total of 48 configurations were analyzed by varying core shape, lift-up height, surrounding building height, and two wind directions, as summarized in Tables 1 and 2 and shown in Figure 3. The model adopted an array-type urban layout with a central lift-up building surrounded by eight 20 m-wide square buildings, with surrounding heights adjusted accordingly.

Table 1: Parameters considered in the parametric study

Parameter	Values
Lift-up height	4 m, 8 m
Lift-up core shape	Square, Circular, Rounded
Wind direction	0°, 45°

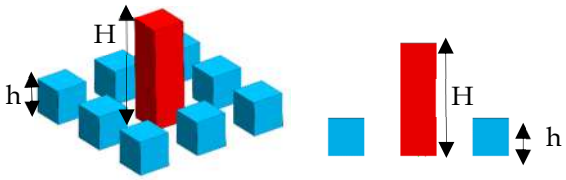

(a) (b)

Figure 3: Surrounding building arrangements in parametric study: (a) isometric view, (b) side view

Table 2: Surrounding building arrangement types

Configuration	Type 1	Type 2	Type 3	Type 4
h/H	0.0	$1/3$	$2/3$	1.0

The Eq. (1) gives the power-law wind profile representative of urban conditions, which was applied in the parametric study.

$$\frac{v_z}{5} = \left(\frac{z}{10}\right)^{0.36} \quad (1)$$

The parametric results clarify how geometric and contextual variations affect pedestrian-level wind conditions around lift-up buildings, providing a foundation for subsequent mitigation strategies.

3.3 Wind barrier effect study

Following the parametric study, wind barrier analysis was conducted for the worst-case discomfort scenarios. Vertical impermeable barriers of varying heights (Table 3) were placed upstream of the central lift-up building to assess their effectiveness as passive mitigation measures. CFD simulations evaluated changes in wind velocity and discomfort zones, aiming to identify optimal barrier heights without causing adverse secondary flow effects.

Table 3: Details wind barrier configurations considered

Configuration	Barrier height
WB1	2 m
WB2	4 m
WB3	8 m
WB4	12 m

4. Results and Discussion

4.1 Validation results

The graph in the Figure 4 gives the comparison of velocity ratios obtained from the experimental data and CFD simulation for the horizontal plane of z = 0.02 m.

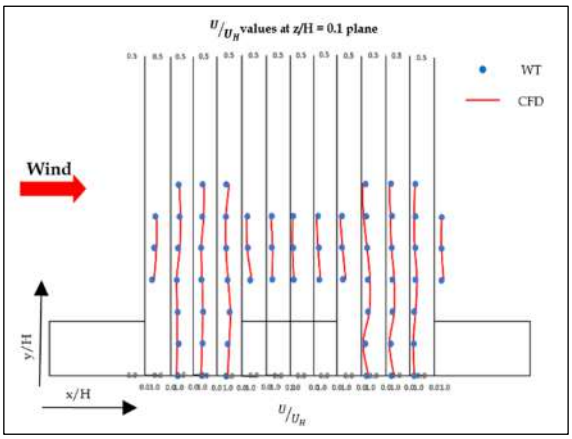

Figure 4: Comparison of velocity ratios obtained from CFD simulation and the given experimental data

The comparison produced an R^2 value of 0.8121, indicating strong agreement (81.21%) between experimental and CFD results and confirming acceptable model accuracy.

4.2 Results of parametric study

The parametric results showed significant variation in pedestrian-level wind velocity across configurations. Analysis of core shape, lift-up height, surrounding building height, and two wind directions identified key factors affecting wind comfort. Figure 5 illustrates the velocity distribution for the square lift-up configuration (4 m height) under 0° wind.

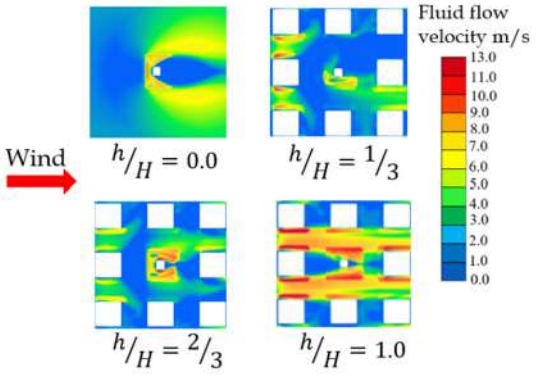

Figure 5: Simulation results at 2 m height for square shaped 4m lift-up core configuration

In the parametric study, the percentage of the area exceeding 8 m/s was calculated using Eq. (2) to quantify high-discomfort zones around the lift-up building.

$$\underset{area}{Uncomfortable} = \frac{A_{Total} - A_{v<8m/s}}{A_{Total}} \times 100\ \% \quad (2)$$

Figures 6 and 7 show the variation in uncomfortable wind area with the surrounding-to-central building height ratio for the 4 m and 8 m lift-up cases, respectively.

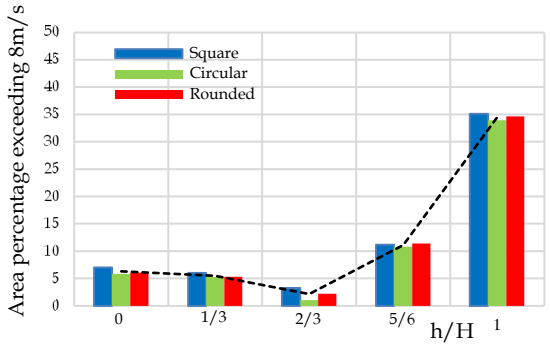

Figure 6: Comparison of uncomfortable area percentage variation with h/H for different lift-up core shapes with 4m lift-up height

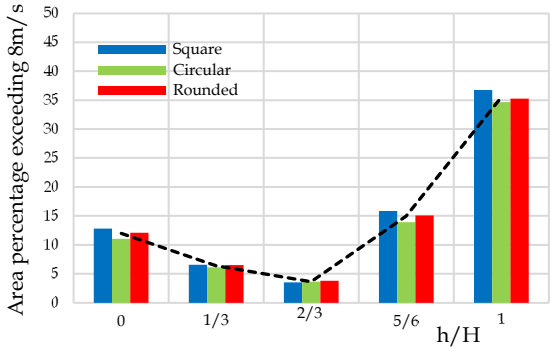

Figure 7: Comparison of uncomfortable area percentage variation with h/H for different lift-up core shapes with 8m lift-up height

Core shape variations produced minimal changes in pedestrian discomfort, remaining within 3% across comparable cases. Discomfort decreased as surrounding buildings reached two-thirds of the central height, acting as barriers that deflected and dissipated wind energy. However, when surrounding and central heights were equal, discomfort increased markedly due to wind tunneling and intensified downwash that accelerated pedestrian-level flow. Figure 8 supports this observation by showing the turbulent kinetic energy dissipation

rate for the square 4 m lift-up case, highlighting changes in wind energy behavior.

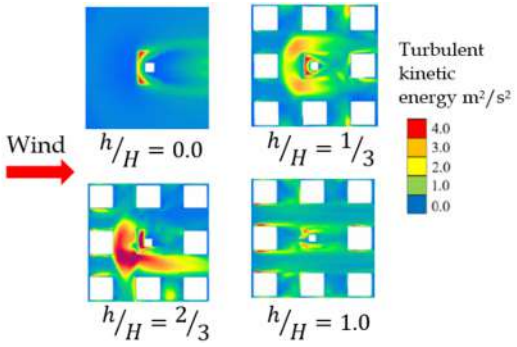

Figure 8: Turbulence kinetic energy at 2 m height for square shaped 4m lift-up core configuration

4.2 Results of wind barrier effect study

The parametric study identified the worst-case scenario for pedestrian wind comfort as the configuration with surrounding buildings at the same height as the central lift-up building under 0° wind direction.

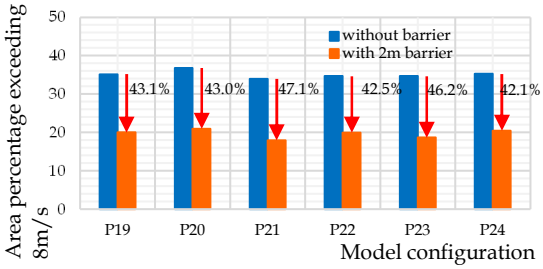

Figure 9: Effect of 2 m barrier

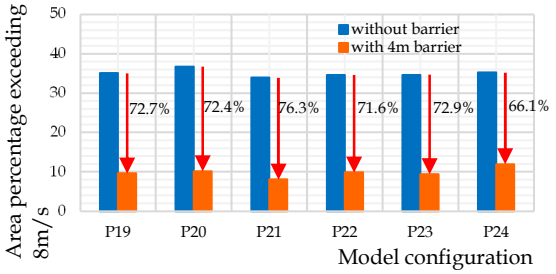

Figure 10: Effect of 4 m barrier

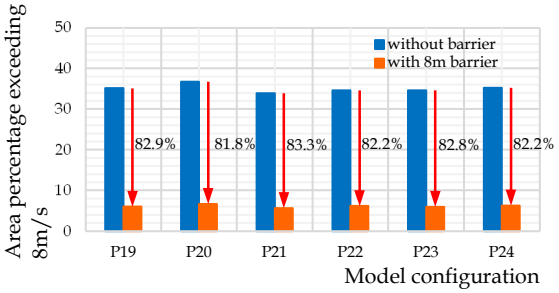

Figure 11: Effect of 8 m barrier

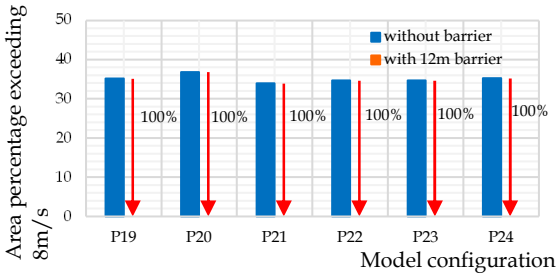

Figure 12: Effect of 12 m barrier

Figures 9, 10, 11 and 12 demonstrate that wind barriers effectively dissipate wind energy and enhance pedestrian comfort.

5. Conclusions

- When maintaining an optimal aspect ratio, lift-up core shape has minimal impact on pedestrian wind discomfort. Differences among square, circular, and rounded cores are marginal, with rounded and circular shapes exhibiting slight aerodynamic advantages.
- Increasing lift-up height from 4 m to 8 m increases discomfort zones by 2–3% due to stronger undercroft wind acceleration.
- Surrounding buildings up to 2/3rd the lift-up building height reduce discomfort effectively, keeping it below 5%, while equal-height surroundings significantly increase discomfort due to downwash and tunneling effects.
- Wind direction significantly affects pedestrian comfort. The 0° wind produced the largest discomfort zones, reaching up to 35% of the area when surrounding and lift-up building heights were equal. In contrast, 45° winds generated more diffuse flow patterns, reducing discomfort by approximately 20%.
- Wind barriers effectively reduce discomfort in the worst-case scenario. Barrier heights of 2 m, 4 m, and 8 m reduce discomfort by around 43%, 72%, and 82% respectively, with a 12 m barrier fully eliminating discomfort zones.

References

Du, Y., Mak, C.M. and Li, Y. (2018). 'Application of a multi-variable optimization method to determine lift-up design for optimum wind comfort' *Building and Environment*, 131, pp.242–254.

Liu, J., Zhang, X., Niu, J. and Tse, K.T. (2019). 'Pedestrian-level wind and gust around buildings with a 'lift-up' design: Assessment of influence from surrounding buildings by adopting LES' *Building Simulation*, 12(6), pp.1107–1118.

PERFORMANCE OF ECCENTRICALLY COMPRESSED STEEL BOX PIERS UNDER BI-DIRECTIONAL CYCLIC LOADS

Weerasekara, W. A.[1,*], Wijesuriya, A. W. L.[1], Jayasinghe, J. A. S. C.[1]

[1]Department of Civil Engineering, University of Peradeniya, 20404, Sri Lanka

* e19498@eng.pdn.ac.lk

1. Abstract

This study evaluates the seismic performance of steel box bridge piers subjected to eccentric axial loads and bidirectional cyclic loading. Using 96 Finite Element models in *ABAQUS*, key response parameters were analysed and compared with existing empirical models. A new equation set was proposed to better account for eccentricity effects. Results highlight that eccentric loading significantly reduces strength and ductility, emphasizing the need for updated seismic design approaches.

Keywords: Bidirectional cyclic loading, Eccentric axial loading, Empirical equations, Finite element analysis, Steel hollow piers

2. Introduction

Steel box piers in bridges are often subjected to eccentric axial loads and bidirectional seismic forces, making their behaviour under such conditions complex and less understood. Existing researches mainly focuses on unidirectional loading, with limited attention to the combined effects of eccentricity and bidirectional cyclic loading. This study addresses that gap by analysing Finite Element models to evaluate the impact of eccentricity on key performance indicators such as normalized peak strength (H_m/H_y), maximum ductility (δ_m / δ_y), and ductility at 95% peak strength (δ_{95} / δ_y). The findings aim to propose design equations and enhance seismic resilience of eccentrically loaded piers.

3. Literature Review

Previous research has examined the cyclic performance of stiffened steel hollow piers primarily under concentric axial and unidirectional lateral cyclic loading. Pioneering works by Suzuki and Usami (1995) and Usami *et al.* (2000) introduced empirical equations based on normalized peak strength and ductility ratios. These models served as the foundation for subsequent studies; however, they overlooked the complex behaviour induced by bidirectional seismic loads and axial eccentricity. Jenothan *et al.* (2024) later proposed an updated set of equations to account for bidirectional incremental cyclic loading (BICI), demonstrating improved accuracy for seismic applications. Figure 1 illustrates the BICI pattern applied in modern seismic simulations to replicate true earthquake-induced displacement histories.

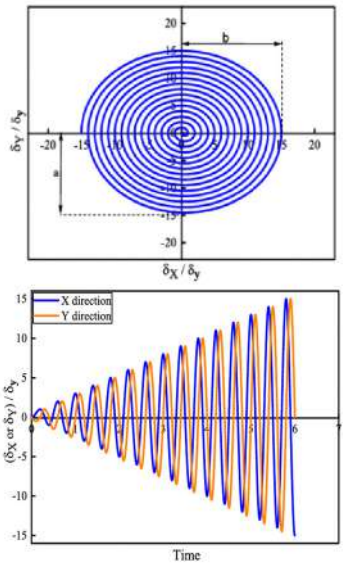

Figure 19: Bi-directional circular loading pattern (Jenothan *et al.*, 2024)

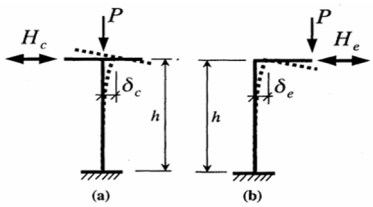

Figure 20: Steel bridge piers: (a) centrally loaded and (b) eccentrically loaded (Liu *et al.*, 2000)

Despite these advancements, the effect of eccentricity remains insufficiently addressed. Eccentric axial forces as shown in Figure 2 generate additional bending moments that affect both stress distribution and failure mechanisms. Increasing eccentricity ratios notably reduce normalized peak lateral strength and ductility

indices. This highlights the critical need for refined models that incorporate both bidirectional lateral and eccentric axial loading effects a gap this study addresses by proposing a new empirical equation set, calibrated through comprehensive Finite Element modelling.

4. Methodology

The overall methodology, illustrated in Figure 3, involves two main stages: numerical modeling and parametric analysis. A total of 96 Finite Element models were developed in *ABAQUS*, including cases with eccentricities of 0, 0.1, 0.2, and 0.3. After mesh convergence and validation under uni-directional and bi-directional loading, key response parameters ($H_m/H_y, \delta_m / \delta_y, \delta_{95} / \delta_y$) were extracted. These were compared with past empirical formulas from 1995 to 2023. Based on statistical deviations, the 2023 BICI model was selected and modified to account for eccentric effects, leading to a new proposed equation set.

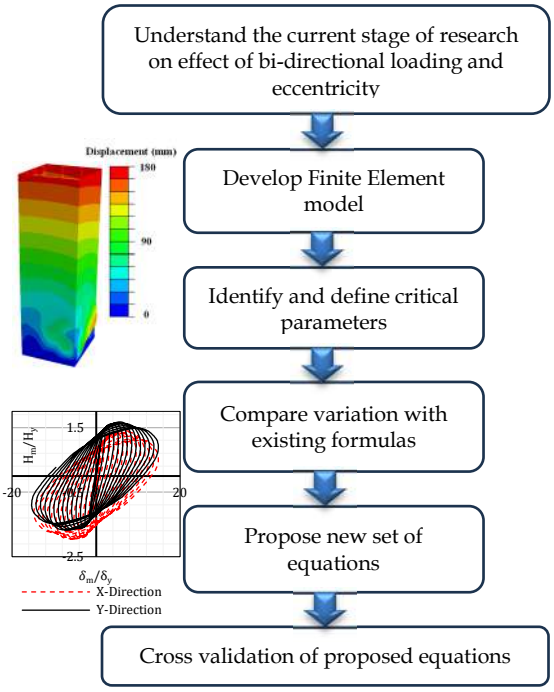

Figure 21: Overall methodology of the study

4.1 Numerical Modelling

Finite Element models of steel hollow box piers were developed in *ABAQUS* to simulate seismic loading. A mesh convergence study determined optimal mesh sizes of 15 mm (lower part up to 1st diaphragm) and 25 mm (upper part). The models were validated against published experimental results to ensure accurate cyclic behaviour simulation. Following validation, a total of 96 models were developed; 24 each for eccentricity ratios of 0, 0.1, 0.2, and 0.3. Bidirectional incremental cyclic loading was applied to all models as shown in Figure 4. Table 1 shows the material properties used for the models. From the resulting hysteretic and envelope curves, key response parameters; normalized peak lateral strength (H_m / Hy), maximum ductility (δ_m / δ_y), and 95% ductility (δ_{95}/δ_y), were extracted for comparison and further analysis.

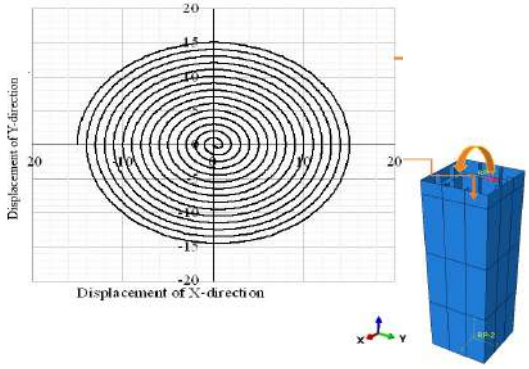

Figure 22: Applied loadings

Table 5: Material properties

Parameter	Value
Yield strength (σ_y)	314 MPa
Ultimate strength (σ_u)	593 MPa
Young's modulus (E)	2.06 × 105 MPa
Poisson's ratio (v)	0.3
E/E_{st}	30
$\varepsilon_{st}/\varepsilon_y$	7

4.2 Parametric Study

A parametric study involving developed Finite Element models was conducted to assess the seismic response of eccentrically compressed steel box piers under bidirectional loading. Models covered eccentricity ratios of 0 to 0.3 and varied key parameters such as width-to-thickness ratio (R_f), slenderness ($\bar{\lambda}$), axial load ratio (P/P_y), and stiffener slenderness ($\bar{\lambda_s}'$)). Critical response indicators; normalized strength, maximum ductility, and ductility at 95% strength were compared with empirical models from 1995–2023. Using statistical indices such as mean relative error, standard deviation and deviation within ±15%, the 2023 BICI equation set was found most compatible with bidirectional loading conditions. This set was selected for further modification to incorporate eccentricity effects, forming the basis of the proposed equations.

5. Results and Discussion

5.1 Validation Results

Validation is a crucial step in verifying the accuracy and reliability of the Finite Element model developed to simulate the seismic behaviour of eccentrically compressed steel box piers under bidirectional cyclic loading. The model was validated against experimental and numerical results from prior literature using three distinct loading scenarios. Key outputs such as hysteresis curves and envelope curves were used for comparison as shown in Figure 5.

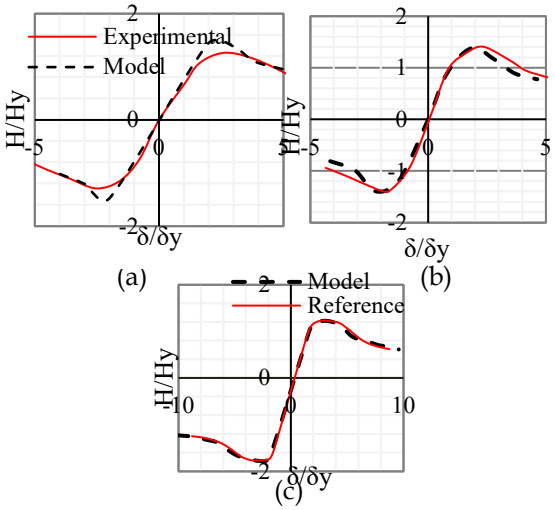

Figure 23: Validation results: (a) uni-directional, (b) bi-directional and (c) eccentric case

5.2 Numerical Analysis

A total of 96 Finite Element models were developed in *ABAQUS* to simulate eccentrically compressed steel box piers under bidirectional incremental cyclic loading (BICI). These models varied by eccentricity levels (e/h = 0.0, 0.1, 0.2, 0.3) and key geometric parameters including width-to-thickness ratio (Rf), slenderness ratio ($\bar{\lambda}$), and stiffener slenderness ($\lambda s'$). SM490 steel was modeled using a bilinear stress–strain curve. Hysteretic and envelope curves were generated to extract critical response indices: normalized peak lateral strength (H_m/H_y), maximum ductility (δ_m / δ_y), and ductility at 95% strength (δ_{95} / δ_y). The X-direction exhibited the weakest structural response, as the moment was applied about the Y-axis in all cases, and was therefore used as the basis for comparison. Figure 6 shows the failure modes of B7 model.

5.3 Statistical Analysis

Numerical results were benchmarked against empirical equations from 1995 to 2023, including the 2023 BICI model. Statistical measures such as mean relative error (MRE), standard deviation (SD), and percentage of results within ±15% deviation was used for validation. The 2023 BICI equation set provided the highest accuracy under bidirectional cyclic loading (Jenothan *et al.* 2024).

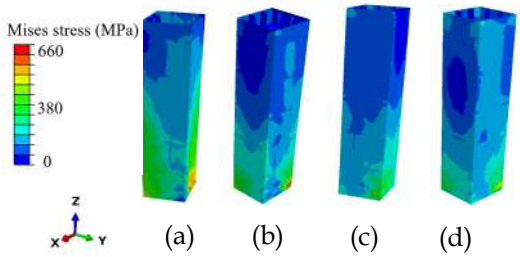

Figure 6: Failure Modes of B7: (a) zero-eccentricity (b) e/h=0.1, (c) e/h=0.2 and (c) e/h=0.3

5.4 Development of the new equation set

A new strength equation incorporating the moment-to-height ratio (M_0/h) was proposed to account for eccentric effects. The formulation was derived by modifying the original equation structure through regression analysis, specifically by adjusting the parameters a and b as presented in Eq. (1). δ_m / δ_y equation from 2023 BICI remained valid without further modification, confirming their conservative applicability under eccentric loading scenarios. For δ_{95}/δ_y, the new equation retains the original form from the 2023 BICI equation set, with the only modification being the exponent term, renamed as c, as shown in Eq. (2).

$$\frac{H_m}{H_y} = \frac{0.33}{\left[R_f\bar{\lambda}\,\bar{\lambda_s}'/((1+P/P_y)\right]^{0.35}} + 0.5 - \left(a\left(\frac{M_0}{h}\right)^b\right)\frac{1}{H_y} \quad (1)$$

$$\frac{\delta_{95}}{\delta_y} = \frac{0.95}{\left[R_f\sqrt{\bar{\lambda}}\,\bar{\lambda_s}'(1+P/P_y)\right]^c} + 0.325 \quad (2)$$

Eqs. (3) and (5) is the modified version of normalized peak lateral strength (H_m/H_y), and ductility at 95% strength (δ_{95} / δ_y) for BICI. No modifications needed for maximum ductility (δ_m / δ_y) since the existing equation as Eq. (4) underpredict the results the models are in safe region.

$$\frac{H_m}{H_y} = \frac{0.33}{\left[R_f\bar{\lambda}\,\bar{\lambda_s}'/((1+P/P_y)\right]^{0.35}} + 0.5 - \left(0.75\left(\frac{M_0}{h}\right)^{1.02}\right)\frac{1}{H_y} \quad (3)$$

$$\frac{\delta_m}{\delta_y} = \frac{7.96}{\left[R_f\sqrt{\bar{\lambda}}\,\bar{\lambda_s}'(1+P/P_y)\right]^{0.15}} - 8.1 \quad (4)$$

$$\frac{\delta_{95}}{\delta_y} = \frac{0.95}{\left[R_f\sqrt{\bar{\lambda}}\,\bar{\lambda_s}'(1+P/P_y)\right]^{0.5}} + 0.325 \quad (5)$$

Figure 7, Figure 8, and Figure 9 present a comparison of predicted versus numerical results for H_m/H_y, and δ_{95} / δ_y including both the 2023 BICI and newly proposed 2025 BICI equation sets, δ_m / δ_y for 2023 BICI equation as benchmarks for cross validated models (Jenothan *et al.* 2024). Each plot features a 45° reference line indicating perfect agreement and highlights data points within the applicable range of both equations under eccentric loading.

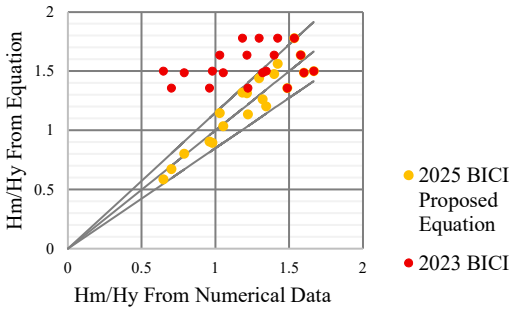

Figure 7: H_m/H_y numerical results vs old and new equation value for cross validation

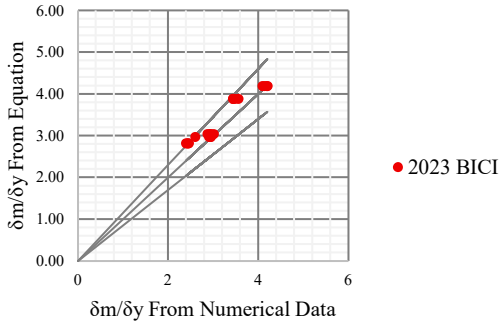

Figure 8: $\boldsymbol{\delta_m/\delta_y}$ numerical results vs equation value for cross validation

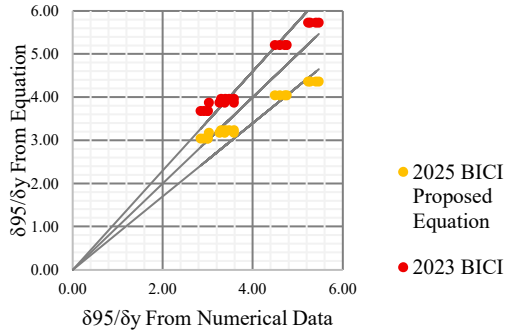

Figure 9: $\boldsymbol{\delta_{95}/\delta_y}$ numerical results vs old and new equation value for cross validation

Conclusions

- Eccentricity reduced seismic performance, causing early local buckling and asymmetry.
- The weakest performance consistently occurred along the axis of eccentric moment, highlighting the importance of accounting for directional effects in design.
- New empirical equations for H_m/H_y and δ_{95} / δ_y under BICI loading showed strong agreement with numerical results and improved accuracy over existing models.
- No modification was needed for the existing equation Eq. (2.28) (Jenothan et al. 2024), predicting δ_m / δ_y , as it already the design values are conservative for safe performance-based design under the range of parameters investigated.
- Statistical evaluation based on the cross validated results (mean error, standard deviation, and ±15% deviation criteria) confirmed that over 90% of predictions fell within acceptable accuracy limits with mean relative error 0.047 and standard deviation 0.03 for H_m/H_y and over 90% of predictions fell within acceptable accuracy limits with mean relative error 0.380 and standard deviation 0.03 for δ_{95} / δ_y, particularly for models within $0.3 \leq R_f \leq 0.5$, $0.25 \leq \bar{\lambda} \leq 0.5$, $0.0 \leq P/P_y \leq 0.5$, $3 \leq \gamma/\gamma^* \leq 0.3$ and $0.0 \leq e/h \leq 0.3$.

References

Jenothan, M. et al. (2024). 'Performance Evaluation of Steel Hollow Box Piers under Bidirectional Lateral Cyclic Loading to Enhance the Existing Seismic Verification Framework', *Journal of Constructional Steel Research*, 212, p.108246. doi: 10.1016/j.jcsr.2023.108246.

Liu, Q., Usami, T. and Kasai, A. (2000). 'Inelastic Seismic Response Analysis of Eccentrically Loaded Steel Bridge Piers', *Structural Engineering/Earthquake Engineering*, 17(2), pp.149–162. doi: 10.2208/jscej.2000.654_25.

Suzuki, M. and Usami, T. (1995). 'Estimating Formulas of Strength and Deformation Capacity of Steel Bridge Pier Model Under Cyclic Loading', *Doboku Gakkai Ronbunshu*, 1995(519), pp.115–125. doi: 10.2208/jscej.1995.519_115.

Usami, T., Gao, S. and Ge, H. (2000). 'Stiffened Steel Box Columns Part 2: Ductility Evaluation', *Earthquake Engineering and Structural Dynamics*, 29(11), pp.1707–1722. doi: 10.1002/10969845(200011)29:11<1707:AID-EQE990>3.0.CO;2-7.

COMPUTER VISION-BASED DETECTION AND QUANTIFICATION OF CRACKS IN CONCRETE BEAMS

Ariyaratne, H. M. P. B.[1,*], Samarasekara, U. G. U. P.[1], Ekanayake E. M. R.[1], Jayasinghe, J. A. S. C.[1], Jayasinghe, U.[1] and Dhammika, A. J.[1]

[1]Faculty of Engineering, University of Peradeniya, Peradeniya, 20400, Sri Lanka

[*] e19027@eng.pdn.ac.lk

Abstract

This study presents a vision-based framework for automated crack detection, quantification, and classification in reinforced concrete beams, addressing the limitations of manual inspection. The process begins with beam support classification using a YOLO-based model, followed by semantic segmentation for beam localization and cropping. Crack presence is identified using optimized CNN classifiers—AlexNet, VGG-16, and DenseNet-121—selected for their performance and efficiency. Crack segmentation is performed using a hybrid model combining the Segment Anything Model (SAM) and YOLO, enabling precise extraction of parameters such as width, length, location, orientation, density, and fractal dimension. Stereo vision techniques convert pixel-level measurements to millimetres, ensuring real-world scalability. Cracks are further categorized by propagation mechanisms (shear, flexure, tension, etc.) using geometric and contextual cues. The framework achieved 94.5% accuracy in support classification, 91.1% beam segmentation accuracy, and 98.0% crack detection accuracy. Measurement errors were below 5.2% for length and orientation, and 12.5% for width. This portable and robust system offers a scalable solution for structural health monitoring.

Keywords: concrete beams, computer vision, convolutional neural network, crack monitoring, structural health monitoring

1. Introduction

Concrete structures, though durable, are prone to long-term deterioration such as cracking, which compromise safety if undetected. While sensor-based SHM systems exist, their complexity and sensitivity limit practicality (Bhowmick et al., 2020). Manual inspection remains widely used but suffers from subjectivity and inaccessibility. Vision-based SHM has emerged as a scalable alternative, with techniques like region-based classification and semantic segmentation enabling accurate crack detection and measurement (Rao et al., 2020). This research addresses that gap by proposing an integrated computer vision-based SHM framework for detection, quantification, and cause-based crack classification.

2. Literature review

Recent advancements in Structural Health Monitoring (SHM) have shifted from manual inspections to sensor-based and computer vision-driven methods. Traditional and sensor-based techniques often face issues of scalability, complexity, and reduced accuracy. In contrast, image-based SHM offers automation and precision. Deep learning models like YOLO, VGG-16, and DenseNet support real-time crack detection, while segmentation networks such as U-Net and FCNs provide detailed pixel-level analysis (Egodawela et al., 2024). Stereo vision further enhances accuracy through 3D mapping and real-world scaling (Hamad et al., 2024). This study proposes a unified, field-ready framework that integrates detection, quantification, and classification.

3. Methodology

Figure 1 shows the general steps of the methodology of this study.

3.1 Data acquisition

A large, diverse dataset was compiled, including 60,000 crack and 100,000 non-crack images from public sources, along with annotated beam images for segmentation and support classification. This multi-source approach ensured balanced training and improved the generalizability of the proposed framework across varied real-world conditions.

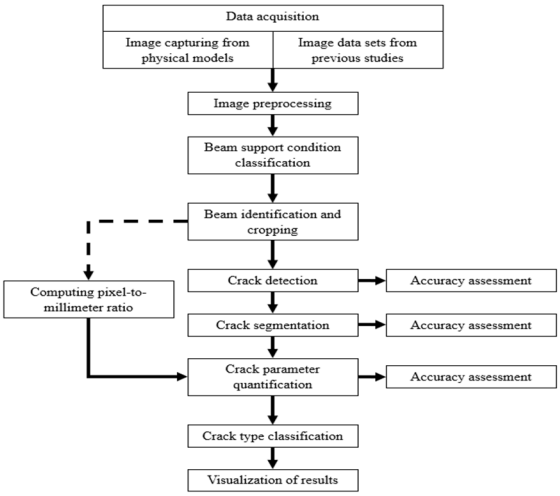

Figure 1: Flow chart of the methodology

3.2 Data preprocessing

Preprocessing involved deblurring, and denoising to enhance image quality for crack detection and segmentation. Checkerboard-based calibration enabled accurate stereo alignment for metric conversions. MPRNet was used for deblurring, restoring fine crack details through attention-based refinement. Wavelet transform-based denoising suppressed high-frequency noise while preserving crack features.

3.3 Beam support condition classification

A YOLOv8-based deep learning model was developed to classify beam support conditions—simply supported, fixed, continuous, and cantilever based on visual cues. The model is trained on a curated dataset of 300 annotated images with preprocessing and augmentation, including low-light and partially occluded images. This classification supports failure mode identification within the framework.

3.4 Beam identification and cropping

To improve crack detection accuracy, a YOLOv8-based semantic segmentation model was used to isolate concrete beams from complex backgrounds. It is trained on 200 annotated images with binary masks, enabling accurate region cropping and pixel-to-millimeter scaling by extracting the beam corner points in stereo vision.

3.5 Pixel to millimetre ratio computation

A stereo vision-based method was employed to convert pixel measurements of cracks into real-world millimetres. Using a fixed baseline setup with calibrated cameras and beam corner matching via epipolar geometry, disparity values were computed. This allowed for accurate pixel-to-millimetre ratio calculation without physical scale markers.

3.6 Crack detection

Crack detection was achieved using deep learning classifiers—DenseNet-121, VGG-16, and AlexNet—trained on 8,000 balanced and augmented images. These 3 models were chosen based on Rao et al., (2020) where VGG-16 delivered the highest accuracy (98.05%), while AlexNet offered the fastest inference time and DenseNet-121 had balanced accuracy and inference time.

3.7 Crack segmentation

Two segmentation methods—SAM and YOLOv8 were assessed for pixel-level crack segmentation. These models were chosen based on literature review while according to Egodawela et al., (2024) SAM with edge-based preprocessing achieved the highest accuracy (IoU: 0.851, F1: 0.728), while YOLOv8, enhanced with patch-wise refinement, provided the fastest inference for real-time use.

3.8 Crack parameter quantification

The framework quantified key crack parameters—length, width, orientation, starting point, fractal dimension, and density using stereo vision-based pixel-to-millimetre conversion. Methods such as contour analysis, distance transform, and box-counting were applied to derive physical measurements.

3.9 Crack type classification

A rule-based system was employed to classify crack types into failure modes—flexure, shear, torsion, tension, and crushing based on crack geometry, beam support type, initiation point, and surface location. This interpretable approach, grounded in structural mechanics, enhances diagnostic reliability.

3.10 Visualization of results

The framework concludes with a detailed visual output that overlays crack detections on the segmented beam image, annotating key attributes such as length, width, orientation, and failure type. This comprehensive visualization supports diagnostic accuracy and aids decision-making in structural health monitoring.

4. Results and discussion

The proposed stereo vision-based SHM framework was evaluated across key stages, including beam classification, segmentation, crack detection, and parameter quantification. High classification accuracy and strong IoU and F1-scores confirmed reliable performance, while quantification errors remained minimal, closely matching actual measurements across crack length, width, orientation, and position.

4.1 Beam support condition classification

The YOLOv8-based beam support classification model accurately identified four structural boundary types—simply supported, cantilever, continuous, and fixed based on image data, achieving a validation accuracy of 94.50%. Despite variations in lighting, scale, and background, the model performed consistently, making it highly suitable for automated structural health monitoring applications. Training metrics showed stable convergence without overfitting, confirming the model's robustness and value as a preprocessing step to improve the contextual relevance of subsequent crack analysis. Figure 2 shows results of beam support condition classification.

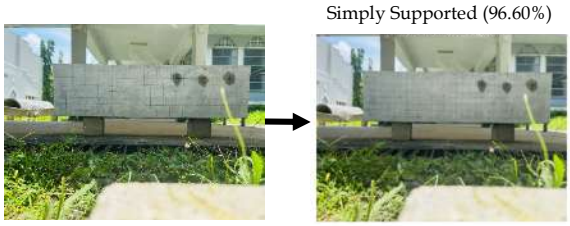

Figure 2: Results of identification and segmentation of the beam

Figure 3 shows the model performance via training and validation accuracy curves for beam support condition classification

Figure 3: Training and validation accuracy curves for beam support condition classification model

4.2 Beam identification

The semantic segmentation-based beam identification module accurately isolated reinforced concrete beams and extracted corner coordinates for spatial calibration. It achieved an IoU of 0.626, F1-score of 0.77, precision of 0.911, and recall of 0.667, with mAP near 0.70. Despite occasional under-segmentation, the model performed robustly and eliminated the need for manual localization, enabling fully automated input preparation for stereo-based crack quantification in real-world structural health monitoring scenarios. Figure 4 shows the results of identification and segmentation of the beam. Figure 5 shows the model performance of beam segmentation.

Figure 4: Results of identification and segmentation of the beam (A – (737, 609), B – (3792, 628), C – (737, 1412), D – (3817, 1474))

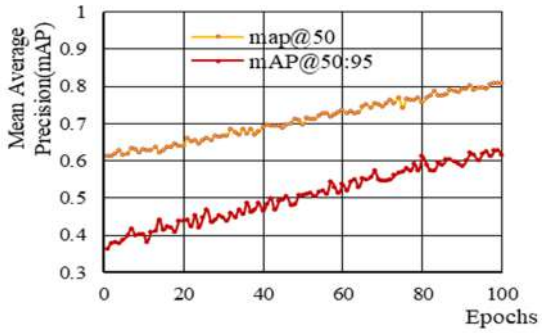

Figure 5: mAP@50 and mAP@50:95 curves of segmentation model of the beam

4.3 Crack detection

The crack detection model, implemented as a binary classifier, accurately identified surface cracks in concrete beams while filtering out non-crack anomalies like spalling. Among the evaluated CNN architectures, DenseNet-121 and VGG-16 both achieved 98.00% classification accuracy, with VGG-16 offering superior inference speed (0.272s) compared to DenseNet-121 (2.993s), making it preferable for real-time use. AlexNet performed slightly lower at 96.00% accuracy but remained efficient (0.513s). All models exhibited stable learning with minimal overfitting, confirming their robustness across variable lighting and surface textures.

4.4 Crack segmentation

The crack segmentation model achieved effective pixel-level localization, with an F1 score of 0.6922, IoU of 0.5293, and pixel-wise accuracy of 99.32%. Visually, predicted masks closely matched

ground truths, accurately capturing crack orientation and geometry. Despite challenges in segmenting fine or fragmented cracks, the segmentation quality was sufficient for reliable crack dimensioning in SHM applications. Figure 6 shows the crack segmentation results.

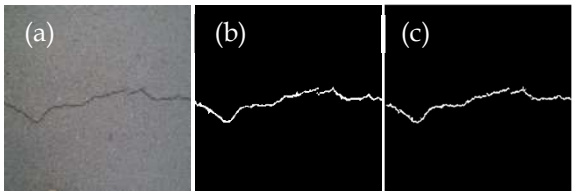

Figure 6: Crack segmentation results (a) original crack (b) Ground truth image (c) Predicted crack image

4.5 Parameter quantification

Using stereo image pairs from a fixed baseline mobile setup, the framework accurately converted pixel-level crack data into real-world dimensions. Four parameters—crack length, width, orientation, and starting point were extracted. Table 1 shows the maximum error percentage for each parameter quantified.

Table 1: Maximum error percentage of quantified parameters

Parameter	Maximum Error Percentage (%)
Crack length	4.41
Crack width	12.5
Crack starting point	5.11
Crack orientation	2.07

Crack parameter measurement results remained field-acceptable. Beam dimensions derived from stereo data had maximum error percentage of 2.73%, validating the system's spatial accuracy and utility for real-world SHM applications.

4.6 Discussion

The proposed framework introduces a unified, stereo vision-based system for automated beam classification, segmentation, crack detection, and parameter quantification. It improves upon prior studies by using disparity-based pixel-to-millimeter conversion with a smartphone stereo setup, eliminating the need for manual scaling. Comparative results show superior or comparable accuracy, particularly in crack detection and measurement. Key novelties include expanded support classification categories and context-aware crack failure classification. The system's modular, field-adaptable design supports real-world SHM applications, though segmentation accuracy could benefit from higher-resolution inputs and advanced model architectures for enhanced performance.

5. Conclusions

This research successfully delivers a scalable and practical solution for non-invasive structural health monitoring of reinforced concrete beams. It achieves high accuracy across tasks such as beam classification (94.50%), segmentation (IoU = 0.63), and crack detection (98.00%), while also enabling millimeter-scale quantification of crack parameters using stereo vision. The novel integration of disparity-based length estimation enables accurate scaling and localization without physical markers. Maximum errors in key measurements such as 4.41% for crack length and 2.73% for beam dimensions fall within acceptable engineering tolerances. With portability, the framework is well-positioned for deployment in mobile, UAV, and post-disaster applications, advancing the field of automated concrete defect assessment.

References

Bhowmick, S., Nagarajaiah, S. and Veeraraghavan, A. (2020). 'Vision and Deep Learning-Based Algorithms to Detect and Quantify Cracks on Concrete Surfaces from UAV Videos', *Sensors*, 20, p.6299. doi: 10.3390/s20216299.

Egodawela, S., Khodadadian Gostar, A., Buddika, H.A.D.S., Dammika, A.J., Harischandra, N., Navaratnam, S. and Mahmoodian, M. (2024). 'A Deep Learning Approach for Surface Crack Classification and Segmentation in Unmanned Aerial Vehicle Assisted Infrastructure Inspections', *Sensors*, 24, p.1936. doi: 10.3390/s24061936.

Hamad, L., Khan, M.A. and Mohamed, A. (2024). 'Object Depth and Size Estimation Using Stereo-Vision and Integration With SLAM', *IEEE Sensors Letters*, 8, pp.1–4. doi: 10.1109/lsens.2024.3367956.

Rao, A.S., Nguyen, T., Palaniswami, M. and Ngo, T. (2020). 'Vision-based Automated Crack Detection Using Convolutional Neural Networks for Condition Assessment of Infrastructure', *Structural Health Monitoring*, 20, pp.2124–2142. doi: 10.1177/1475921720965445.

INVESTIGATING THE EFFECTS OF NOTCHES AND HOLES IN THE PERFORMANCE OF TIMBER GIRDERS

Ranasinghe V.A.K.S.P.[1], Azhar H.M.[1], N.M.S.H. Bandara[1, *]

[1]Department of Civil Engineering, Faculty of Engineering, University of Peradeniya, Sri Lanka

[*] sahan@eng.pdn.ac.lk

Abstract

This study investigates the structural performance of timber girders containing notches and holes, which are often introduced for service integration and construction convenience. Such discontinuities can significantly reduce load-bearing capacity due to stress concentration and anisotropic behaviour of timber. Experimental three-point bending tests were conducted on laminated veneer lumber (LVL) girders with varying notch depths and hole geometries. The observed failure modes included shear and tensile cracking, with stepped notches showing the poorest performance. Finite element models using ABAQUS and Hill's anisotropic plasticity theory were developed and validated against the test data. A parametric study demonstrated that tapered notches and filleted holes reduce stress concentration and enhance load capacity. The findings show that current design standards may be overly conservative or lack precision in addressing notch and hole effects. Recommendations are made for more optimized and realistic design practices, improving the safe application of timber girders in modern construction.

Keywords: Notches, Holes, Hills Criteria, Timber girder

1. Introduction

Timber has been a prominent construction material for centuries due to its favourable strength-to-weight ratio, sustainability, and visual appeal. In modern construction, timber girders are often modified with notches and holes to accommodate utilities and structural connections. While these modifications serve functional purposes, they introduce stress concentrations that can significantly affect structural performance. The anisotropic nature of timber further complicates the analysis of such discontinuities. This study aims to investigate the effects of notches and holes on the strength and behaviour of timber girders through experimental testing and finite element modelling, ultimately guiding improved design practices.

2. Literature review

2.1 Introduction

Navaratnam et al., (2021) provides a comprehensive understanding of timber's structural behaviour which is essential for safe and efficient design, especially when modified with notches or holes. Previous research highlights the anisotropic nature of timber, the mechanical impact of discontinuities, and the limitations of existing design codes (Porteous and Kermani, 2008; Linville, 2012). This literature review explores the properties of timber and engineered wood products, the influence of notches and holes on structural performance, failure mechanisms, and the effectiveness of numerical and experimental methods used in past studies.

2.2 Background

Timber has been used as a construction material since ancient times and still being used today. Timber has natural imperfections such as cracks splits and decays. Timber also has anisotropic behaviour which means its material properties vary from the orientation. Timber properties can be aligned with the grain direction.

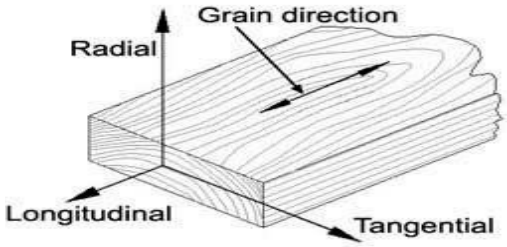

Figure 24: Timber anisotropy

This Grain direction is a critical property when designing. Parallel to the grain is the preferred load caring direction. Radial Direction has very low strength compared to parallel direction

2.3 Holes and Notches

Holes and notches are section that are added to the timber girders for mostly utility accommodation and aesthetically good seating between beams and columns. These Holes and notches add a certain complication to the design and create stress concentrations.

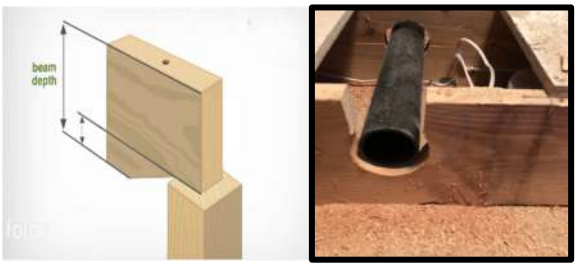

Figure 25: Holes and notches in timber girders

2.4 Factors that affect Girder Performance

Factors such as the notch depth, notch angle, notch type, hole size, hole position and hole geometry affect the timber girder very differently and very significantly. Many sections of these are studied under the parametric study.

3. Methodology

3.1 Understanding Anisotropic imperfections

The process begins with a detailed study of timber as a structural material, focusing on its use in modern construction, engineered wood products, and its mechanical behaviour. Emphasis is placed on timber's anisotropic characteristics and the impact of natural imperfections such as knots, cracks, and moisture sensitivity. Timber's orthotropic nature is analysed in terms of material directions (longitudinal, radial, tangential). The study identifies how these directional properties affect stress response, especially under flexural and shear loading when discontinuities like notches and holes are present.

3.2 Selection of Failure Criteria

To define the failure mode and damage factor under load for timber girders we needed a failure criterion. To accurately simulate timber behaviour under load, Hill's anisotropic yield criterion is selected. This criterion enables capturing direction-dependent stress-strain relationships, necessary for modelling timber's failure behaviour in three dimensions.

3.3 Development of FEM and Model Validation

A numerical model is developed in ABAQUS to simulate the structural performance of timber girders with different notch and hole configurations. The model incorporates elastic-plastic behaviour, material anisotropy, and boundary conditions based on experimental setups. The FEM model is validated using experimental data obtained from three-point bending tests of timber specimens with varying notch depths. The validation compares load-deflection curves, failure modes, and stress distributions to ensure the model's accuracy.

3.4 Parametric Study

A series of simulations is performed to assess the effect of different notch angles, depths, hole sizes, and positions on timber girder performance. Both rectangular and circular cross-sections are examined to evaluate variation in structural response. Based on parametric outcomes, design guidelines are proposed. These include recommendations on optimal notch shapes, safe hole placements, and suitable cross-sectional geometries. The study also evaluates current design standards, identifying Eurocode 5 as the most reliable.

4. Results and Discussion

The Model was validated for All 4 notch variations using the experimental results of Navaratnam et al., (2021).

4.1 Material Properties

Table 1: Material Properties of Timber

Material property	Unit	Value
Density	Kg/m^3	1060
Young's modulus X Direction	MPa	1093
Young's Modulus Y Direction	MPa	1655
Young's modulus Z Direction	MPa	16107
Poisson's Ratio XY		0.48
Poisson's Ratio YZ		0.047

Poisson's Ratio XZ		0.045
Shear modulus XY	MPa	630
Shear modulus YZ	MPa	1148
Shear modulus XZ	MPa	609
$\Sigma_{c,90}$	MPa	10.9
F		0.75
G		0.15
H		0.25
L = M		1.19
N		1.24
Friction Coefficient		0.6

Table 2: Plastics Stress Strain Variation

Plastic Stress	Plastic Strain
11.43	0.004
11.4	0.0045
11.34	0.0046
11.30	0.00466
6.8	0.004668
4.8	0.00469
3.4	0.0048

Table 3: Potential Rolling Values

Potential R value	Value
R11	8.85
R22	2.8
R33	2.7
R12	2.8
R13	2.8
R23	2.63

4.2 Validation Results

For the Specimens we have selected to carry out validation for all 4 Models.

Table 4: Experimental Sample configuration

Beam	Specimens	Width (m)	Depth (m)	Notch Depth (mm)	Notch Angle
A	5	150	150	0	0
B	5	150	150	15	1:4
C	5	150	150	22.5	1:4
D	5	150	150	45	1:4

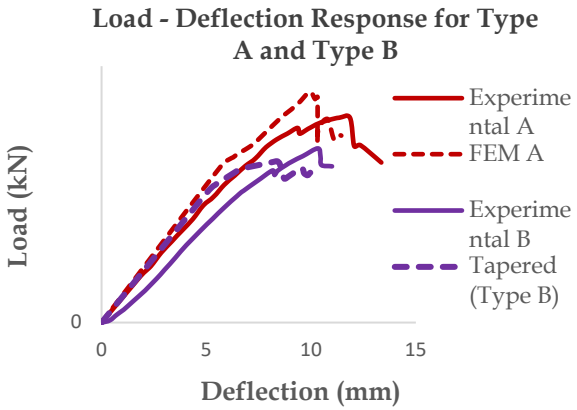

Figure 3: Validation Results of Type A and Type B beams

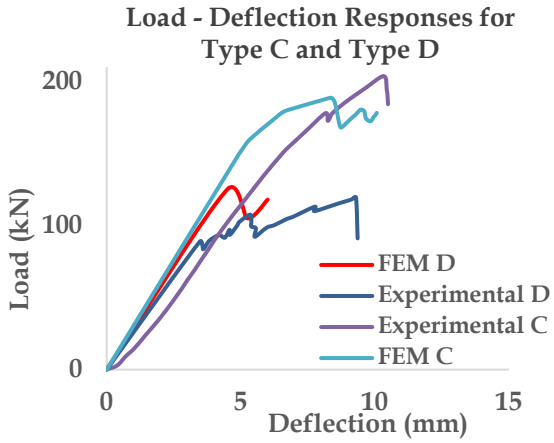

Figure 4: Validation Results of Type C and D Models

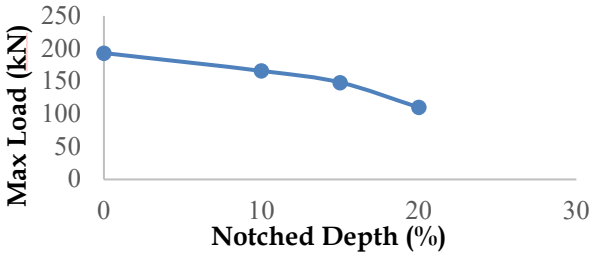

Figure 5: Load Variation with Notch depth

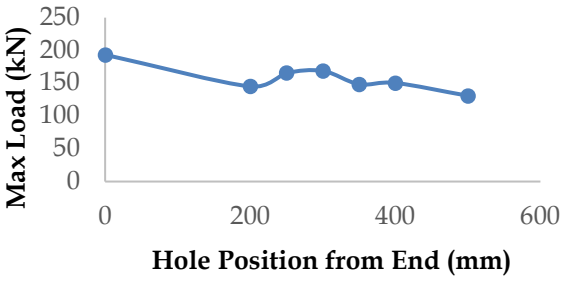

Figure 6: Max Load Vs Hole Position

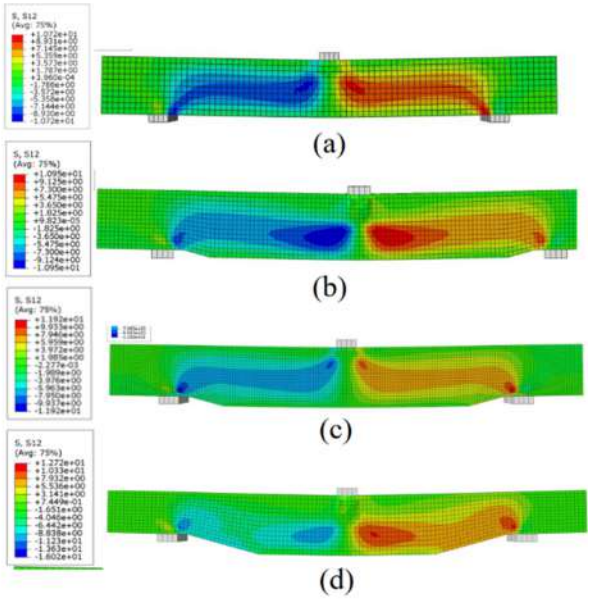

Figure 7: Shear Stress (S12) and Failure modes of the timber specimens under three-point bending: (a) Type A (b); Type B (c); Type C; and (d) Type D

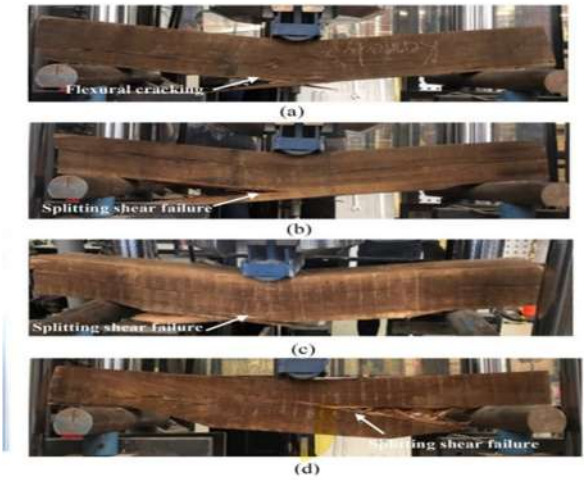

Figure 8: Experimental Setup Failure Results

5. Conclusions

- The finite element models developed in ABAQUS using Hill's anisotropic yield criterion showed strong agreement with experimental load-deflection behavior and failure modes, confirming model accuracy.
- Notch geometry plays a critical role—rounded or smooth notches performed significantly better than stepped notches. Curved profiles converted tensile stress to compressive along the grain, increasing strength by 12% and ductility by 20%.
- Tapered notches with smooth edges (150 mm radius) offered the best balance of strength (195 kN) and ductility, minimizing stress concentrations. Stepped notches showed higher peak loads (203 kN) but failed abruptly, possibly due to coarse meshing (5 mm) or lack of damage modeling.
- Small fillets (8 mm) improved stepped notch performance but require further validation due to simulation instability.
- Hole position had more influence on girder performance than hole size in small-holed specimens.
- As notch depth increases, failure mode shifts from flexural to shear.

References

European Committee for Standardization (2004) *EN 1995-1-1: Eurocode 5: Design of timber structures – Part 1-1: General – Common rules and rules for buildings*.

Linville, J.D. (ed.) (2012) *Timber construction manual*. 6th edn. Hoboken: John Wiley & Sons.

Navaratnam, S., Herath, N., Lokuge, W., Thamboo, J. and Poologanathan, K. (2021) 'Performance of timber girders with end-notch: Experimental and numerical investigation', *Structures*, 29, pp.730–740.

Porteous, J. and Kermani, A. (2008) *Structural timber design to Eurocode*. Chichester: John Wiley & Sons.

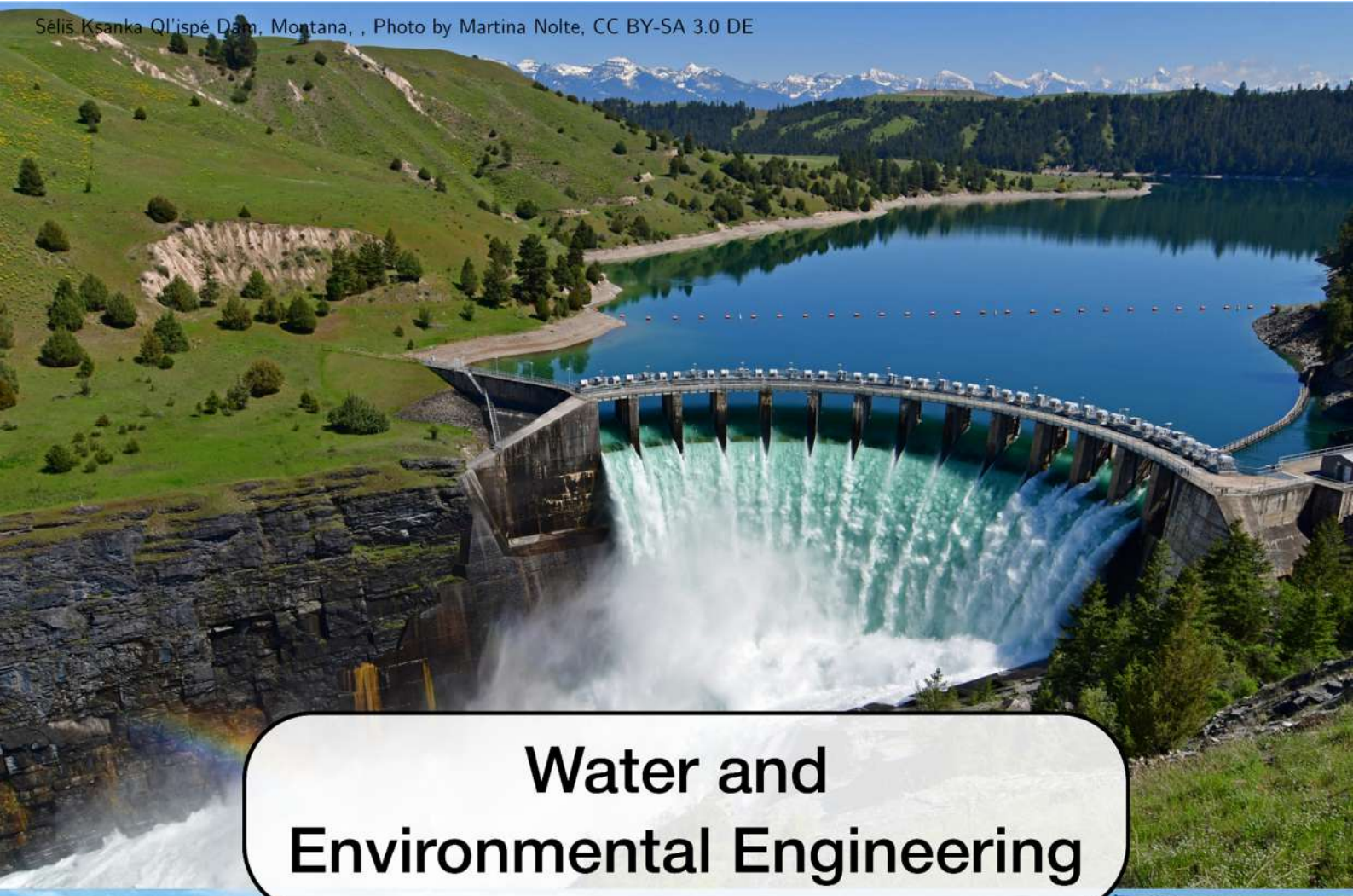

Water and Environmental Engineering

COMPARATIVE EVALUATION OF CONVENTIONAL AND MACHINE LEARNING MODELS FOR STREAMFLOW SIMULATION IN A TROPICAL SRILANKAN RIVER BASIN

Rathnayake R.A.V.D.[1], Sampath M.A.A.[1], De Silva M.M.G.T.[1,*]

[1]Department of Civil Engineering, Faculty of Engineering, University of Peradeniya, Sri Lanka

[*] gouri@eng.pdn.ac.lk

Abstract

Rainfall-runoff modelling is an important area of study in hydrological engineering with conventional techniques and emerging machine learning approaches. This study aims to bridge that gap by evaluating and comparing HEC-HMS, Machine Learning (ML) models, and a hybrid HEC-HMS-ML model in simulating streamflow at the Hanwella gauging station in the Upper Kelani River Basin. Using data from 1990 to 2024, the analysis focuses on streamflow simulation using performance metrics including Nash-Sutcliffe Efficiency (NSE), Normalized Root Mean Squared Error (nRMSE), Coefficient of Determination (R^2), and Percent Bias (PBIAS). Three machine learning models - Artificial Neural Network (ANN), Least Squares Boosting (LSBoost), and Random Forest were evaluated. The research highlights the hybrid model that combines HEC-HMS and ML model, demonstrating that the application of a hybrid model offers superior performance compared to physical models, delivering accurate results through a more efficient modelling process. It offers critical insights into the reliability of hybrid approaches for streamflow simulation, contributing to a detailed understanding of hydrologic modelling in the Upper Kelani River Basin.

Keywords: Streamflow simulation, HEC-HMS, Machine Learning, Hybrid model, Kelani river basin

1. Introduction

This research evaluates the accuracy of different streamflow simulation techniques, including conventional methods, machine learning models, and hybrid approaches, addressing a gap in the literature where comparative analyses among these methods remain limited. It demonstrates that traditional physically based models like HEC-HMS require precise calibration and high-quality input data, whereas machine learning models can learn patterns directly from historical data, offering greater flexibility and adaptability.

1.1 Aim and Objectives

The aim of this research is to investigate the most reliable method for streamflow estimations among conventional method (HEC HMS), machine learning models and Hybrid approaches for upper Kelani river basin. To achieve this aim, the study is guided by two specific objectives as, to develop conventional model (HEC HMS), Machine learning models and hybrid model, and to compare the results to select best fitting model.

1.2 Study Area

The Kelani River originates from the Sri Pada mountain range in the central hills and flows westward, passing through the districts of Nuwara Eliya, Ratnapura, Kegalle, Gampaha, and Colombo, the country's commercial capital. As the second largest river by discharge and the fourth longest river in Sri Lanka, with a total length of 145 km. The basin covers approximately 2,230 km² and is located between latitudes 6°47′–7°05′ N and longitudes 79°53′–80°13′ E.

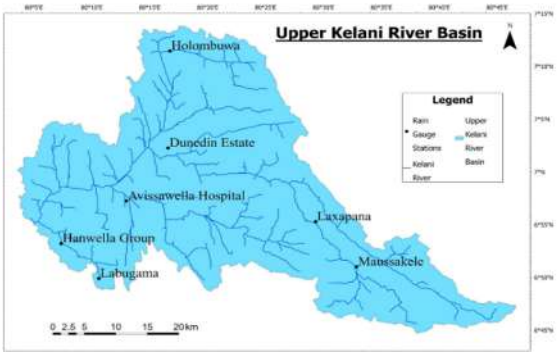

Figure 1: Selected rainfall gauging stations of the Upper Kelani River basin.

Land use within the basin includes rubber plantations, tea plantations, forests, and homesteads. Figure 1 shows the distribution of selected rainfall gauging stations of the Upper Kelani River basin.

2. Literature review

Streamflow modelling has progressed from empirical to conceptual and physically based models. While empirical models are simple and cost-effective, they lack accuracy. Conceptual models like HEC-HMS offer a balance between realism and usability (De Silva et al., 2014; Gunathilake et al., 2021; Reddy et al., 2023), whereas physically based models provide higher accuracy but demand extensive data and computation (Deulkar et al., 2024). Machine Learning models such as FFBPNN, LSBoost, and RF effectively capture nonlinear rainfall-runoff relationships without physical assumptions (Kedam et al., 2024). Hybrid approaches combining HEC-HMS with ML improve simulation performance by merging physical insights with data-driven learning (Mugume et al., 2024; Asaad et al., 2022).

Both conventional and ML models are commonly evaluated using statistical metrics such as the Coefficient of Determination (R^2), Nash–Sutcliffe Efficiency (NSE), Percent Bias (PBIAS), and Normalized Root Mean Squared Error (nRMSE). (Mugume et al., 2024).

3. Methodology

3.1 Workflow

The workflow diagram of this study is illustrated in Figure 2.

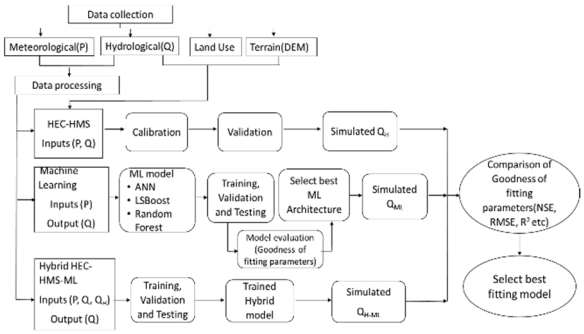

Figure 2: Workflow diagram

3.2 Data collection

Daily rainfall data from seven stations (Laxapana, Maussakele, Awissawella Hospital, Labugama, Dunedin, Hanwella Group, and Holombuwa) and daily discharge data at Hanwella were obtained from the Department of Meteorology and the Irrigation Department, respectively, for a 35-year period.

3.3 Data processing

Collected rainfall data was processed with three main steps: (1) filling missing data for less than 10% of missing records using the inverse distance weighted method, (2) checking for data consistency using the double mass curve technique, and (3) distributing data using the Thiessen polygon method. Figure 3 shows the Thiessen polygon map of the basin.

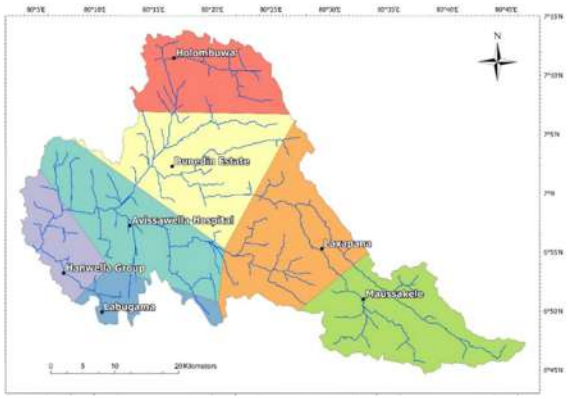

Figure 3: Thiessen polygon map of rainfall distribution.

3.4 Conventional model (HEC-HMS)

The first approach employed the HEC-HMS model. Precipitation and discharge data were used as model inputs. For model development, the Soil Moisture Accounting method was used to model loss parameters, the Clark Unit Hydrograph method was used to model direct runoff, and the recession-based flow method was applied to model base flow. The model was initially calibrated to optimize parameter settings and then validated with independent data to assess its predictive accuracy. This process resulted in simulated streamflow values representing the performance of the conventional model.

3.5 Machine Learning models

In the second approach, various machine learning models namely Artificial Neural Networks (ANN), LSBoost, and Random Forest were applied. These models were trained, validated, and tested using relevant hydrological inputs to simulate streamflow.

After model training, the best-performing ML architecture was selected based on performance during validation and testing.

3.6 Hybrid model (HEC-HMS-ML)

To leverage the strengths of both modelling paradigms, a hybrid modelling approach was developed. This model combined the physical-based HEC-HMS output with machine learning techniques. Here, precipitation, observed discharge, and the simulated output from HEC-HMS were used as inputs to train the hybrid ML model.

3.7 Model evaluation and comparison

All three approaches HEC-HMS, selected ML model, and the hybrid model were evaluated using key statistical performance metrics, including Nash–Sutcliffe Efficiency (NSE), Root Mean Square Error after normalization (nRMSE), and Coefficient of Determination (R^2). These metrics enabled a direct comparison of each model's predictive accuracy. Based on the evaluation results, the model that demonstrated the best overall performance was selected as the most suitable approach for streamflow simulation in the study area.

4. Results and Discussion

4.1 HEC-HMS model evaluation

Considering the long-term simulation, the HEC-HMS model performed better with an NSE, PBIAS, nRMSE during calibration and validation. These results indicate that HEC-HMS has a strong ability to replicate observed streamflow. Table 1 shows the performance metrics of the HEC-HMS model.

Table 1: HEC-HMS model performances

Performance metric	HEC-HMS	
	Calibration	Validation
NSE	0.821	0.827
PBIAS (%)	-5.84	11.75
RMSE	0.04	0.04
R^2	0.82	0.84

4.2 Machine learning models evaluation

Based on performance metrics across training, validation, and test datasets, the ANN model outperforms LSBoost and Random Forest. It records the lowest normalized RMSE (0.051) and the highest NSE (0.901) and R^2 (0.905) on the test set, indicating strong accuracy and generalization. While LSBoost shows high training performance, it drops significantly in validation and testing, suggesting overfitting. Random Forest shows moderate but less consistent results.

4.3 Final model evaluation

The final results show that the Hybrid Model outperforms both HEC-HMS and ANN across all metrics. In the testing phase, the Hybrid Model maintained superior performance (NSE: 0.964, R^2: 0.967, RMSE: 0.032, PBIAS: 6.25%), while ANN had slightly higher errors. Overall, the Hybrid Model proved most accurate and reliable for streamflow prediction. Table 2 shows the evaluation of models.

Table 2: Final evaluation of the models

Model	Validation				Test			
	NSE	R^2	PBIAS (%)	RMSE	NSE	R^2	PBIAS (%)	RMSE
HEC-HMS	0.83	0.84	11.75	0.04	—	—	—	—
ANN (FFBPNN)	0.84	0.85	7.36	0.06	0.90	0.90	7.52	0.05
Hybrid	0.94	0.95	6.79	0.04	0.96	0.97	6.25	0.03

4.4 Discussion

The HEC-HMS model reproduces low-flow variations satisfactorily but shows limited accuracy in simulating peak discharges, frequently over- or underestimating extreme events. Compared to the ANN model, its performance during high-flow conditions is weaker, indicating constraints in representing extreme hydrological responses. Figure 4 illustrates the comparison between simulated and observed discharge at the Hanwella outlet during validation.

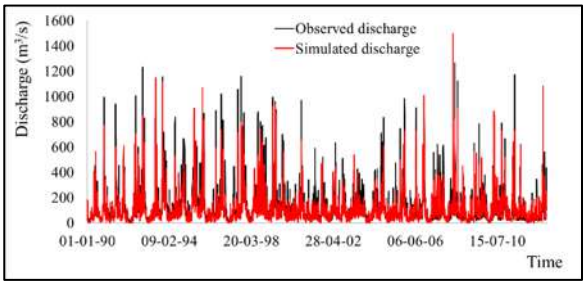

Figure 4: Variation of observed and simulated discharge in the validation of HEC-HMS model

The ANN model accurately captures discharge fluctuations, especially during low flow periods. However, it slightly over or underestimates during peak flows, indicating challenges in simulating extreme events. Despite this, the close match between actual and predicted values confirms the model's reliability for general hydrological analysis and water resource management under normal conditions. Figure 5 shows the comparison of observed and simulated river discharge on the testing set of ANN model.

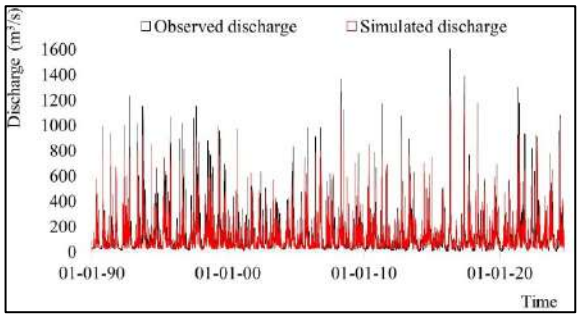

Figure 5: Comparison of observed and simulated discharge on the testing set

This hybrid model, which combines ANN with HEC-HMS simulated discharge as an additional input, shows a clear improvement over the standalone ANN in capturing both base flow and peak flow events. While the ANN struggled slightly during extreme discharge periods, this hybrid model effectively captures the timing and magnitude of high-flow events, demonstrating its superior ability to handle complex hydrological dynamics. Figure 6 shows the comparison of observed and simulated river discharge on the testing set of ANN model.

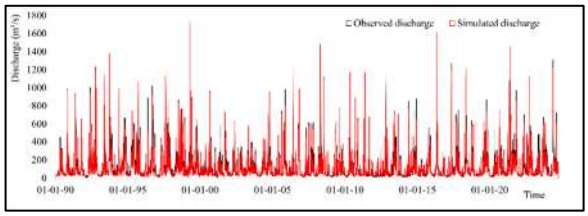

Figure 6: Comparison of observed and simulated river discharge on the testing set of hybrid model

5. Conclusions

Performance comparisons among the models demonstrate the effectiveness of the hybrid approach. The ANN model exhibited a 9% improvement over the traditional HEC-HMS, showcasing the strength of data-driven modelling. The hybrid model further enhanced simulation accuracy, achieving a 14% higher performance than HEC-HMS and a 7% improvement over the ANN model alone. These results confirm that the Hybrid HEC-HMS-ANN model is the most reliable method for streamflow estimation in the Upper Kelani River Basin.

References

Asaad, M.N., Eryürük, Ş. and Eryürük, K. (2022) 'Forecasting of Streamflow and Comparison of Artificial Intelligence Methods: A Case Study for Meram Stream in Konya, Turkey', *Sustainability (Switzerland)*, 14(10). doi: 10.3390/su14106319

De Silva, M.M.G.T., Weerakoon, S.B. and Herath, S. (2014) 'Modeling of Event and Continuous Flow Hydrographs with HEC–HMS: Case Study in the Kelani River Basin, Sri Lanka', *Journal of Hydrologic Engineering*, 19(4), pp. 800–806. doi: 10.1061/(asce)he.1943-5584.0000846

Deulkar, A.M. et al. (2024) 'Rainfall-runoff modelling–a comparison of Artificial Neural Networks (ANNs) and Hydrologic Engineering Centre-Hydrologic Modelling System (HEC-HMS)', *ISH Journal of Hydraulic Engineering*, 30(4), pp. 478–488. doi: 10.1080/09715010.2024.2346244

Gunathilake, M.B. et al. (2021) 'Hydrological Models and Artificial Neural Networks (ANNs) to Simulate Streamflow in a Tropical Catchment of Sri Lanka', *Applied Computational Intelligence and Soft Computing*, 2021. doi: 10.1155/2021/6683389

Kedam, N. et al. (2024) 'River stream flow prediction through advanced machine learning models for enhanced accuracy', *Results in Engineering*, 22, p. 102215. doi: 10.1016/j.rineng.2024.102215

Mugume, S.N. et al. (2024) 'Development and application of a hybrid artificial neural network model for simulating future stream flows in catchments with limited in situ observed data', *Journal of Hydroinformatics*, 26(8), pp. 1944–1969. doi: 10.2166/hydro.2024.066

Reddy, N.M., Saravanan, S. and Abijith, D. (2023) 'Streamflow simulation using conceptual and neural network models in the Hemavathi sub-watershed, India', *Geosystems and Geoenvironment*. doi: 10.1016/j.geogeo.2022.100153

DROUGHT ANALYSIS IN A TROPICAL RIVER BASIN IN SRI LANKA

Nilumindi M.T.[1,*], Niwarthana E.G.S.[1], and De Silva M.M.G.T.[1]

[1]Department of Civil Engineering, Faculty of Engineering, University of Peradeniya, Sri Lanka

[*] e19263@eng.pdn.ac.lk

Abstract

Drought is a recurrent natural hazard that significantly affects water resources, agriculture and ecosystems, particularly in tropical river basins. This study analyzes meteorological, hydrological and agricultural droughts in Kirindi Oya River Basin in Sri Lanka using historical data. The Standardized Precipitation Index (SPI), Streamflow Drought Index (SDI) and remote sensing-based NDVI and Vegetation Condition Index (VCI) were used to assess drought conditions. Drought characteristics were evaluated at 1, 3, 6, and 12 months timescales. Pearson correlation analysis examined relationships among indices to identify drought propagation patterns and lag effects. The results revealed significant spatial and temporal variability in drought occurrence and progression across the basin. This study highlights the importance of using a multi index, multi timescale approach to improve drought monitoring and early warning systems. The findings support better drought preparedness, agricultural planning and water resource management in drought prone regions in Sri Lanka.

Keywords: Drought analysis, meteorological drought, hydrological drought, agricultural drought, Kirindi Oya River Basin

1. Introduction

Drought is a major environmental hazard caused by prolonged water deficiency, severely affecting agriculture, water resources, and ecosystems. It is classified into four types: meteorological drought, due to reduced rainfall; agricultural drought, resulting from insufficient soil moisture for crops; hydrological drought, associated with decreased streamflow and groundwater levels; and socioeconomic drought, which impacts livelihoods and the economy. This complexity makes drought a far-reaching phenomenon.

This study analyzes meteorological, hydrological, and agricultural droughts in the Kirindi Oya River Basin, Sri Lanka, using historical data that are not widely discussed in the literature. The objectives are to estimate meteorological, hydrological, and agricultural drought indices and to examine the correlations among these indices.

The multi-index, multi-timescale approach emphasizes the importance of drought monitoring and supports improved preparedness, agricultural planning, and water resource management in the basin.

The Kirindi Oya River Basin, located in southeastern Sri Lanka between 6°18′–6°54′ N and 80°45′–81°45′ E, covers approximately 1,190 km² and extends about 118 km from the central highlands to the Indian Ocean. It supports major irrigation schemes, including Yoda Wewa and Lunugamvehera, which are vital for agriculture.

Figure 1: Kirindi oya river basin

The region experiences a dry climate with 1000–1500 mm of annual rainfall, mainly from the northeast monsoon and temperatures ranging from 26°C to 30°C, contributing to high

evaporation and water scarcity. Land use includes various crops such as tea, rubber, sugarcane and fruit, along with forested areas.

2. Literature review

Drought is a slow-onset, widespread environmental hazard caused by reduced precipitation, rising temperatures and largescale atmospheric phenomena such as El Niño (Yan et al., 2016). It is categorized into meteorological, hydrological, agricultural and socioeconomic types, with the first three being most studied due to their measurable impacts. Meteorological drought is assessed using indices like SPI and SPEI, while hydrological drought often lagging behind is evaluated using streamflow indices such as SDI. Agricultural drought, linked to soil moisture deficits and vegetation stress, is monitored using NDVI and VCI (Saha et al., 2018). The temporal lag among drought types emphasizes the need for integrated assessment. Using meteorological, hydrological and agricultural indices enables comprehensive monitoring, particularly in agriculture dependent basins like Kirindi Oya in Sri Lanka (Abeysingha et al., 2020), aiding early warning and adaptive resource management under climate change.

3. Methodology

3.1 Workflow

The methodology follows a structured approach, starting with data collection and pre-processing, then classifying drought types and finally conducting comparative and correlation analysis of selected drought indices. Figure 2 represents the workflow diagram.

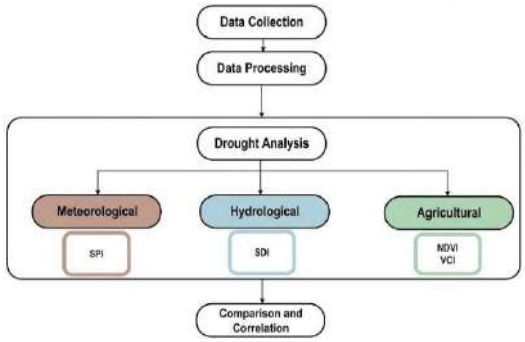

Figure 2: Workflow diagram

3.2 Data Collection

To evaluate drought characteristics in the Kirindi Oya River Basin, multiple datasets were acquired. A 35-year historical record from six rainfall gauge stations (Thissamaharama, Bundala Lewaya, Wellawaya, Bandara Eliya, Bandarawela, and Lunugamwehera) was obtained from the Meteorological Department. Data from two stream gauge stations at Thanamalwila and Wellawaya were obtained from the Irrigation Department. MODIS based NDVI data were accessed via Google Earth Engine.

3.3 Data Processing

To ensure data quality and spatial coverage, missing rainfall data (<10%) were estimated using the Inverse Distance Weighted (IDW) method. Consistency was verified using double mass curve analysis and corrections were applied to Thissamaharama and Wellawaya stations. The Thiessen Polygon method was used to spatially distribute rainfall, dividing the basin into zones namely; Intermediate, Dry and Arid Zones (Figure 3).

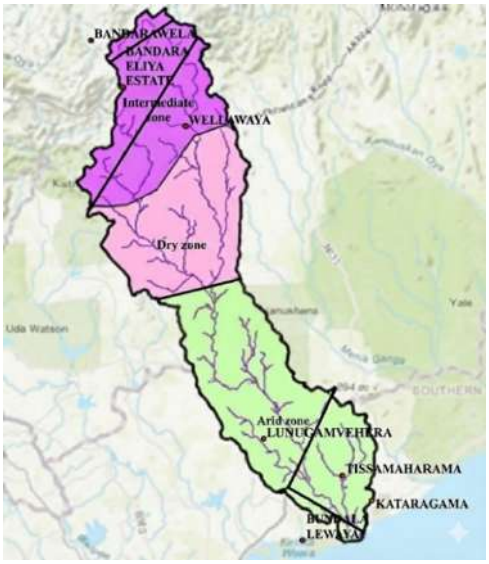

Figure 3*:* Thiessen Polygon Map of Rainfall Distribution

3.4 Drought Analysis

Droughts were evaluated across timescales of 1, 3, 6 and 12 months using a combination of meteorological, hydrological and agricultural indices.

The Standardized Precipitation Index (SPI) was computed to assess precipitation deviations relative to the long-term average for each climate zone, providing a standardized measure of meteorological drought severity.

$$SPI = \frac{X_i - \overline{X}}{s} \qquad (1)$$

Where Xi is the accumulated precipitation for a specific time period and $\bar{X}$ and s are the mean and standard deviation of the long-term monthly precipitation series, respectively.

The Standardized Precipitation Index (SPI) was calculated by fitting monthly precipitation data to a gamma distribution to handle its skewed nature. SPI uses accumulated precipitation along with the long term mean and standard deviation of monthly rainfall. It classifies conditions as extremely wet (≥2), very wet (1.5 to <2), moderately wet (1 to <1.5), near normal (-1 to 1), moderately dry (-1.5 to <-1), severely dry (-2 to <-1.5) and extremely dry (≤-2).

Based on the cumulative streamflow volumes $V_{i,k}$, the Streamflow Drought Index (SDI) was defined for each reference period k of the i th hydrological year as follows:

$$SDI_{i,k} = \frac{V_{i,k} - \bar{V}_k}{S_k} \; i = 1, 2, \ldots, \quad k = 1, 2, 3, 4 \qquad (2)$$

$\bar{V}_k$ and S_k were, respectively, the mean and the standard deviation of cumulative streamflow volumes of the reference period k, as they were estimated over a long period of time.

The Streamflow Drought Index (SDI) classifies hydrological drought as non-drought (SDI ≥ 0), mild (-1 to 0), moderate (-1.5 to -1), severe (-2 to -1.5), and extreme (< -2).

Agricultural drought was analyzed using the Vegetation Condition Index (VCI), which indicates vegetation health. VCI values of 80–100 mean wet conditions, 60–80 indicate no drought, 40–60 mild drought, 20–40 severe drought and 0–20 extreme drought. VCI was calculated using NDVI values derived from satellite imagery. The Vegetation Condition Index (VCI) compared the current NDVI with measured historical NDVI values. It was defined by the following equation:

$$\mathrm{VCI} = \frac{\mathrm{NDVI} - \mathrm{NDVI}_{\min}}{\mathrm{NDVI}_{\max} - \mathrm{NDVI}_{\min}} \times 100, \qquad (3)$$

4. Results and Discussion

4.1 Standardized Precipitation Index (SPI) Analysis

Drought years in intermediate, dry and arid zones were identified using the Standardized Precipitation Index (SPI), showing spatial and temporal variability. The intermediate zone experienced severe droughts in 1991, 1995, 2001 and 2014. The dry zone had severe droughts in 1991, 1995, 2001, 2009 and 2014. The arid zone faced the most frequent droughts, with severe events in 1990, 1993, 1999, 2006, 2014 and 2017. Droughts in 1991, 1995, 2001, 2009, and 2014 affected multiple zones, indicating widespread dry conditions. Figure 4 shows SPI values for the Dry Zone.

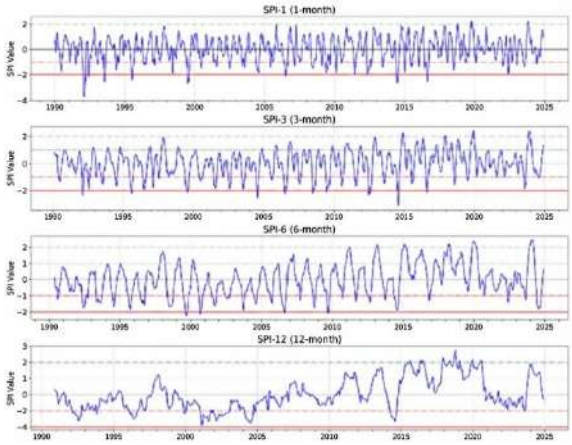

Figure 4: SPI values for Dry zone

4.2 Streamflow Drought Index (SDI) Analysis

Using the Streamflow Drought Index (SDI), significant hydrological droughts were identified in the Thanamalwila and Wellawaya catchments. Thanamalwila experienced major droughts in years like 1992, 2002, 2004, 2009, 2014, and 2023, while Wellawaya saw droughts in 1993, 2002, 2009, and 2021. Several drought years overlapped in both regions, such as 1999, 2004, 2009, 2012, 2014 and 2017, indicating widespread hydrological stress. Figure 5 shows the SDI values for the Thanamalwila.

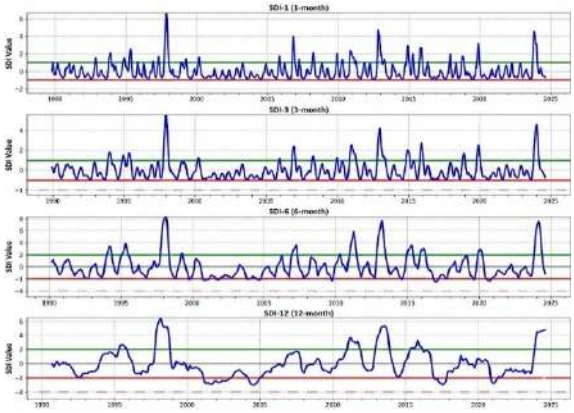

Figure 5: SDI values for Thanamalwila

4.3 Vegetation Condition Index (VCI) Analysis

Agricultural drought in the Kirindi Oya basin was assessed using the Vegetation Condition Index (VCI), with values below 40% indicating severe vegetation stress. Severe droughts occurred in the intermediate zone during 2004,

2010, 2013, 2016 and 2023; in the dry zone during 2007, 2014, 2016, and 2020; and in the arid zone during 2004, 2010, 2012, 2014 and 2019. Overlapping droughts in 2004, 2010, 2014, and 2016 highlight widespread agricultural stress. Figure 6 presents VCI values for the Dry Zone.

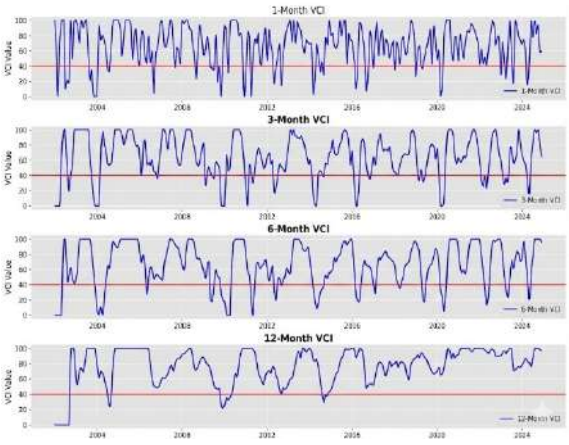

Figure 6: VCI values for Dry zone

4.4 SPI – SDI Correlation analysis

Analysis of SPI and SDI correlations across intermediate and dry revealed strong positive relationships, with Pearson correlation coefficients ranging between 0.6 and 1.0. A regression equation was derived between the SPI and the SDI to quantify the relationship between meteorological and hydrological droughts. Table 1 shows correlation values between SPI and VCI which is a good correlation.

Table 1: Correlation values between SPI and VCI

SPI-SDI	Correlation Values			
	1 Month	3 Month	6 Month	12 Month
Intermediate – Thanamalwila	0.63	0.69	0.72	0.68
Intermediate – Wellawaya	0.63	0.70	0.77	0.84
Dry – Thanamalwila	0.62	0.67	0.68	0.60

4.5 SPI – VCI Correlation analysis

The very poor SPI-VCI correlations in Kirindi Oya Basin. As an example, the correlation between SPI and VCI at 6 and 12 month timescales for the arid zone is illustrated in Figure 7.

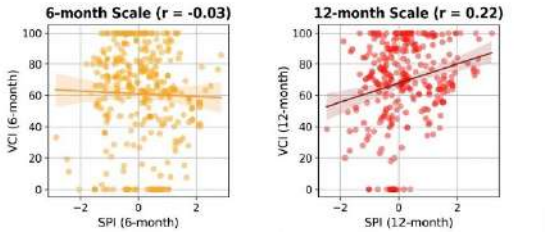

Figure 7: SPI - VCI Correlation for 6 and 12 time scales in Arid zone

5. Conclusions

The analysis confirms that drought indices effectively detect drought conditions in the Kirindi Oya River Basin. The arid zone experienced the most frequent and severe droughts, followed by the dry and intermediate zones. A strong correlation between SPI and SDI suggests that meteorological droughts rapidly develop into hydrological droughts. However, the weak correlation between SPI and VCI indicates that vegetation response is affected by irrigation, land use, and remote sensing limitations such as cloud cover, low resolution, and lack of ground validation. These results highlight the importance of integrating multiple indices for accurate drought monitoring and effective management.

6. References

Abeysingha, N.S., Jayasekara, J.M.N.S. and Meegastenna, T.J. (2020) 'Stream flow trends in up and midstream of Kirindi Oya river basin In Sri Lanka and its linkages to rainfall', *Mausam*, 68(1), pp. 99–110. doi: 10.54302/mausam.v68i1.437

Saha, A., Patil, M., Goyal, V.C. and Rathore, D.S. (2018) 'Assessment and Impact of Soil Moisture Index in Agricultural Drought Estimation Using Remote Sensing and GIS Techniques', *Proceedings*, 7(1), p. 2. doi: 10.3390/ecws-3-05802

Yan, H., Wang, S.Q., Wang, J.B., Lu, H.Q., Guo, A.H., Zhu, Z.C., Shugart, H.H. and Myneni, R.B. (2016) 'Assessing spatiotemporal variation of drought in China and its impact on agriculture during 1982–2011 by using PDSI indices and agriculture drought survey data', *Journal of Geophysical Research*, 121(5), pp. 2283–2298. doi: 10.1002/2015JD024285

MORPHOLOGICAL EVOLUTION OF DEDURU OYA

Wanigasooriya I.W.M.T.C.[1,*], Tharindi M.G.T.[1] and Dias D.D.[1]

[1]Department of Civil Engineering, Faculty of Engineering, University of Peradeniya, Sri Lanka

* thariniwanigasooriya@gmail.com

Abstract

The Deduru Oya River in Sri Lanka exhibits notable morphological evolution due to natural fluvial processes and human influences, affecting downstream ecosystems, land use, and increasing the risk of erosion and flooding. This study investigates the river's dynamic behavior over a ten-year period (2015–2025), focusing on changes in sinuosity, sediment bar area, and sediment bar aspect ratio at selected downstream locations. Landsat and Sentinel-2 satellite imagery, processed via Google Earth Engine (GEE), was used to derive these parameters. Sentinel-2's higher spatial resolution enabled more sensitive detection of recent meandering and subtle morphological variations, particularly near the estuary. Results revealed a steady increase in sinuosity, with values exceeding 2.8–2.9 at several points, suggesting enhanced meandering and potential anabranching. Sediment bar area showed spatial and temporal variability, while aspect ratios varied significantly, especially near the Wilattawa dam, reflecting diverse flow energy and deposition patterns. Larger meander loops were most evident near the estuarine outlet, where channel widening and divergence were prominent. These findings offer valuable insights into morphological dynamics in tropical river systems and provide a framework for future fluvial monitoring and geomorphological studies.

Keywords: Sinuosity, Sediment Bar Aspect Ratio, Sentinel, Landsat, Google Earth Engine

1. Introduction

The Deduru Oya River(Figure 1), Sri Lanka's sixth-longest at 142 km, flows west from Kurunegala to the Indian Ocean, supporting agriculture, domestic use, and biodiversity. In recent years, its downstream section has experienced notable morphological changes due to natural and human factors. This study analyses fluvial dynamics from 2015 to 2025 using Sentinel-2 and Landsat data via Google Earth Engine. Key parameters include sinuosity, sediment bar area, and aspect ratio, offering insights into evolving river morphology. The aim is to better understand the fluvial dynamics of the river and to identify patterns and potential future developments in river morphology.

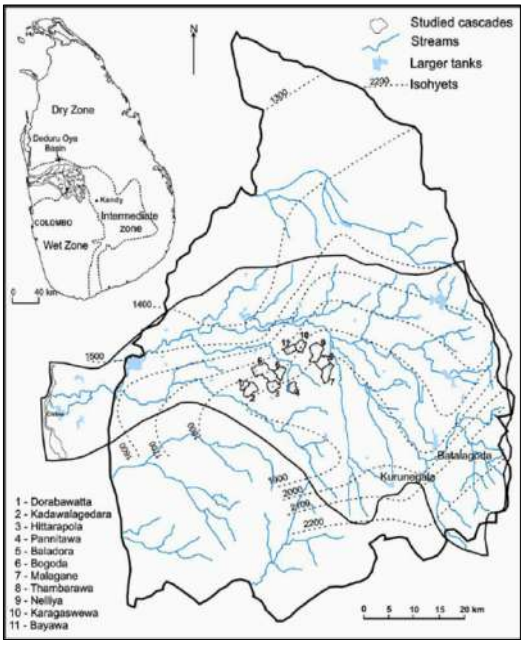

Figure 26: Deduru oya stretch in Sri Lanka Map (Jayasena et al., 2011)

1.1 Study Area

In this study, we focused on the lower reaches of the Deduru Oya River, particularly the downstream areas near the estuary where morphological changes are most prominent. Multiple points along different stretches of the river were selected for the analysis of sinuosity and sediment bar dynamics.

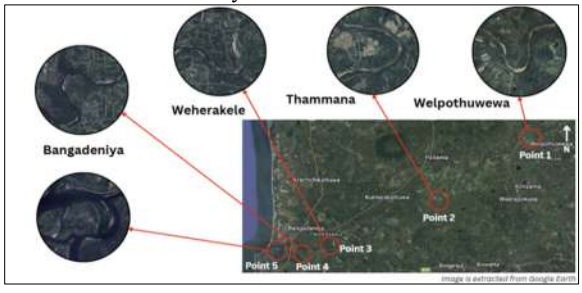

Figure 27: Study Area for Meandering Behavior These locations were selected based on visible meanders and sediment patterns seen in satellite imagery from 2015 to 2025.

Special attention was given to sites such as Wilattawa and Weherakale due to their significant fluctuations in sediment bar formation and extent.

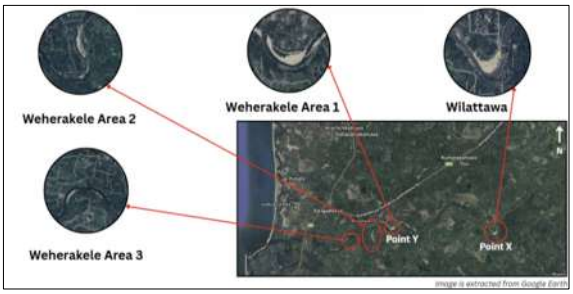

Figure 28: Study Area for Sediment Bar Changes

Figure 29: Larger Meandering Places Near Estuary

2. Literature Review

Understanding river morphological changes is essential for predicting erosion-prone zones and managing sediment transport. Among the critical parameters in river morphology studies are sinuosity, sediment bar area, and sediment bar aspect ratio.

2.1 Sinuosity

Sinuosity measures the deviation of a river from a straight path and is given by the ratio of the actual watercourse length to the straight-line valley length. It reflects the degree of meandering, with values greater than 1.5 indicating meandering rivers (Akbar et al., 2019).

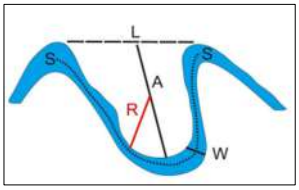

W-River width
S-Water flow Length
L-Meander neck length
A-Axis length
R-Radius of curvature

Figure 30: Model of curve winding morphometric parameters (Akbar et al.,2019)

$$\text{Sinuosity} = \frac{\text{Water Flow Length}}{\text{Meander Neck Length}} \quad (1)$$

Elevated sinuosity values suggest lateral migration and potential instability in the channel, often leading to erosion and sediment redistribution.

2.2 Sediment Bar Aspect Ratio

Sediment bars, indicative of depositional processes, serve as important indicators of sediment transport dynamics. Their area provides a quantitative measure of deposition over time, and their aspect ratio offers geometric insight into their formation:

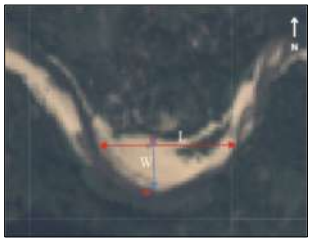

L- Longest horizontal length of sediment bar
W- Widest vertical width of sediment bar (L & W are measured perpendicular to each other)

Figure 31: Sediment Bar Aspect Ratio measured using L and W from satellite images

$$\text{Sediment Bar Aspect Ratio} = \frac{\text{Horizontal Length (L)}}{\text{Vertical Width (W)}} \quad (2)$$

High aspect ratios imply elongated sediment deposits aligned with flow direction, whereas low ratios may indicate broader, more dispersed formations.

Previous studies have shown that sediment bar geometry reflects fluvial dynamics and channel changes. For example, Basnayaka et al. (2022) emphasized the usefulness of remote sensing, particularly Sentinel-2 imagery, for studying sediment dynamics and suggested its further development for analyzing sediment bar changes in the Deduru Oya River. Hooke (2013) noted that elongated bars often result from lateral migration. Zhou et al. (2023) also demonstrated that long-term satellite data can effectively track bar area and shape changes linked to flow variability and human impacts. These findings support the use of aspect ratio alongside other metrics to assess morphological changes in the Deduru Oya River.

3. Methodology

Satellite images from Landsat and Sentinel-2 (2015–2025) were processed via Google Earth

Engine (GEE) to generate annual cloud-free median composites. At selected downstream sites, river sinuosity was computed using Akbar et al. (2019) (Equation 1). Sediment bar areas and aspect ratios were manually measured using pixel dimensions (Equation 2). Key meander loops, particularly near the estuary, were visually identified and tracked to assess spatial evolution. Temporal analysis enabled the evaluation of morphological changes and detection of larger meandering zones.

4. Results and Discussions

4.1 Sinuosity

Sinuosity gradually increased from 2015 to 2025 at several downstream locations (ex at estuary, Thammana), with noticeable changes after 2018. The highest values appeared near the estuary, indicating stronger meandering and lateral channel shifts in that area. This trend suggests ongoing morphological adjustments likely influenced by natural flow dynamics and sediment deposition.

Table 6: Temporal variation in river sinuosity at Point 5 (Sentinel-2 vs Landsat, 2015–2025)

Year	Point 5	
	Sinuosity (Sentinel)	Sinuosity (Landsat)
2025	3.08	3.23
2024	3.05	2.84
2023	2.89	No Data
2022	2.81	No Data
2021	2.74	2.65
2020	2.57	No Data
2019	2.62	2.49
2018	2.56	2.51
2017	2.46	2.24
2016	2.29	No Data
2015	No Data	2.27

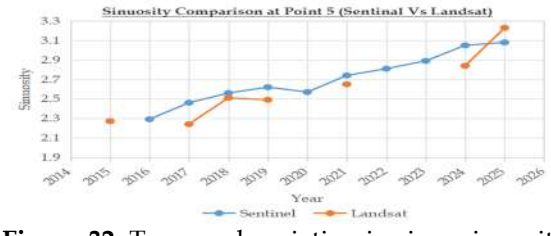

Figure 32: Temporal variation in river sinuosity at Point 5 (Sentinel-2 vs Landsat, 2015–2025)

4.2 Sediment Bar Aspect Ratio

Aspect ratios varied annually, indicating changes in the shape and spread of bars. A shift toward elongated bars was noted in later years, possibly due to increased sediment transport and deposition patterns driven by meandering. At Wilattawa (Point 5), significant variation was observed, indicating dynamic morphological adjustments and altered sediment deposition patterns.

Table 7: Yearly Changes in Sediment Bar Aspect Ratios at Wilattawa (Sentinel-2 vs Landsat, 2015–2025)

Year	Point X	
	Sediment bar Ratio (Sentinel)	Sediment bar Ratio (Landsat)
2025	1.83	1.45
2024	1.86	1.29
2023	No Data	No Data
2022	1.96	1.49
2021	2.05	No Data
2020	1.67	1.36
2019	1.74	1.47
2018	2.61	1.59
2017	2.57	1.68
2016	2.58	No Data
2015	No Data	0

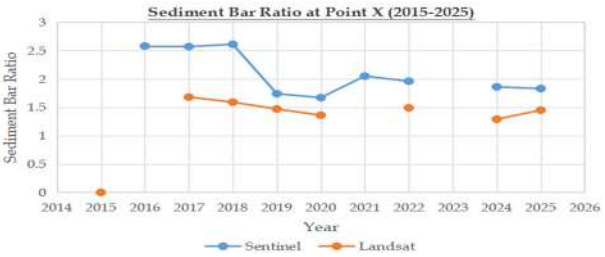

Figure 33: Temporal variation in Sediment bar Aspect Ratio at Point X (Sentinel-2 vs Landsat, 2015–2025)

4.3 Sediment Bar Area

In 2018, Wilattawa experienced a notable increase in sediment bar area, while Weherakale and other regions saw declines due to a major flood that deposited sediment 2022, all study areas showed increased sediment bar extent, likely due to drought conditions. Aside from these events, a general decline in sediment bar area has occurred since 2018. These patterns demonstrate the significant impact of climatic

events, such as floods and droughts, on sediment dynamics in the Deduru Oya river system.

Figure 34: Sediment Bar Area Change over time (2016-2025)

4.4 Larger Meandering Places

As shown in Figure 3, Areas 1, 2, and 3 near the estuary display significant meander loop development from 2016 to 2025. Figure 10 highlights a steady increase in branch lengths and widths, indicating intensified meandering. These pronounced bends may lead to anabranch formation or delta initiation, with a potential estuary shift in Area 1 within the next 20–30 years. However, the pace of these changes may vary depending on future flood events and climate conditions.

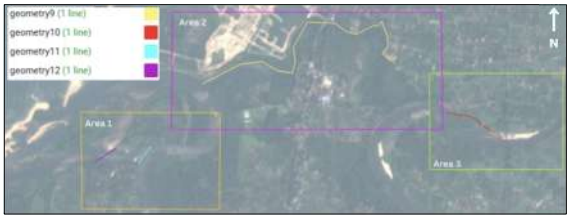

Figure 35: Meander Length and Width Variations in Areas 1, 2, and 3 Based on 2025 Sentinel-2 Imagery

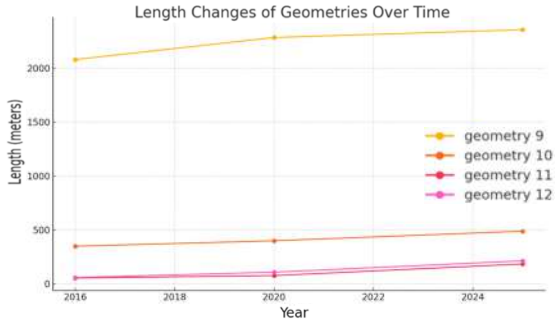

Figure 36: Comparison of Meander Branch Length and Width Growth from 2016 to 2025 in Estuarine Areas

5. Conclusions

This study successfully assessed the morphological evolution of the Deduru Oya River over a ten-year period (2015–2025) using remote sensing data. Key parameters such as sinuosity, sediment bar aspect ratio, and sediment bar area revealed significant changes, especially in downstream regions. The increasing sinuosity and elongated sediment bars indicate active meandering and potential erosion risk. Additionally, larger meander formations near the estuary suggest geomorphological instability that may lead to future anabranching. These findings offer valuable insights into fluvial dynamics in tropical river systems.

References

Akbar, I. and Setiawan, B. (2019) 'Morphometric analysis for evaluation of environmental change and disaster reduction of flood', *Sriwijaya Journal of Environment*, 4(2), pp. 52–58. doi: 10.22135/sje.2019.4.2.52-58

Basnayaka, V., Samarasinghe, J.T., Gunathilake, M.B., Muttil, N., Hettiarachchi, D.C., Abeynayaka, A. and Rathnayake, U. (2022) 'Analysis of meandering river morphodynamics using satellite remote sensing data—An application in the lower Deduru Oya (River), Sri Lanka', *Land*, 11(7), p. 1091. doi: 10.3390/land11071091

Gargiulo, M., Cavallo, C. and Papa, M.N. (2025) 'Mapping of fluvial morphological units from Sentinel-1 data using a deep learning approach', *Remote Sensing*, 17(3), p. 366.

Hooke, J.M. (2013) 'River meandering', in Shroder, J. (ed.) *Treatise on Geomorphology*. San Diego, CA: Academic Press, pp. 260–288.

International Journal of Advanced Research (2020) 'Management of the sediment transported by the South Mahanadi deltaic rivers to the Chilika Lagoon'. Available at: (Accessed: 19 February 2026).

Jayasena, H.A.H., Chandra, R. and Gangadhara, K.R. (2011) 'Water Management in Ancient Tank Cascade Systems (TCS) in Sri Lanka: Evidence for Systematic Tank Distribution', *Journal of the Geological Society of Sri Lanka*, 14, pp. 29–33.

Zhou, N., Sheng, S., He, L.-Y., Tian, B.-R., Chen, H. and Xu, C.-Y. (2023) 'An integrated approach for analyzing the morphological evolution of the lower reaches of the Minjiang River based on long-term remote sensing data', *Remote Sensing*, 15(12), p. 3093. doi: 10.3390/rs15123093

NOVEL COATING MATERIAL TO PREVENT FAT, OIL AND GREASE DEPOSITION IN SEWER

Dinuwan I.M.T.S [1,*], Palliyaguru N.M [1], and Nanayakkara K.G.N [1]

[1]Department of Civil Engineering, Faculty of Engineering, University of Peradeniya, Sri Lanka

* Shanukat385@gmail.com

Abstract

Buildup of fat, oil, and grease (FOG) in sewer systems creates blockages and maintenance problems within sewer systems. This study presents an innovative, environmentally friendly coating material made with locally-sourced biomass based fly ash to mitigate deposition of FOG onto sewer pipes. Fly ash is also a cheap material and it has a high hydrophobic silica (SiO_2) content. Our coating was hydrophobic and self-cleaning and was made by mixing fly ash with epoxy-resin and ethanol. Trial coatings were prepared by varying fly ash content from 1% to 30%. Trial coatings applied to concrete substrate and test for hydrophobicity and self-cleaning using contact angle and sliding angle tests for performance, and SEM and EDX tests for microstructure and surface chemistry. The coatings were subjected to 21 days of synthetic FOG wastewater treatment to simulate sewer conditions. The results indicated that fly ash-enhanced coatings' water resistance and demonstrated lower adhesion to FOG. The coating formulation resulted in more than 50% decrease in FOG buildup compared to uncoated samples. This research highlights the possibility of using industrial waste materials like fly ash to develop cost-effective and environmentally friendly approaches to manage FOG in sewer systems.

Keywords: Coatings, FOG, Fly ash, Hydrophobicity.

1. Introduction

The deposition of fat, oil, and grease (FOG) is a leading cause of sewer clogging and blockages, especially in locations that have high volumes of discharge from food service establishments (FSEs). FOG forms metallic soaps through saponification when it interacts with leached calcium ions (Ca^{2+}) from concrete surfaces. These metallic soaps are able to grow into solid fatbergs that subsequently adhere to pipe walls. Traditional solutions to the issue of FOG comprised grease interceptors, manual maintenance, and chemical dosing. Each of these solutions is costly, very labor-intensive, and only somewhat effective. This study utilizes surface modification of sewer pipes with hydrophobic, self-cleaning coatings as a potential solution to reducing FOG accumulation and resolving the service issues with sewer pipes (He et al., 2017).

This research presents a new, sustainable coating made with fly ash, epoxy resin, and ethanol. Fly ash is a local biomass based industrial waste product that contains high SiO_2, which has inherent hydrophobicity and can be used to enhance the surface roughness of the coating. The coating will reduce calcium leaching, FOG adherence, and sewer asset service life while implementing publicly funded waste in an environmentally sustainable way. The objectives of this study are to develop and characterize a novel coating material to reduce FOG deposition, and to evaluate the coating's performance in preventing FOG accumulation, ultimately enhancing the longevity and efficiency of sewer systems.

2. Literature review

The deposition of Fat, Oil, and Grease in sewer systems is a widespread issue, primarily caused by the discharge of FOG from food service establishments (FSEs). FOG interacts with other wastewater components, particularly calcium ions (Ca^{2+}) leached from concrete surfaces, forming insoluble metallic soaps through a process known as saponification. These soaps accumulate and can form large, solid masses known as "fatbergs," which obstruct sewer pipes, reduce flow, and lead to sewer overflows (He et al., 2017). The accumulation of FOG not only hampers wastewater movement but also contributes to serious environmental and operational challenges in sewer systems.

Current methods for managing FOG, such as grease interceptors, manual cleaning, and chemical dosing, have proven to be expensive, labor-intensive, and often ineffective over time. These traditional solutions fail to address the root cause of FOG buildup, especially in areas with high FOG discharge volumes. As a result, there has been growing interest in developing more efficient and sustainable solutions to mitigate FOG accumulation in sewer systems (Yusuf et al., 2023).

Recent research has explored the use of hydrophobic and self-cleaning coatings as an innovative solution to prevent FOG deposition. These coatings, when applied to sewer pipe surfaces, aim to reduce FOG adherence by creating water-repellent, easy-to-clean surfaces. Coatings made from sustainable materials such as fly ash, which is rich in silica (SiO_2), have gained attention due to their inherent hydrophobic properties and environmental benefits. Fly ash has been shown to enhance surface roughness and improve the water resistance of coatings, making it a promising material for reducing FOG accumulation in sewer systems (Chindaprasirt et al., 2020; Song et al., 2020). In addition, self-cleaning coatings that replicate the natural properties of surfaces like lotus leaves have been explored to further reduce FOG buildup. These coatings not only prevent the accumulation of FOG but also facilitate the removal of any deposits that may form, ultimately extending the service life of sewer infrastructure (Boinovich et al., 2008).

However, despite these advancements, there is still a need to optimize the formulation of these coatings and assess their long-term effectiveness under real-world conditions. The performance of coatings can be influenced by several factors, including coating thickness, surface texture, and hydrophobicity (Chindaprasirt et al., 2020). Further studies are required to fine-tune the coating materials, improve their self-cleaning properties, and evaluate their durability in actual sewer environments.

3. Methodology

3.1 Analysis of fly ash.

Particle size of fly was analysed using sieve analysis test. Fly ash particles less than 63µm was used to prepare trial coatings because fine particles enhance its hydrophobicity and improve the coating's effectiveness in preventing FOG deposition. Elemental composition of fly ash was analysed using XRF analysis.

3.2 Substrate preparation

Concrete blocks of 40mm x 40mm x 10mm were cast using C25 concrete grade and cured for 21 days in water at 28°C. Mortar paste slices (50mm x 50mm x 5mm) were prepared by mixing cement and soil in a 1:2.75 ratio, with a water content of 0.48 and 500 µm aggregate size. These substrates were smoothed using A239 sandpaper to simulate sewer pipe surfaces for the application of coatings. Mortar paste substrates were only used for SEM imaging.

3.3 Trial coating preparation

Fly ash, epoxy resin, and ethanol were mixed in varying concentrations (1% to 30%) to create different coating formulations. The mixture was stirred for 30 minutes after mixing epoxy resin, fly ash and ethanol. Then epoxy hardener was added in a 1:2 ratio with epoxy resin. The final mixture was mixed another 10 minutes before applied to concrete substrates.

3.4 Characterization of coating

The characterization of the coatings was performed using various techniques to assess their performance in terms of hydrophobicity, self-cleaning ability, surface texture, and chemical composition. Contact angle testing was conducted to evaluate the hydrophobicity of the coatings, with higher contact angles indicating better water resistance. Sliding angle tests were carried out to assess the self-cleaning properties, where lower angles suggest better water droplet sliding and self-cleaning behaviour. Scanning Electron Microscopy (SEM) was used to analyse the surface texture and distribution of fly ash particles in the coatings, providing insights into the roughness and uniformity of the coatings. Additionally, Energy Dispersive X-ray (EDX) spectroscopy was employed to examine the elemental composition of the coatings, particularly the presence of silicon and calcium, which are crucial for hydrophobicity and FOG resistance. Self-healing test was also conducted for trial coatings.

3.5 Synthetic FOG waste water preparation.

The synthetic FOG wastewater preparation required 1 litre of solution which contained 175 ml of cooked oil and 200 ml of coconut oil and 5 g of calcium chloride and 625 ml of water. The mixture required 70°C heating to achieve proper

oil blending and calcium chloride dissolution which enabled saponification. The synthetic FOG wastewater was characterized through COD measurement to determine organic pollutant levels as well as electrical conductivity assessment for ionic strength and pH testing for acidity or alkalinity and temperature monitoring for required levels. The prepared wastewater served as the test medium to assess coating performance against FOG deposition in the experiments.

3.6 Selection of best coatings

Based on the results from all characterization techniques (contact angle, sliding angle, SEM, and EDX), five coatings were selected for further evaluation in the FOG deposition study. These trials were chosen due to their promising performance in terms of hydrophobicity, self-cleaning ability, and surface texture. The 5% fly ash coating was identified as the best-performing sample after initial tests, showing the highest hydrophobicity and superior water-repelling characteristics.

3.7 FOG deposition study and comparison

Selected trial coatings, epoxy only coating and uncoated substrates were exposed to prepared synthetic waste water for 21 days. At the end of the time duration deposited FOG on each substrates were carefully scraped off and measure their dry weight compare performance of coatings.

4. Results and discussion

4.1 XRF analysis

Table 4: Elemental composition of fly ash

Element	Composition (%)
Ca	43.67
P	25.76
Si	14.86
K	14.54
Fe	0.93
Sr	0.20

XRF analysis showed a significant amount of silicon (Si) in the fly ash sample. The presence of Si can enhance the hydrophobic properties of coatings, indicating potential functional benefits.

4.1 Contact angle

The 5% fly ash coating had the highest contact angle (101.1°), showing better hydrophobic property than other samples. Epoxy only coating showed contact angle 65.4°.

4.2 Sliding angle

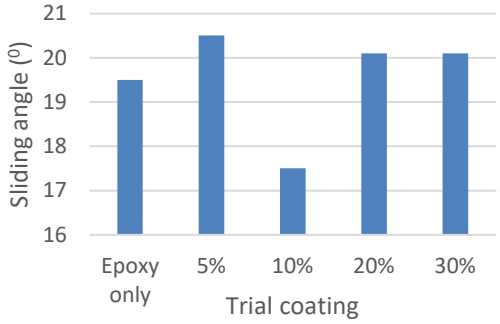

Figure 1: Variation of sliding angle measurement

The 10% fly ash coating had the lowest sliding angle (17.5°), showing better water droplet movement than other samples. All coatings had angles above the 10° self-cleaning threshold, meaning true self-cleaning was not achieved. The improved sliding behavior is due to surface texture created by fly ash particles.

4.3 SEM imaging and EDX

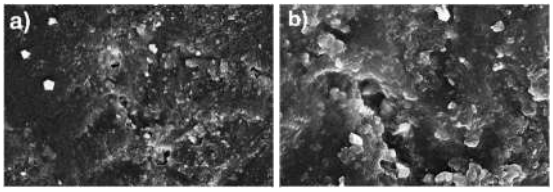

Figure 2: SEM images of epoxy only coating a) 5000x b) 15000x

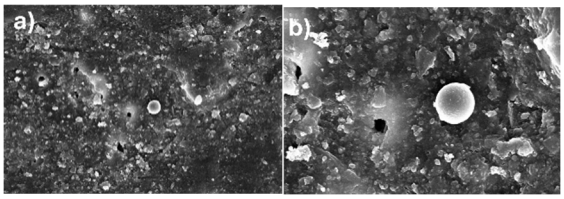

Figure 3: SEM images of 5% fly ash coating a) 5000x b) 15000x

SEM images showed a smooth surface for the epoxy-only coating, while the 5% fly ash coating had a rougher texture with embedded particles. This increased surface roughness helped improve hydrophobicity and reduce FOG adhesion, supporting results from contact and

sliding angle tests. EDX shows the increment of O, N, Ca, Cl and Si content on 5% fly ash coating due to addition of fly ash.

Table 2: Elemental composition on epoxy only coating and 5% of fly ash coating

Element	Epoxy only coatings (w/w %)	5% of fly ash coating (w/w %)
C	78.70	65.30
O	16.01	26.45
N	2.13	2.80
Ca	0.93	2.90
Cl	1.29	1.64
Si	0.39	0.55

4.4 Self-healing test results

Scratched samples were placed in water at room temperature for 7 days. At the end of time period there were not any difference of the scratched marks. Therefore, coatings did not have self – healing property.

4.5 FOG deposition study

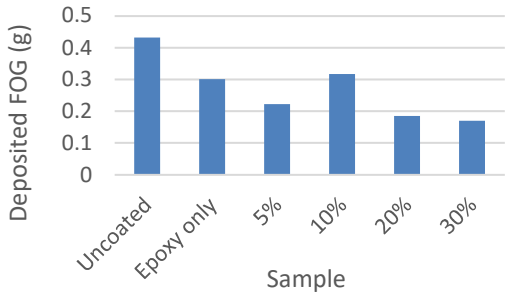

Figure 4: Variation of FOG deposition in each sample

The results showed that the fly ash-enhanced coatings significantly reduced FOG accumulation compared to the epoxy-only coating. The 30% fly ash coating exhibited the best performance, reducing FOG deposition by 60.60% compared to the uncoated sample. The 5% fly ash coating reduced FOG by 48.46%, while the 10% fly ash coating showed a 26.25% reduction. The epoxy-only coating demonstrated the least effectiveness, with a 30.41% reduction in FOG accumulation.

5. Conclusions

The 5% fly ash coating demonstrated hydrophobic properties with a contact angle greater than 90°. While the 10% fly ash coating showed the lowest sliding angle, it did not exhibit self-cleaning ability due to a sliding angle greater than 10°. All fly ash coatings reduced FOG deposition by more than 50% compared to uncoated samples, with the 30% fly ash coating showing the best performance in FOG reduction. Future research should focus on improving self-cleaning and self-healing properties by adding more additives, as fly ash alone cannot achieve all desired properties. The reduction in FOG deposition is a result of a combination of factors, including hydrophobicity, self-cleaning ability, surface properties, and coating thickness.

References

Boinovich, L.B. and Emelyanenko, A.M. (2008) 'Hydrophobic materials and coatings: principles of design, properties and applications', *Russian Chemical Reviews*, 77(7), p.583.

Chindaprasirt, P., Jitsangiam, P., Pachana, P.K. and Rattanasak, U. (2023) 'Self-cleaning superhydrophobic fly ash geopolymer', *Scientific Reports*, 13(1), p.44.

He, X., de los Reyes III, F.L. and Ducoste, J.J. (2017) 'A critical review of fat, oil, and grease (FOG) in sewer collection systems: challenges and control', *Critical Reviews in Environmental Science and Technology*, 47(13), pp.1191–1217.

Song, H., Tang, M., Lei, X., Feng, Z. and Cheng, F. (2020) 'Preparation of ultrafine fly ash-based superhydrophobic composite coating and its application to foam concrete', *Polymers*, 12(10), p.2187.

Yadav, S. and Pramanik, B.K. (2024) 'Novel hybrid coating material with triple distinct healing bond for fat oil and grease deposition control in the sewer system', *Chemical Engineering Journal*, 499, p.156226.

Yusuf, H.H., Roddick, F., Jegatheesan, V., Gao, L. and Pramanik, B.K. (2023) 'Tackling fat, oil, and grease (FOG) build-up in sewers: insights into deposit formation and sustainable in-sewer management techniques', *Science of the Total Environment*, 904, p.166761.

EVALUATION OF MICROPLASTICS CONTENT IN URBAN ENVIRONMENT

Rathnayake, R.W.A.R.M.M.O.[1,*], Witharana, C.D.[1], and Dr. Gunawaradana, W.C.T.K.[1]

[1] Department of Civil Engineering, University of Peradeniya

* menukaosanda@gmail.com

Abstract

Microplastic (MPs) pollution is a growing environmental concern due to its persistence and risks to human health and ecosystems. MPs are synthetic polymer particles smaller than 5 mm, originating from tire wear, textiles, and degraded plastics. Road dust is a major source of MPs in urban environments, particularly in high-traffic areas, as it can be resuspended and transported over long distances. This study investigated the presence of MPs and pollutant loads in road dust and air in urban areas of Kandy, Sri Lanka. Samples were collected during the dry period from two congested indoor and outdoor parking locations. Seven road dust samples and two air samples were collected during weekday peak hours. Indoor samples included separate collections from areas used by four-wheelers, three-wheelers, and motorbikes to assess vehicle-type influence. Road dust samples were sieved and examined for Total Suspended Solids (TSS), digested organic matter, and MPs. Air samples were analyzed for PM10 and MPs. MPs were extracted by density separation and identified using microscopy. Results confirmed MPs in all samples, with black-colored fragments, fibers, and films being dominant and typically under 300 µm. The study highlights the influence of traffic intensity, road surface roughness and weather conditions on MP accumulation.

Keywords: Airborne Microplastics, Dry Period, Microplastics, Road Deposited Dust, Urban Pollution

1. Introduction

Urban air pollution is a growing concern in developing cities, with road dust playing a major role due to its complex composition of organic, inorganic, and plastic-based particles. In Sri Lanka, Kandy is especially prone to dust accumulation because of its basin-shaped topography, limited airflow, and heavy traffic. Microplastics (MPs), defined as plastic particles smaller than 5 mm, have recently emerged as a major concern in urban dust due to their persistence and associated health risks. They can originate from sources such as tire wear, road-marking paint, and plastic debris.

This study addresses this gap by investigating the concentration, characteristics, and distribution of MPs in build-up road dust and airborne particulates from indoor and outdoor parking areas in Kandy. Additionally, the study aims to identify the types of vehicles specifically two-wheelers, three-wheelers, and four-wheelers that contribute most to microplastic emissions, providing insight into vehicle-related sources of urban microplastic pollution. Factors such as traffic intensity, road surface texture, and weather conditions, including the dry period, were considered in the analysis.

2. Literature review

Urban traffic is a major source of air and road dust pollution, contributing to elevated levels of particulate matter (PM10, PM2.5), heavy metals, and microplastics. Both exhaust and non-exhaust emissions (e.g., tire and brake wear, road dust resuspension) deteriorate air quality and pose serious health risks including respiratory and cardiovascular conditions.

Globally, road dust is known to contain toxic elements such as lead, copper, and zinc, with higher concentrations near high-traffic and industrial zones. In Sri Lanka, studies highlight that rapid motorization, especially, three-wheelers and poorly maintained roads worsen urban pollution. Although national air quality standards exist, enforcement remains weak (Rathnayake et al., 2023).

Microplastics in road dust originate mainly from tire wear and urban waste, and they are often resuspended into the air by traffic and wind. These microplastics commonly under 100 µm, contribute to PM10 and exhibit environmental persistence and toxicity.

Airborne microplastics, detected in PM10, are dispersed over long distances and interact with other pollutants, complicating source attribution and increasing health risks.

Resuspension of road dust significantly influences urban PM levels, especially in dry conditions and high-traffic areas. Mitigation strategies such as street cleaning, green infrastructure, and low-emission zones are critical for improving urban air quality and reducing health hazards (Das & Wiseman, 2024).

3. Methodology

3.1 Sample Collection and Processing

All activities related to road-deposited dust (RDD) sampling were carried out at selected indoor and outdoor vehicle parks in Kandy, including the Kandy Municipal Council (KMC) Vehicle Park (indoor) and the vehicle park near the Royal Botanic Gardens (outdoor). A 1.5 m × 1.5 m square area was marked for sampling, and dust was swept systematically to 3 directions using a non-plastic brush to metal pan to minimize contamination. Samples were transferred to labelled, non-reactive envelopes. Mean Texture Depth (MTD) was measured using the sand patch test, which helps evaluate surface voids and their role in dust accumulation.

Weather data (rainfall and temperature) were obtained from the Katugasthota station to assess the influence of antecedent dry periods on pollutant buildup. After collection, RDD samples were sieved into four size ranges: <75 µm, 75–150 µm, 150–300 µm, and 300 µm–1 mm. Particles >1 mm and >300 µm were weighed and discarded. As the samples were insoluble in water, TSS of the fractions were equal to their weights. For the MP identification, Microplastics (MPs) were isolated using hydrogen peroxide (H_2O_2) digestion (35 mL per 1 g of dust), stirred, and left for 24–48 hours until bubbles to disappear. The digested samples were filtered using 0.45 µm glass fiber filters, dried at 37°C, and then the remaining dried weight in the beaker was subjected to density separation using $ZnCl_2$ (1.7 g/cm³), stirred for 15 minutes, and allowed to settle for 24 hours. Floating MPs were filtered for analysis. Extracted MPs were examined using a ZEISS Stemi 305 microscope for size, shape, and color characterization.

For the analysis of pollutants in air, samples were collected near the Royal Botanic Gardens, Peradeniya, using a High-Volume Air Sampler (HVAS) positioned 1.5–2.0 m above the ground to capture particles within the human breathing zone. The HVAS was operated at a flow rate of 0.16–0.17 m³/min for four hours, collecting airborne particulates on 0.45 µm glass fiber filters. These filters were pre-conditioned by drying at 40°C for 24 hours to eliminate moisture. After sampling, filters were oven-dried at 37°C, cooled in a desiccator for 1 hour, and weighed using a high-precision balance (0.01 mg resolution). By using the accumulated dust weight and used air volume, PM10 was calculated. For MP analysis, Microplastics retained on the filters were then analyzed under the ZEISS Stemi 305 microscope to identify their size, shape, and color.

4. Results and Discussion

4.1 Variations of Total Suspended Solids (TSS) Load

Outdoor samples consistently showed higher TSS loads than indoor ones, even under similar dry conditions (e.g., OD3 vs. ID3), as depicted in Figure 1. This highlights the impact of environmental exposure on pollutant build-up. TSS loads increased with the duration of the dry period (Figure 1), likely due to the absence of rainfall to wash off accumulated particulates., a trend supported by previous findings (Leads et al., 2019).

Analysis of size fractions revealed that particles within the 1 mm–300 µm range were the most dominant across all samples, consistently contributing over 40% of the total TSS load (Figures 2 and 4). Although TSS distribution did not strictly correlate with road surface texture depth (Figure 3), the relative proportions of size fractions remained stable (Figure 4).

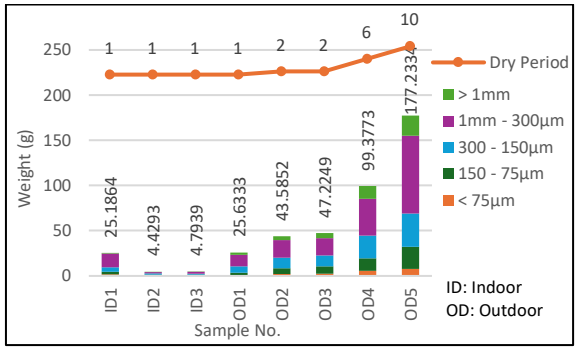

Figure 1: Variation of TSS load with dry period

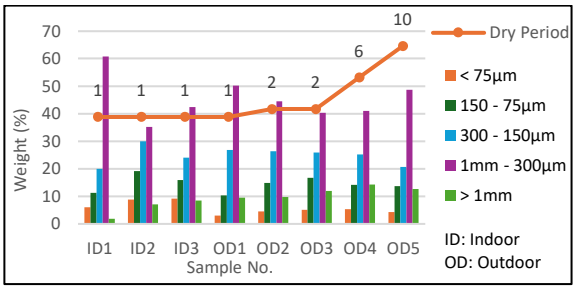

Figure 2: Variation of TSS load in each size fraction with dry period

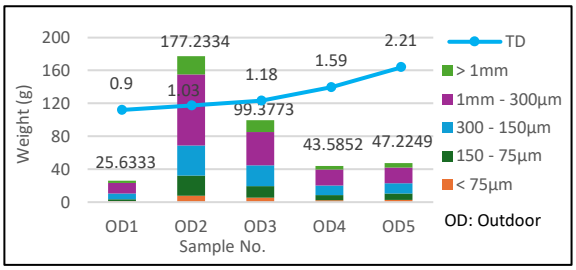

Figure 3: Variation of TSS load with road surface texture depth (TD: Texture Depth)

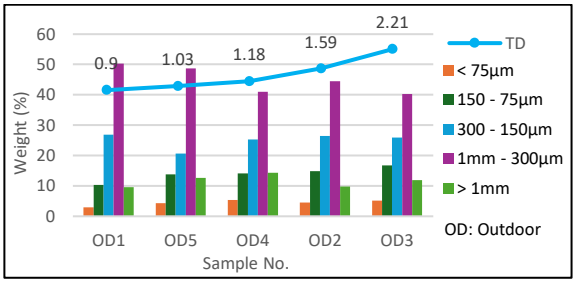

Figure 4: Variation of TSS load in each size fraction with road surface texture depth (TD: Texture Depth)

4.2 Variations of Digested Organic Matter

In indoor areas, organic matter content increased from four-wheeler (ID1) to two-wheeler zones (ID3) as shown in Figure 5. This may be due to greater frequency of pedestrian and tire contact in motorbike zones, increasing organic debris accumulation.

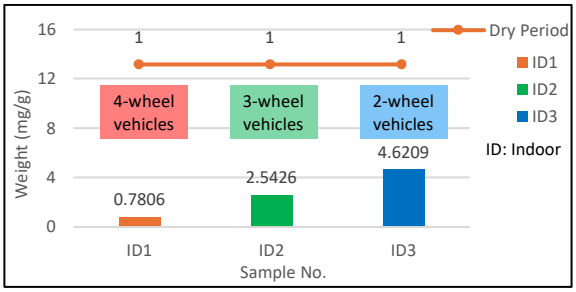

Figure 5: Variation of digested organic matter in indoor samples with dry period

In outdoor samples (Figure 6), organic matter loads also rose with the dry period, reflecting ongoing deposition without wash-off events. However, OD1 displayed a comparatively high value despite a short dry period. This may be attributed to the low rainfall (11.1 mm/day) before sampling, which may have been insufficient to cleanse previously deposited material.

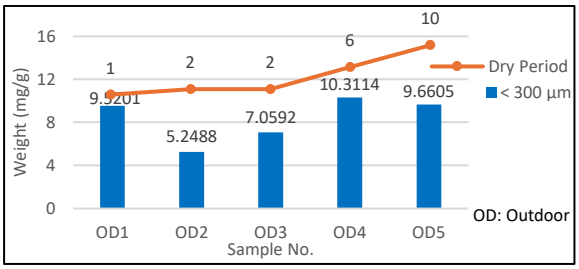

Figure 6: Variation of digested organic matter in outdoor samples with dry period

4.3 Variations of Microplastics (MP) in Road Dust

MP concentrations in indoor dust also followed the vehicle-type trend: increasing from four-wheel to two-wheel zones (ID1 < ID2 < ID3), as seen in Figure 7. This suggests tire wear and polymer fiber detachment are greater in areas with more vehicle turnover or friction.

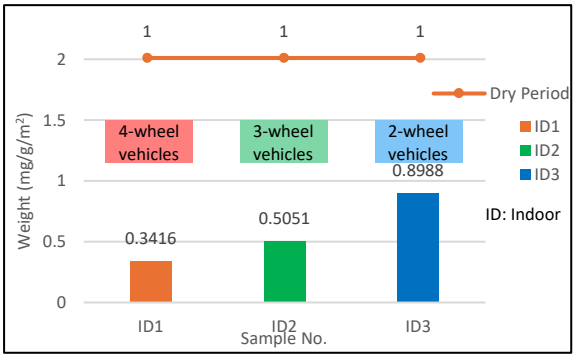

Figure 7: Variation of MP in indoor samples with dry period

In outdoor samples, MP concentrations increased with dry period (Figure 8), showing dry accumulation in the absence of rainfall and wash-off. However, Figure 9 shows a decline in MP levels with increased surface texture depth, likely due to increased wind activity that can resuspend and remove lightweight microplastics from coarser road surfaces. OD1 again acted as an outlier, likely due to insufficient rainfall prior to sampling, as discussed earlier.

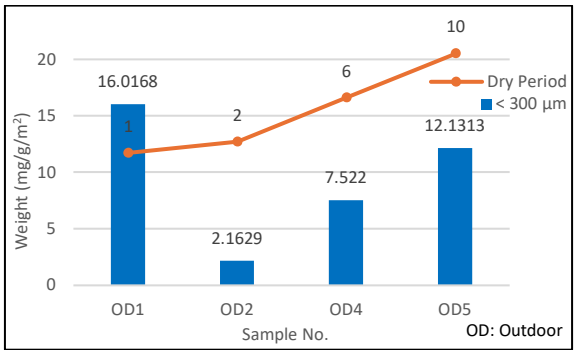

Figure 8: Variation of MP in outdoor samples with dry period

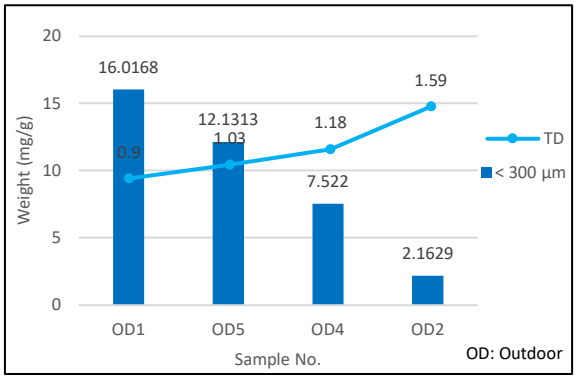

Figure 9: Variation of MP in outdoor samples with road surface texture depth

Microscopic analysis (Figure 10) revealed MPs in various colours and shapes, with black fragments and fibers dominating. This suggests significant tire wear contribution (Järlskog et al., 2023).

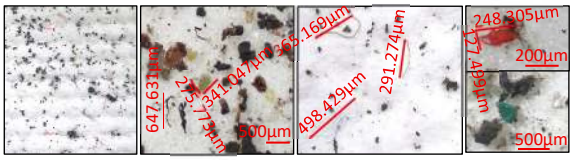

Figure 10: Microscopic images of MPs in road Deposited Dust

4.5 Variations of Properties of Air Samples

Particulate matter (PM10) concentrations increased with dry period (Figure 11), consistent with dust resuspension trends in dry urban environments. MPs were observed in both air samples, with fibers and fragments under 500 µm in black, red, and gold hues being most common (Figure 12). These results highlight atmospheric MP transport potential, especially under prolonged dry conditions.

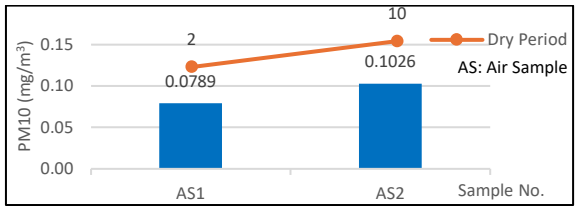

Figure 11: Variations of PM 10 in each air sample

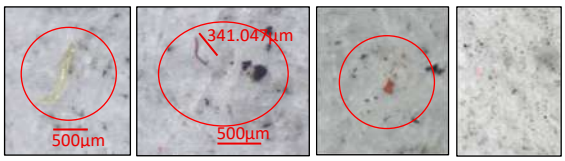

Figure 12: Microscopic images of MPs in air

5. Conclusions

The study found that microplastics (MPs) were present in both road dust and air samples, with higher concentrations in outdoor environments (21.281 mg/g) compared to indoor settings (12.445 mg/g). Total Suspended Solids (TSS) were also greater outdoors. Fragments and fibers were the dominant MP shapes, mostly black in color. MP levels increased during longer dry periods. Outdoors, smoother surfaces showed higher MP accumulation, while indoors, increased vehicle interaction led to higher levels of both organic matter and MPs.

References

Das, S. and Wiseman, C.L.S. (2024) 'Examining the effectiveness of municipal street sweeping in removing road-deposited particles and metal(loid)s of respiratory health concern', *Environment International*, 187, p. 108697.

Järlskog, I., Strömvall, A.-M., Magnusson, K., Gustafsson, M., Polukarova, M., Galfi, H. and Aronsson, M. (2020) 'Occurrence of tire and bitumen wear microplastics on urban streets and in sweepsand and washwater', *Science of The Total Environment*, 729, p. 138950.

Leads, R.R. and Weinstein, J.E. (2019) 'Occurrence of tire wear particles and other microplastics within the tributaries of the Charleston Harbor Estuary, South Carolina, USA', *Marine Pollution Bulletin*, 145, pp. 569–582.

Rathnayake, L.R.S.D., Sakura, G.B. and Weerasekara, (2023) 'Review of Outdoor Air Pollution in Sri Lanka Compared to the South Asian Region', *Nature Environment and Pollution Technology*, 22(2), pp. 609–621.

POTENTIAL USE OF RO CONCENTRATE/BRINE IN CONCRETE AS A PARTIAL REPLACEMENT FOR CEMENT

E.M.P.K. Ekanayake[1,*], S.M.K.P. Senanayake[1], W.M.D.S.B. Navaratna[1] and G.B.B. Herath[1]

Department of Civil Engineering, University of Peradeniya, 20400, Sri Lanka

* e19098@eng.pdn.ac.lk

Abstract

The increasing use of reverse osmosis (RO) desalination to meet freshwater demand has led to significant environmental concerns due to the disposal of RO brine, a waste stream rich in salts and chemicals. This study explores the reuse of RO brine as a partial cement replacement in concrete to mitigate its environmental impact. Using brine composition simulated with Wave software based on data from the Seawater Reverse Osmosis Desalination Plant in Jaffna, a synthetic brine solution was prepared in the laboratory. Concrete specimens were cast with varying brine replacement levels (25%, 50%, 75%, and 100%) while maintaining a constant mix design. Compressive strength was tested at 7 and 28 days. Results showed improved strength in mixes with 25%–75% brine, with the 75% replacement achieving the highest strength at 28 days. Although the 100% brine mix initially showed lower early strength, it surpassed the control by 28 days. The strength gains are linked to reactive ions in the brine enhancing cement hydration. The study concludes that using RO brine as a cement substitute is both technically effective and environmentally sustainable. Further research is recommended to assess long-term durability and reinforcement corrosion for broader implementation in sustainable construction.

Keywords: Reverse osmosis brine, Desalination, Cement replacement, Total Dissolved Solids

1. Introduction

Growing global water scarcity has led many countries to establish Seawater Reverse Osmosis (SWRO) plants to produce freshwater. In Sri Lanka, the first SWRO plant has been established in Jaffna to address regional water shortages. However, SWRO systems generate a concentrated waste stream known as brine, which contains high levels of dissolved ions such as chloride, sulphate, calcium, sodium, and magnesium.

Globally, desalination technologies produce about 51.7 billion cubic meters of brine annually, with approximately 38% (19.6 billion cubic meters) originating from RO processes (Lee et al., 2019). This brine is commonly discharged into oceans or nearby water bodies, causing environmental issues such as increased salinity and ecological imbalance.

This study investigates the use of SWRO brine as partial mixing water in concrete while proportionally reducing cement content based on the total dissolved solids (TDS) present in the brine. Unlike previous studies that mainly used RO brine as a direct replacement for freshwater, this research considers the chemical contribution of dissolved ions during cement hydration. By adjusting the cement content according to TDS concentration, the approach aims to utilize the accelerating effects of these ions on hydration and early strength development, thereby improving material efficiency and promoting sustainable reuse of desalination waste.

2. Literature review

Previous studies have investigated the use of RO brine as mixing water in concrete and reported that it can produce concrete with high strength due to its influence on cement hydration. The presence of high chloride concentrations promotes the formation of Friedel's salt, which fills pores and improves density and strength (Zhu et al., 2012). Similarly, incorporating GGBS with reject brine has been shown to enhance concrete strength (Fattah et al., 2017a), while CSA cement bricks and alkali-activated slag cement (AASC) mixed with RO brine also demonstrated improved compressive strength, particularly at early ages (Lee et al., 2019; Kang & Kim, 2022a).

However, several limitations have been identified. Concrete made with RO brine often exhibits reduced workability due to the high ion concentration increasing the viscosity of the mix (Lee et al., 2019). In addition, the high chloride content makes it generally unsuitable for reinforced concrete because of the increased risk of steel corrosion. Therefore, its application is mainly recommended for non-reinforced products such as pavements, blocks, and bricks. Despite some evidence of strength improvement, comprehensive studies on the reuse of RO brine as mixing water—especially considering cement replacement strategies and long-term durability under high salt conditions—remain limited.

3. Methodology

3.1 RO Brine Composition Determination and Validation

The RO brine composition was determined using a mass balance approach based on feed water ion concentrations, system recovery (40–50%), and permeate quality data from the Seawater Reverse Osmosis Desalination Plant in Jaffna. The composition was also simulated using WAVE software. The manually calculated results were compared with the WAVE simulation by evaluating percentage deviations, confirming the reliability of the manual estimation method. The results are presented in Table 1.

Table 8: Simulated and Manually Calculated RO Brine Composition

Ion	Unit	Manual Calculation	WAVE Software
Ca^{2+}	mg/L	532.7	620.1
Mg^{2+}	mg/L	3102.7	3155
Na^{+}	mg/L	15724.4	15979
K^{+}	mg/L	1069.1	1096
SO_4^{2-}	mg/L	4471.82	4640
Cl^{-}	mg/L	32402.73	32245

3.2 Synthetic Brine Preparation and Characterization

3.2.1 Synthetic Brine Recipe Preparation

The synthetic brine recipe formulation was primarily based on the calculated RO brine composition. The recipe included major ions such as Na^{+}, Ca^{2+}, Mg^{2+}, K^{+}, Cl^{-}, and SO_4^{2-}. All chemicals used for recipe preparation were of analytical reagent grade to ensure high purity.

3.2.2 Synthetic Brine Preparation

The synthetic RO brine was prepared at the laboratory by accurately weighing each salt according to the established recipe. These pre-weighed salts were then sequentially dissolved in distilled water under continuous magnetic stirring to ensure complete dissolution and homogeneity. Several quality parameters were measured, and the obtained values are provided in Table 2. The prepared synthetic brine was stored in a sealed glass bottle in the refrigerator until used for concrete mixing.

Table 2: Quality Parameters and Measured Values of Synthetic Brine

Parameters	Unit	Measured Value
pH	-	8.91
Temperature	^0C	28.9
TDS	mg/L	58.89
EC	mS/cm	113.5

3.3 Concrete Mix Design and Specimen Preparation

3.3.1 Mix Design Preparation

The concrete mix design was formulated to achieve a target cube compressive strength of 25 MPa at 28 days, as per ASTM C39. The design followed the guidelines of ACI 211.1. to ensure consistent workability and enable direct comparison of the brin's impact, a constant water-cement ratio of 0.5 was maintained across all mix designs. A portion of the cement content was substituted with an equivalent mass of the TDS present in the synthetic brine at each respective water replacement level of 0%, 25%, 50%, 75%, and 100%.

3.3.2 Cube Casting

All concrete mixes were prepared in a pan mixer. Bry ingredients (cement, coarse aggregates, fine aggregates) were first mixed for 30s, followed by the gradual addition of the mixing water (either potable water or synthetic

brine). Wet mixing continued for 3-4 minutes until a homogenous consistency was achieved.

Standard 100 mm x 100 mm x 100 mm steel cube moulds were prepared and fresh concrete was placed into the moulds with compacted using an external vibrating table for 15 seconds to minimize voids and ensure proper compaction. Each cast cube was uniquely labelled for identification.

3.3.3 Curing

After initial setting, the concrete cubes were demoulded at 24 hours. Following demoulding, all cubes were transferred to a water curing tank maintained at ambient temperature and atmospheric conditions until their respective testing ages.

3.4 Compressive Strength Testing

Compressive strength tests were performed on the concrete cubes at 7 and 28 days of curing.

4. Results and Discussion

4.1 Compressive Strength

4.1.1 7-day Compressive Strength

The 7-day compressive strength results, illustrated in Figure 1 and summarized provided critical insight into the impact of synthetic RO brine on early strength development. The control mix (0% brine) recorded a baseline strength of 9.78 MPa. According to Figure 1, incorporating moderate levels of RO brine significantly enhances early strength. The 50% RO brine replacement mix achieved a peak strength of 15.34 MPa, representing a remarkable 56.9% increase compared to the control sample. Similarly, 25% and 75% replacement levels also showed improved strengths of 14.5 MPa and 14.56 MPa, respectively. This enhancement is primarily attributed to the accelerated hydration effect of chloride (Cl^-) and sodium (Na^+) ions present in the brine, which promote faster setting and early C-S-H gel formation.

However, increasing the RO brine content to 100% resulted in a strength drop to 8.76 MPa, falling 10.43% below the control value. This suggests that excessive salt concentrations disrupt the hydration process or introduce detrimental porosity, negatively impacting strength.

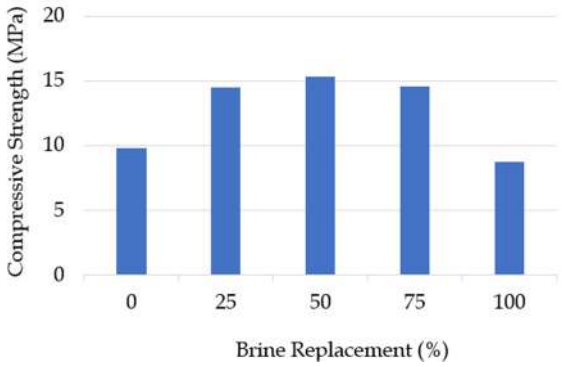

Figure 1: 7-day Compressive Strength Variation with Brine Replacement

RO brine water has been shown to accelerate hydration reactions, particularly enhancing the hydration of C_3S and C_3A, which are critical for early strength development (Fattah et al., 2017). However, when used at high concentrations, the excessive salt content can disrupt the balance of hydration, potentially increasing porosity and leading to a reduction in compressive strength (Zhu et al., 2012).

4.1.2 28-day Compressive Strength

The 28-day compressive strength can serve as a standard guide for long-term structural performance. As shown in Figure 2, all brine-containing mixes demonstrated an improvement in strength compared to the control mix (0% brine), which recorded 18.41 MPa.

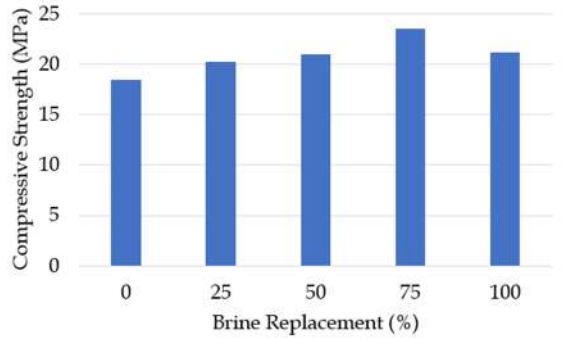

Figure 2:28-day Compressive Strength Variation with Brine Replacement

The most significant increase was observed at 75% brine replacement (23.49 MPa), representing a 27.6% improvement over the control. Notably, even the 100% brine replacement mix achieved 21.20 MPa, remaining higher than the control and contrasting with its 7-day performance, where it showed a reduction. Mixes with 25% and 50% brine also

performed well, reaching 20.25 MPa and 21.02 MPa, respectively.

This sustained strength enhancement suggests that the continued presence of chloride and other dissolved ions in the brine positively influenced long-term hydration and contributed to the formation of additional C-S-H gel, improving the internal curing environment. Unlike the 7-day trend, any initial negative effects of high salinity in the 100% brine mix appear to have been compensated for over time. These results confirm the potential of RO brine as a viable partial, or even full, mixing water substitute for concrete, with 75% replacement showing the most favourable outcome for 28-day strength.

RO brine has been found to contribute to long-term hydration by enhancing the formation of secondary hydration products, such as Friedel's salt, which fills micro-pores and strengthens the cement matrix (Lee et al., 2019). The presence of chloride ions supports sustained C-S-H gel formation and promotes microstructural densification, thereby improving later-age compressive strength (Fattah et al., 2017). In the present study, the mix with 75% brine replacement achieved the highest 28-day strength value of 23.49 MPa, suggesting that the interaction between chloride ions and tricalcium aluminate (C_3A) facilitated the formation of Friedel's salt. This reaction likely contributed t**o** the development of a denser and more durable cementitious structure.

5. Conclusions

- Synthetic RO Brine Utilization: A lab-grade synthetic RO brine was successfully prepared based on real RO plant parameters using Wave software, enabling realistic simulation of brine water in concrete mixing.
- Enhanced Early Strength: The use of RO brine at 25–75% replacement levels significantly improved the 7-day compressive strength of concrete, with the 50% brine mix achieving the highest strength gain of approximately 57% compared to the control.
- Sustained Long-Term Performance: At 28 days, all brine replacement levels showed higher compressive strength than the control, with the 75% brine mix recording the peak strength of 23.49 MPa, indicating continued strength development over time.
- Optimal Replacement Range Identified: Brine replacement between 25–75% was found to be optimal, providing both early and long-term strength enhancement. The 100% brine mix showed lower early strength but recovered by 28 days.
- Feasibility of RO Brine in Concrete: The study confirms the feasibility of using RO brine as a partial replacement for mixing water in concrete production, offering a sustainable alternative for freshwater usage in construction

References

Fattah, K.P., Al-Tamimi, A.K., Hamweyah, W. and Iqbal, F. (2017). 'Evaluation of Sustainable Concrete Produced with Desalinated Reject Brine', *International Journal of Sustainable Built Environment*, 6, pp.183–190.

Halder, B.K., Tandon, V., Chintalapalle, R.V., Roy, D. and Tarquin, A. (2015). 'A Potential Biological Approach for Sustainable Disposal of Total Dissolved Solid of Brine in Civil Infrastructure', *Construction and Building Materials*, 76, pp.51–60.

Kang, C. and Kim, T. (2022). 'Effect of Reverse-Osmosis Brine and Sodium Aluminate on the Hydration Properties and Strength of Alkali-Activated Slag Cement', *Case Studies in Construction Materials*, 16.

Lee, H., Jeon, D., Song, H., Sim, S.W., Kim, D., Yu, J., Cho, K.H. and Oh, J.E. (2019). 'Recycling of Reverse Osmosis (RO) Reject Water as a Mixing Water of Calcium Sulfoaluminate (CSA) Cement for Brick Production', *Applied Sciences*, 9.

Zhu, Q., Chen, Q., Li, X. and others (2012). 'Effect of Chloride Salt Type on Chloride Binding Behavior of Concrete', *Construction and Building Materials*, 34, pp.94–101.

Sponsored By

TOKYO CEMENT GROUP

DEPARTMENT OF CIVIL ENGINEERING
FACULTY OF ENGINEERING
UNIVERSITY OF PERADENIYA
SRI LANKA

9 773021 673003